UNIVERSIDADE ESTADUAL DE CAMPINAS
INSTITUTO DE GEOCIÊNCIAS

WELLINGTON PAULO DE OLIVEIRA

GEOMAGNETIC FIELD VARIATIONS OVER THE PAST 10 Myr

VARIAÇÕES DO CAMPO GEOMAGNÉTICO PARA OS ÚLTIMOS 10 Ma

CAMPINAS
2022

WELLINGTON PAULO DE OLIVEIRA

GEOMAGNETIC FIELD VARIATIONS OVER THE PAST 10 Myr

VARIAÇÕES DO CAMPO GEOMAGNÉTICO PARA OS ÚLTIMOS 10 Ma

TESE APRESENTADA AO INSTITUTO DE GEOCIÊNCIAS DA UNIVERSIDADE ESTADUAL DE CAMPINAS PARA OBTENÇÃO DO TÍTULO DE DOUTOR EM CIÊNCIAS NA ÁREA DE GEOLOGIA E RECURSOS NATURAIS.

THESIS PRESENTED TO THE INSTITUTE OF GEOSCIENCES OF THE UNIVERSITY OF CAMPINAS TO OBTAIN THE DEGREE OF DOCTOR IN SCIENCES IN AREA OF GEOLOGY AND NATURAL RESOURCES.

ORIENTADOR: PROF. DR. GELVAM ANDRÉ HARTMANN

ESTE EXEMPLAR CORRESPONDE À VERSÃO DA TESE DEFENDIDA PELO ALUNO WELLINGTON PAULO DE OLIVEIRA E ORIENTADO PELO PROF. DR. GELVAM ANDRÉ HARTMANN

CAMPINAS
2022

Ficha catalográfica
Universidade Estadual de Campinas
Biblioteca do Instituto de Geociências
Marta dos Santos - CRB 8/5892

OL43g Oliveira, Wellington Paulo de, 1989-
Geomagnetic field variations over the past 10 Myr / Wellington Paulo de Oliveira. – Campinas, SP : [s.n.], 2022.

Orientador: Gelvam André Hartmann.
Tese (doutorado) – Universidade Estadual de Campinas, Instituto de Geociências.

1. Geomagnetismo. 2. Variação espacial. 3. Paleomagnetismo. I. Hartmann, Gelvam André, 1978-. II. Universidade Estadual de Campinas. Instituto de Geociências. III. Título.

Informações para Biblioteca Digital

Título em outro idioma: Variações do campo geomagnético para os últimos 10 Ma
Palavras-chave em inglês:
Geomagnetism
Spatial variation
Paleomagnetism
Área de concentração: Geologia e Recursos Naturais
Titulação: Doutor em Geociências
Banca examinadora:
Gelvam André Hartmann [Orientador]
Augusto Ernesto Rapalini
Cosme Ferreira da Ponte Neto
Daniele Cornellio de Paiva Caldeira Brandt
Ricardo Ivan Ferreira da Trindade
Data de defesa: 12-08-2022
Programa de Pós-Graduação: Geociências

Identificação e informações acadêmicas do(a) aluno(a)
- ORCID do autor: https://orcid.org/0000-0002-5363-2234
- Currículo Lattes do autor: http://lattes.cnpq.br/1225953623904894

UNICAMP

UNIVERSIDADE ESTADUAL DE CAMPINAS

INSTITUTO DE GEOCIÊNCIAS

AUTOR: Wellington Paulo de Oliveira

GEOMAGNETIC FIELD VARIATIONS OVER THE PAST 10 Myr

VARIAÇÕES DO CAMPO GEOMAGNÉTICO PARA OS ÚLTIMOS 10 Ma

ORIENTADOR: PROF. DR. GELVAM ANDRÉ HARTMANN

Aprovada em: 12/08/2022

EXAMINADORES:

Prof. Dr. Gelvam André Hartmann - Presidente

Prof. Dr. Augusto Ernesto Rapalini
Prof. Dr. Cosme Ferreira da Ponte Neto
Profa. Dra. Daniele Cornellio de Paiva Caldeira Brandt
Prof. Dr. Ricardo Ivan Ferreira da Trindade

A Ata de Defesa assinada pelos membros da Comissão Examinadora consta no processo de vida acadêmica do aluno.

Campinas, 12 de agosto de 2022.

SÚMULA/BIOGRAFIA

Wellington Paulo de Oliveira nasceu e viveu na cidade de Duque de Caxias-RJ no ano de 1989. Em 2014, concluiu a graduação (bacharelado e licenciatura) em Física pela Universidade Estadual do Rio de Janeiro (UERJ), tendo sido bolsista de iniciação científica (PIBIC-CNPq) do Centro Brasileiro de Pesquisas Físicas (CBPF) entre 2012 e 2013, onde desenvolveu estudos baseados em Espectroscopia Mössbauer para supercondutores de alta temperatura crítica. Os resultados da iniciação científica foram publicados em livros de resumos do CBPF. Além disso, efetuou estágio supervisionado no Instituto de Aplicação Fernando Rodriguez da Silveira (CAp-UERJ) e Colégio Pedro II (Campus Caxias) no ano de 2013, realizando atividades em Ensino Médio de Física. É mestre em Geofísica pelo Observatório Nacional (2017), aonde desenvolveu estudos relacionados à variação paleosecular durante o Superchron Reverso do Permo-Carbonífero, com resumos publicados em 2 eventos científicos, o VII Simpósio Brasileiro de Geofísica (SimBGf) 2016 e 5th Biennial Latinmag 2017. Por estes trabalhos e pelos resultados publicados em revistas de alto impacto científico, foi contemplado com Menção Honrosa no Prêmio de Melhor Dissertação (biênio 2018-2019) da Sociedade Brasileira de Geofísica (SBGf). Durante o seu doutorado em Geociências pela Universidade Estadual de Campinas (UNICAMP), abordou as variações do campo geomagnético (CG) para os últimos 10 Ma. A fim de investigar a morfologia do CG ao longo do tempo, realizou análises sobre bancos de dados paleomagnéticos direcionais atualizados, modelagem do campo geomagnético histórico (1840-2015), e para o intervalo de 0-10 Ma. Além disso, contribuiu com novos dados paleodirecionais a partir de rochas vulcânicas (com idades inferiores a 2 Ma) da Colômbia, em uma região escassa de dados para a América do Sul. Publicou em 5 resumos científicos em congressos internacionais da área de Geomagnetismo. Também realizou estágio de capacitação docente no Instituto de Geociências da UNICAMP em 2018. Em sua carreira, já publicou quatro artigos (2022, 2021, 2019, 2018) em periódicos internacionais indexados de classificação A1, demonstrando protagonismo científico: *Physics of the Earth and Planetary Interiors* (DOI: 10.1016/j.pepi.2022.106926), *Geochemistry, Geophysics, Geosystems* (G-Cubed; DOI: #10.1002/2017GC007262; #10.1029/2021GC010063) e *Scientific Reports* (DOI:10.1038/s41598-018-36494-x). Participou em bancas de comissões julgadoras (2021) de monografias e trabalhos científicos. Vem atuando nas áreas de pesquisa de Geomagnetismo (avaliações de variações do campo geomagnético operantes em diferentes escalas de tempo ao longo do tempo geológico), Paleomagnetismo e Magnetismo de rochas.

DEDICATÓRIA

À minha família.

ACKNOWLEDGEMENTS

Firstly, I thank God for giving me health and strength for my achievements.

I would especially like to acknowledge my advisor Prof. Dr. Gelvam André Hartmann for his guidance, patience and discussions of this interesting research topic. I appreciate the opportunity to work with him and his constant support to complete this research project.

I am grateful the contributions of Prof. Dr. Andrew Biggin, Dr. Richard Bono, and Dr. Yael Engbers of the University of Liverpool for their helpful suggestions, resources for data analysis, and collaboration regarding the first published article included in this thesis.

I also thank Prof. Dr. Jairo Savian (Universidade Federal do Rio Grande do Sul), Prof. Dr. Mauricio Parra (University of São Paulo - USP), and Giovanny Rodriguez (PhD candidate in Geology - USP) who provided valuable assistance with the volcanic sample collection during a fieldwork carried out in Colombia, and contributions to the second article included in this thesis.

My gratitude to the committee members of the Laboratory of Paleomagnetism – USPMag: Prof. Dr. Andréa Ustra and Prof. Dr. Ricardo Trindade for permission to use the facilities. I also want to thank Daniele Brandt, Giovanni Moreira, and Sonia Urenha for their support in the laboratory work.

The professors of the Postgraduate Department of the Institute of Geosciences, Universidade Estadual de Campinas (IG-UNICAMP): Ana de Abreu, Alessandro Batezelli, Emilson Leite, and Vinícius Meira. I would like to express my appreciation for their support and important contributions in my academic formation.

The library staff and the Postgraduate Office (IG-UNICAMP), my thanks for the assistance.

I am grateful for the help of research colleagues at the Institute of Astronomy, Geophysics and Atmospheric Sciences (IAG-USP): Filipe Terra-Nova, Thiago Moncinhatto, Janine do

Carmo, Ualisson Bellon, and Filipe Temporim.

I would like to thank to colleagues and friends of the Posgraduate Program in Geosciences – UNICAMP: Bruno dos Santos, Carlos Medina, Cleberson Vieira, Douglas Martins, Eduardo Geraldo, Endel Muller, Josué Passos, Jussara Secco, Laura Correa, Poliana Toledo, Robert Muniz, Sanny Castro, and Simmon Souza. All the people who helped me in any way and not mentioned here also have my gratitude.

My deepest gratitude to Luciana, Renato, and Lucca for their hospitality and accommodation in their residence for 2 months.

Lastly, I would like to acknowledge my family for all support, encouragement, and affection that they gave me at all times of this journey; especially my mother Maria Ramos, and my brothers André de Oliveira and Wagner de Oliveira.

This study was financed in part by the Coordenação de Aperfeiçoamento de Pessoal de Nível Superior – Brasil (CAPES) - Finance Code 001.

This study was financed in part by The Brazilian National Council for Scientific and Technological Development (CNPq), grants 165161/2018-3 and 425728/2018-8.

This study was financed in part by Student Stay Program – UNICAMP.

RESUMO

O campo magnético principal da Terra exibe variações espaciais em diferentes escalas de tempo, desde anos até bilhões de anos. Para os últimos 10 milhões de anos, a estrutura do campo é limitada pela distribuição e desigualdade espacial e temporal de dados paleomagnéticos. Em particular, a América do Sul contribui com apenas 10% do banco de dados global. Uma melhor distribuição inter-hemisférica de dados é crucial para reconstrução do campo e a compreensão de fenômenos em escalas de tempo de milhões de anos. Os objetivos desta tese são: (1) avaliar o comportamento da variação paleosecular (VPS) e a estrutura do campo médio (CM) para o intervalo de 0-10 Ma e os chrons Matuyama e Brunhes, com base em uma atualização do banco de dados para os últimos 10 Ma; (2) investigar a assimetria equatorial da VPS, e (3) expandir o banco de dados da América do Sul com novos dados paleodirecionais da Colômbia. A nova base de dados foi obtida a partir de uma coleção de estudos paleomagnéticos utilizando rigorosos critérios de seleção, com melhorias na cobertura espacial e temporal de dados paleodirecionais comparado com compilações anteriores. Este banco de dados foi usado para construir novos modelos de VPS com base na curva de ajuste de dispersão de polos geomagnéticos virtuais (PGVs) adaptado ao Modelo G. Além disso, novos modelos de CM foram desenvolvidos a partir de dados de anomalia de inclinação usando uma descrição dos harmônicos esféricos. Os resultados indicam uma baixa dependência latitudinal da curva de dispersão de PGVs para os últimos 10 Ma. Neste período, os modelos CM sugerem a presença de termos zonais de quadrupolo e octupolo de cerca de 3,2% e 1,2% do termo de dipolo axial, respectivamente. As estimativas de VPS e CM revelam diferenças entre os chrons Brunhes e Matuyama. Um teste estatístico sugere uma assimetria hemisférica da VPS para o chron Brunhes, que possui um elevado padrão de dispersão de PGVs no hemisfério sul em relação ao hemisfério norte. Investigações adicionais para o campo histórico (1840-2015) apontam que a assimetria equatorial de dispersão de PGVs aumenta progressivamente com o tempo, associada com o decaimento (aumento) do campo dipolar (campo não-dipolar). Um estudo paleomagnético foi realizado a partir de amostras de rochas vulcânicas do Pleistoceno-Holoceno coletadas em três vulcões (vulcões Doña Juana, Galeras e Morasurco) localizados no sudoeste da Colômbia. Os resultados, a partir de 30 dados paleodirecionais de alta qualidade, revelam alta dispersão de PGVs para os intervalos de 0-2 Ma e Brunhes. Da mesma forma, as anomalias de inclinação sugerem grandes desvios em relação ao campo de dipolo geocêntrico axial, consistentes com os novos modelos CM. A alta dispersão no Sul da Colômbia pode estar relacionada com a acentuada variabilidade longitudinal do equador magnético na região equatorial da América do Sul, e que tem sido observada em modelos de campo recentes para escalas de séculos e milênios. As investigações realizadas nesta tese forneceram informações importantes sobre as variações geomagnéticas de longo prazo e restrições em modelos numéricos de geodínamo.

Palavras-Chave: Variação Paleosecular; Campo Paleomagnético; Assimetria Equatorial da Variação Paleosecular; Dispersão de Polos Geomagnéticos Virtuais; Anomalia de Inclinação.

ABSTRACT

The Earth's main magnetic field exhibits spatial variations at different timescales, from years to billions of years. For the past 10 million years, the paleomagnetic field structure is limited by the irregular spatial and temporal distributions of paleomagnetic data. In particular, South America contributes only 10% of the global database. A better inter-hemispheric distribution of paleomagnetic data is crucial for field reconstruction and understanding of phenomena over the past million years. The aims of this thesis are (1) to assess the paleosecular variation (PSV) behavior and the time-averaged field (TAF) structure for the 0-10 Ma interval and the Matuyama and Brunhes chrons, based on an updated 0-10 Ma database; (2) to investigate the equatorial PSV asymmetry, and (3) to expand the South American database with new paleodirectional data from Colombia. The new database was obtained from a collection of paleomagnetic studies using strict selection criteria. It provided improvements in the spatial and temporal coverage of paleodirectional data compared to previous compilations. The upgraded database was used to construct new PSV models based on the best-fit curve to the virtual geomagnetic pole (VGP) estimates adapted to Model G. Additionally, new TAF models were designed from inclination anomaly data using a spherical harmonic description. Results indicate a low latitudinal dependence of VGP dispersion curve for the past 10 Myr. In this period, TAF models show the presence of zonal quadrupole and octupole terms of about 3.2% and 1.2% relative to axial dipole term, respectively. PSV and TAF estimates reveal differences between the Brunhes and Matuyama chrons. A statistical test suggests a hemispheric PSV asymmetry for the Brunhes chron, with a stronger latitudinal variation of VGP dispersion in the southern hemisphere than in the north. Further investigations into the historical field (1840-2015) point out that equatorial asymmetry of VGP dispersions increases progressively with time, associated with the dipole field decay and increased non-dipole field components. A paleomagnetic study was carried out from Pleistocene-Holocene volcanic rock samples collected from three volcanoes (Doña Juana, Galeras, and Morasurco volcanoes) located in southwestern Colombia. From 30 high-quality paleodirectional data, the results reveal high VGP dispersion for the 0-2 Ma and Brunhes intervals. Likewise, the inclination anomalies suggest large deviations for a geocentric axial dipole field, consistent with the new TAF models. The high VGP scatter in southern Colombia may be linked to the enhanced longitudinal variability of the magnetic equator in the equatorial South America region, which has been observed in recent field models for the centuries and millennia timescales. The investigations carried out in this thesis provided important information about long-term geomagnetic variations and constraint numerical geodynamo models.

Keywords: Paleosecular Variation; Time-Averaged Field; Equatorial Paleosecular Variation Asymmetry; Virtual Geomagnetic Pole Dispersion; Inclination Anomaly.

LIST OF FIGURES

LIST OF TABLES

LIST OF ABBREVIATIONS

AFD	Alternating-field demagnetization.
ChRM	Characteristic remanent magnetization.
CMB	Core-mantle boundary.
CNS	Cretaceous Normal Superchron.
DC	Demagnetization code.
DJVC	Doña Juana Volcanic Complex.
EMF	Earth’s magnetic Field.
FORC	First-order reversal curve.
GAD	Geocentric axial dipole.
GGP	Giant Gaussian Process.
GPTS	Geomagnetic polarity time scale.
GVC	Galeras Volcanic Complex.
IGRF65	International Reference Geomagnetic Field model for 1965.
IHMP	Illawarra Hyperzone of Mixed Polarity.
IRM	Isothermal remanent magnetization.
LLSVP	Large Low Shear Velocity Province.
MD	Multidomain.
NRM	Natural remanent magnetization.
NVZ	Northern Volcanic Zone.
PCRS	Permo-Carboniferous Reversed Superchron.
PSD	Pseudo-single domain.
PSV	Paleosecular variation.
PSV10	Paleomagnetic database for the 0-10 Ma interval of Cromwell et al. (2018).
RMS	Root mean square.
SAA	South Atlantic Anomaly.
TAF	Time-averaged field.
THD	Thermal demagnetization.
VGP	Virtual geomagnetic pole.

LIST OF SYMBOLS

α_{95}	95% confidence cone about the mean direction.
A_{95}	95% confidence cone about the VGP direction.
a	Model G parameter associated with the secondary geodynamo family.
b	Model G parameter associated with the primary geodynamo family.
β	Longitudinal difference between the paleomagnetic pole and site.
$\chi(T)$	Thermomagnetic susceptibility.
ΔI	Inclination anomaly.
ΔS	Interhemispheric variance.
λ	(Paleo)latitude.
θ	(Paleo)colatitude.
D	Magnetic declination.
F	Total intensity.
g_1^0	Axial dipole term.
g_2^0	Axial quadrupole term.
g_3^0	Axial octupole term.
$G2$	Ratio between the axial quadrupole term and the axial dipole term.
$G3$	Ratio between the axial octupole term and the axial dipole term.
H	Horizontal component of F.
H_c	Coercive force.
H_{cr}	Coercivity of remanence.
I	Magnetic inclination.
I_{OBS}	Observed inclination.
k	Fisher precision parameter of directions.
K	Fisher precision parameter of VGPs.
M_s	Saturation magnetization.
M_{rs}	Saturation remanent magnetization.
n	Number of samples per site.
N	Number of sites.
P	Paleomagnetic pole.
S	Total VGP dispersion.
S_B	Between-site VGP dispersion.
S_p	VGP dispersion associated with the primary geodynamo family.
S_s	VGP dispersion associated with the secondary geodynamo family.
S_w	Within-site VGP dispersion.
T_c	Curie temperature.

CONTENTS

1. INTRODUCTION

The Earth's magnetic field (EMF) exhibits variations over a wide spectrum of timescales (Hulot et al., 2010). Short-period variations (from seconds to days) arise from disturbances of electric currents in the ionosphere and magnetosphere, which are associated with diurnal variations and geomagnetic storms (Hulot et al., 2015). These variations are detected from magnetic observatories, operating in the late 15th century (Jackson & Murray, 1997) and recently by satellite measurements, such as the MAGSAT (1979-1980), Oersted (1999), CHAMP (2000-2010) and SWARM (launched in 2013) missions (Korte & Mandea, 2019). Long-period geomagnetic variations originate from dynamic processes in the Earth's liquid outer core, by means of a mechanism known as the geodynamo (Buffett, 2000). Variations of the main internal geomagnetic field occur over years to billions of years timescales (Aubert et al., 2010), and include the events associated with drastic changes of the ancient geomagnetic field (the paleomagnetic field) known as geomagnetic excursions and reversals with duration in the order of 10^4 years (A. P. Roberts, 2008). On these timescales, the EMF variability is observed indirectly through changes in field direction and intensity, which encompasses several databases such as magnetic observatories and mainly records obtained from archaeological artifacts and geological materials (Hulot et al., 2010).

The temporal variation of internal origin of the order of $10^5 - 10^6$ years, observable at the Earth's surface is referred to as paleosecular variation (PSV; Johnson & McFadden, 2015), which according to some studies (e.g., Buffett, 2015; R. Heller et al., 2002; Zhang & Zhong, 2011) it is associated with changes in the core-mantle boundary (CMB) heat flux. PSV has been investigated through paleomagnetic records of rock materials (sedimentary and volcanic rocks), and are crucial for a better understanding of the evolution and morphology of the geomagnetic field (Aubert et al., 2010), as well as providing constraints for numerical geodynamo models (Biggin et al., 2020; Christensen & Olson, 2003; Coe & Glatzmaier, 2006; Davies et al., 2008; Meduri et al., 2021; Olson & Christensen, 2002; Sprain et al., 2019). When PSV is averaged over a long time period, the time-averaged field (TAF) is described in first order by a geocentric axial dipole (GAD; Merrill & McFadden, 2003). The GAD hypothesis is fundamental to paleomagnetism with applications for plate tectonic reconstructions (McElhinny & McFadden, 2000; Tauxe, 2010). PSV behavior and the TAF structure are commonly evaluated by the latitudinal pattern of two statistical parameters

(Johnson & McFadden, 2015): (i) the angular dispersion of virtual geomagnetic poles (VGPs), which are defined as the pole position of a geocentric dipole for a given instant in time and locality from the observed direction of the magnetic field (Butler, 1998); (ii) the inclination anomaly, which is usually determined by the difference between the Fisher (R. A. Fisher, 1953) mean inclination and the expected GAD inclination.

Statistical analysis of VGP patterns according to Model G (McFadden et al., 1988) has been used widely in evaluations of PSV behavior over Precambrian times (e.g., Biggin et al., 2008a; Biggin et al., 2008b; de Oliveira et al., 2018; Doubrovine et al., 2019; Franco et al., 2019; Handford et al., 2021; Johnson et al., 2008; Smirnov et al., 2011; Veikkolainen & Pesonen, 2014). For the 0-10 Ma interval, marked by a high average frequency reversal (~ 4.9 reversals per million years), Doubrovine et al. (2019) found a strong latitudinal variation of VGP dispersion curve (Model G), using the 0-10 Ma database from lava flows (PSV10) of Cromwell et al. (2018). TAF models for the last 5 Myr (e.g., Cromwell et al., 2018; Johnson et al., 2008; McElhinny et al., 1996) are constructed from spherical harmonic analysis of paleodirectional (or inclination anomaly) data. They indicate the presence of small non-dipole field contributions, which are similar to recent geomagnetic models for the 0-100 ka (Panovska et al., 2018b; Panovska et al., 2019) and 0-10 ka (Constable et al., 2016) intervals.

Specific aspects related to geomagnetic field hemispheric asymmetry and differences between normal and reverse polarity field geometries over the last few million years have been debated (Cromwell et al., 2018; Cromwell et al., 2013a; Engbers et al., 2020; Johnson & McFadden, 2015). For instance, global geomagnetic field models on centennial to millennial timescales (Constable et al., 2016; Panovska & Constable, 2017; Panovska et al., 2019) have suggested a high field variability in the southern hemisphere than the northern hemisphere. For the past 10 Myr, the results are not entirely conclusive (Cromwell et al., 2018; Cromwell et al., 2015). Recent studies reveal an anomalous field behavior in the South Atlantic region, supported by the high VGP dispersion and low intensity estimates in the volcanic islands of Tristan da Cunha (Shah et al., 2016) and Saint Helena (Engbers et al., 2020; Engbers et al., 2022), respectively, formed around 90 ka and 11 Ma. It has been suggested (Campuzano et al., 2019; Engbers et al., 2022) that the recurrence of this anomalous feature is associated with the South Atlantic Anomaly (SAA), which is characterized by the lowest total intensity values observed for the present and historical fields (Finlay et al., 2020; Hartmann & Pacca, 2009; Rother et al., 2021). SAA covers a large area from southern Africa to South America, with a strong presence in the Brazilian territory (Finlay et al., 2020). Tarduno et al. (2015) proposed that the CMB compositional heterogeneity and structure under southern Africa (constrained by a Large Low Shear Velocity Province (LLSVP; Garnero & McNamara, 2008)) trigger core flux expulsions and resulting in a weak field in this region. The authors also suggested that the African LLSVP is responsible for the persistence of SAA and for promoting geomagnetic reversals on million years timescales.

Hemispherical asymmetries in both PSV and the TAF are of interest given the potential to provide important insights into the Earth's interior processes (McFadden & Merrill, 2007). However, the greatest barriers to a better assessment of the paleomagnetic field behavior over the past few million years are the low quality and uneven temporal and spatial distribution of paleomagnetic data (Hulot et al., 2010; Johnson & McFadden, 2015; Johnson et al., 2008). The scarcity of these data is quite remarkable at low and high latitudes. In particular, South America contributes only ~10% of the PSV10 database (Cromwell et al., 2018). These limitations illustrate the difficulties for a better understanding of the geomagnetic field evolution for the past 10 Myr and the dynamic geodynamo behavior.

Therefore, the main objectives of this thesis are: (i) to assess the latitudinal structure of paleosecular variation and the time-averaged field for three distinct time periods, the 0-10 Ma interval and the Matuyama and Brunhes chrons, based on a revised and updated 0-10 Ma paleodirectional database from lava flows; (ii) to assess the equatorial paleosecular variation asymmetry in these time intervals, based on VGP dispersion patterns in a broad interhemispheric coverage, and (iii) to contribute new high-quality paleodirectional data from volcanic rock targets in Colombia. The obtained results are presented and discussed in the form of two scientific articles: a study published in the journal *Geochemistry, Geophysics, Geosystems*, and another accepted to *Physics of the Earth and Planetary Interiors*.

This thesis is structured as follows. Chapter 2 provides theoretical framework information about the main components and particularities of the Earth's magnetic field, such as the generation of the main geomagnetic field, polarity reversals and long-term geomagnetic variations, and a description of the paleomagnetic databases available for the 0-10 Ma interval used to build paleosecular variation and the time-averaged paleomagnetic field models. Chapter 3 presents a new paleodirectional database spanning 0-10 Ma from a published paper (de Oliveira et al., 2021), with improvements in geographic and temporal coverage of paleomagnetic data. It provides new insights into latitudinal variation of paleosecular variation and the time-averaged field morphology. An innovative aspect of this work concerns a statistical approach employed to investigate the equatorial asymmetry of the historical and paleomagnetic fields. For the historical period (1840-2015), the results are discussed in respect of the geomagnetic field evolution. Chapter 4 presents new high-quality paleodirectional data from lava flows sampled in three stratovolcanoes from southwestern Colombia (de Oliveira et al., 2022), covering the last 2 Myr. This data expands the 0-10 Ma database at equatorial latitude South America in a sparsely populated region. Furthermore, a detailed investigation of magnetic mineralogy of the volcanic samples was carried out. New findings suggest the hypothesis of a high VGP dispersion related to a strong variability of the magnetic equator over the South American equatorial region that persists over different timescales. Finally, Chapter 5 presents the concluding remarks highlighting the results found in this thesis.

2. THEORETICAL FRAMEWORK

2.1 The geomagnetic field

2.1.1 Generation of the main geomagnetic field

The EMF is generated by convection currents in the electrically conducting fluid outer core (P. H. Roberts & King, 2013). Some authors (e.g., Buffett, 2000; Dormy & Le Mouël, 2008; Litasov & Shatskiy, 2016) suggest that this fluid is mainly composed of iron (Fe) and nikel (Ni) with the presence of light elements, particularly sulfur (S), oxygen (O) and silicon (Si) at about 10% in proportion. The hypothesis that has been accepted to explain the generation and maintenance of the geomagnetic field concerns the self-sustaining dynamo. It referred to as the mechanism responsible for the constant conversion of kinetic energy of the liquid outer core into electromagnetic energy (Olson, 2015).

Convective processes in the Earth's interior are dependent on two energy sources (Olson, 2015): (i) thermal energy associated with the latent heat of crystallization at the inner core boundary, combined with the temperature gradients along the base and top of the outer core that produce thermal convection, and (ii) compositional energy from light elements released into fluid outer core during the crystallization and growth of inner core. As addressed by some studies (e.g., Buffett, 2000; De Koker et al., 2012; Labrosse, 2003; Landeau et al., 2017), compositional convection is considered as the most important energy source to the present-day geodynamo. Moreover, the Coriolis effect caused by the Earth's rotation plays a fundamental role to self-sustained magnetic field production and influence on convective dynamic (Christensen, 2011; Glatzmaier & Olson, 2005).

Over the past three decades, significant progress from numerical geodynamo simulations has provided valuable information regarding the structure and geomagnetic field generation and its evolution over the time. Overall, these simulations try to solve the governing equations of the magnetohydrodynamic theory, which involves conservation of mass, momentum, energy, as well as fluid dynamics and magnetic induction equations (Glatzmaier, 2002). There are several geodynamo models that investigate the morphological and temporal features of the modern field, geomagnetic polarity reversals and observable aspects of the paleomagnetic field (e.g., Amit et al., 2015; Coe & Glatzmaier, 2006; Davies & Constable, 2020; Glatzmaier et al., 1999; Glatzmaier & Roberts, 1995; Terra-Nova et al., 2019).

Nevertheless, few studies apply the geodynamo theory to investigate the statistical properties of the time-averaged paleomagnetic field over the last few million years (e.g., Biggin et al., 2020; Davies et al., 2008; Lhuillier & Gilder, 2013; Sprain et al., 2019). Recently, Meduri et al. (2021) proposed the first geodynamo simulations capable reproducing the main features of the paleomagnetic field for the past 10 Myr, such as the VGP dispersion parameters, the inclination anomaly (maximum value), and average field intensity.

Despite recent advances in numerical geodynamo modeling, several issues have been raised since the difficulties of establishing boundary conditions imposed by different models, such as computational limitations (for instance, numerical processing and spatial resolution). According to some authors (e.g., Dormy et al., 2000; Glatzmaier, 2002; Kono & Roberts, 2002; Sreenivasan, 2010), these impasses make it difficult to obtain realistic parameters at Earth-like conditions and, consequently a better understanding of the dynamic behavior of the geomagnetic field.

2.1.2 Main geomagnetic field components

The geomagnetic field measured at any point on the Earth's surface can be described by the intensity and direction (Butler, 1998). Through representation of a Cartesian coordinate system, the total intensity vector (**F**) is decomposed by the magnetic elements X, Y, and Z, whose axes are geographically oriented to the north, east and vertically downwards, respectively (Figure 2.1). Thus, two components are used to determine the field direction: (i) the magnetic declination (D) defined as the angle between geographic north and the horizontal component of **F** (= **H**), ranging from 0º to 360º (positive clockwise), and (ii) the magnetic inclination (I) described by the vertical angle of **F** from its horizontal component. By convention I varies between -90º (south magnetic pole) and +90º (north magnetic pole), with values equal to zero at the magnetic equator. The intensity values observed are higher near the magnetic poles (~60 μT) when compared in equatorial regions (~30 μT). The magnetic components are expressed by:

$$X = F\cos I\cos D, \qquad Y = F\cos I\sin D, \qquad Z = F\sin I \tag{2.1}$$

$$H = \sqrt{X^2 + Y^2}, \qquad F = \sqrt{X^2 + Y^2 + Z^2} \tag{2.2}$$

$$D = \arctan\left(\frac{Y}{X}\right), \qquad I = \arctan\left(\frac{Z}{H}\right) \tag{2.3}$$

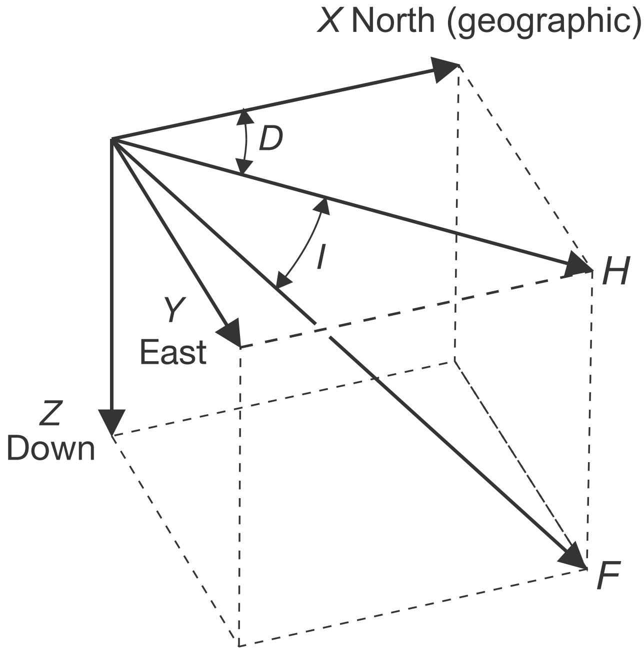

Figure 2.1 – Geomagnetic field components. The total intensity vector F is represented by three magnetic elements: X (northwards), Y (eastwards), and Z (vertical). H corresponds the horizontal component of F. D (declination) and I (inclination) define the magnetic direction. From McElhinny and McFadden (2000).

For the present time, the geomagnetic field structure can be considered, to a first approximation, as a magnetic dipole located at the Earth's center and inclined $\sim 11.5°$ in relation to the geographic axis, with the orientation of the best-fitted dipole changing with time (Butler, 1998). According to Panovska et al. (2019), the dipole field contributes about 90% of the EMF observed at the surface. The two points where inclined magnetic dipole intersects the planet's surface are designated as *geomagnetic poles*, an imaginary line equidistant from these poles is referred to as the *geomagnetic equator*. Geomagnetic poles are completely different from the magnetic poles (Figure 2.2) that correspond to two particular areas where the field is vertical with values of $I = \pm 90°$. The imaginary contour near the geographic equator with inclination values equal to zero is called *magnetic equator* (Butler, 1998).

In the case of a perfect geocentric dipole, the geomagnetic and magnetic poles would coincide with the Earth's spin axis. However, this is not valid since 10% of the geomagnetic field can be attributed to the presence of non-dipole sources. Both the dipole and non-dipole field contributions vary spatially and temporally (Johnson & McFadden, 2015; Merrill et al., 1998). Each of these sources can be obtained through global field models constructed in terms of spherical harmonics coefficients (see Appendix A.1 for further details

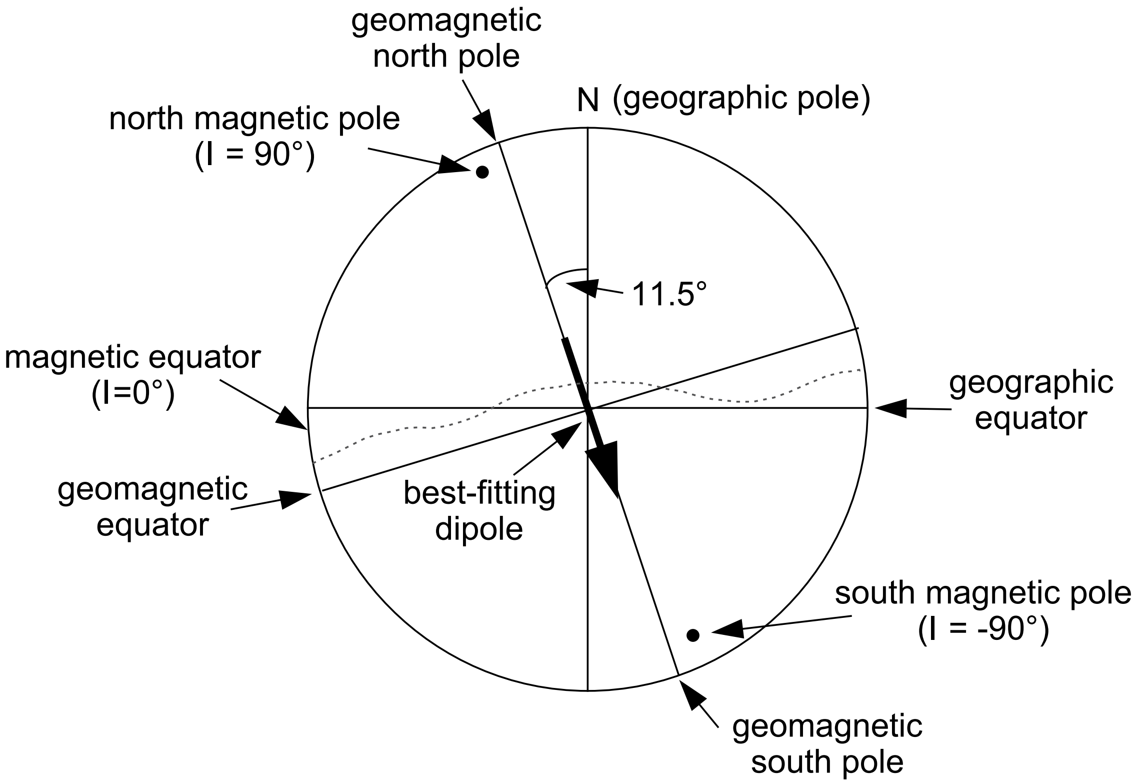

Figure 2.2 – Inclined geocentric dipole indicating the (geo)magnetic poles and equators. Modified from Butler (1998).

of the mathematical description) using data from satellites, magnetic observatories and paleomagnetic records for a particular time interval (Hulot et al., 2010).

2.1.3 Geocentric Axial Dipole Hypothesis

One of the fundamental concepts in paleomagnetism refers to the GAD hypothesis, in which the geocentric dipole coincides with the Earth's rotational axis as long as the mean paleodirection is sufficiently long over a time interval of at least 10^4 years (Merrill & McFadden, 2003). Thus, the paleomagnetic latitude λ is the equivalent to the magnetic latitude (Figure 2.3). For a magnetic moment M and a is the radius of the Earth, the horizontal (H) and vertical (Z) components of the field at any latitude can be determined from the axial dipole term g_1^0 (see Appendix A.2), given by (Butler, 1998):

$$H = \frac{M\cos\lambda}{r^3}, \qquad Z = \frac{2M\sin\lambda}{r^3}, \tag{2.4}$$

The tangent of the magnetic inclination is defined by the Z/H ratio:

$$\tan I = 2\tan\lambda, \tag{2.5}$$

or

$$\tan I = 2\cot\theta \qquad (0° \leq \theta \leq 180°), \tag{2.6}$$

where θ is the paleocolatitude. By definition, the declination is given by:

$$D = 0°. \tag{2.7}$$

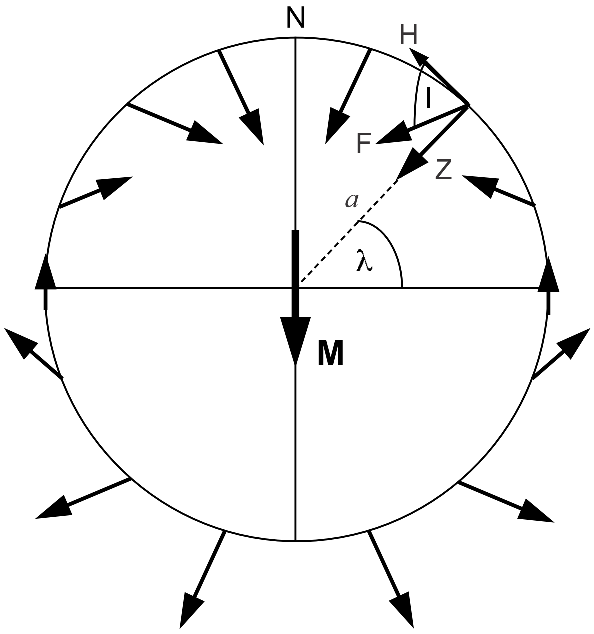

Figure 2.3 – Geomagnetic axial dipole model. Modified from Butler (1998).

The relationship given by Equation (2.5) is usually referred to as the *dipole equation*, which allows the calculation of paleolatitude from the mean inclination. The latter is an estimate of field direction obtained by sampling of various geological units (e.g., a sedimentary sequence, lava flows and dykes) for a given instant of time and locality known as "sites" (Butler, 1998). The Equation (2.5) can be used for different time intervals with applications for plate tectonics and continental reconstructions (McElhinny, 2007). In this context, it is interest in paleomagnetism to determine the paleomagnetic pole position that represents the position of the equivalent geomagnetic pole for a certain geological period. From the mean directions (D_m, I_m) and the geographic coordinates for a given location site (latitude λ_s, longitude ϕ_s), the coordinates of the paleomagnetic pole P (latitude λ_p, longitude ϕ_p) can be calculated from the procedures described below (Figure 2.4). First, the latitude of the paleomagnetic pole is calculated as:

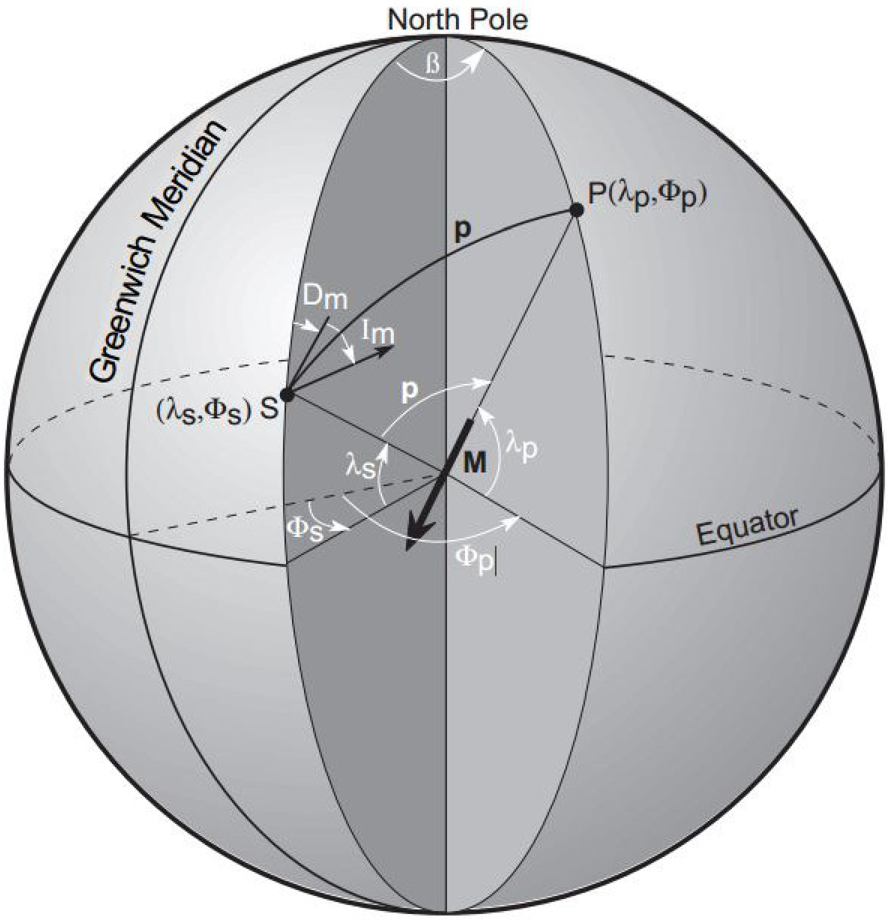

Figure 2.4 – Squematic of the position of a paleomagnetic pole P (λ_p, ϕ_p) calculated from site location at S (λ_s, ϕ_s) and mean magnetic direction (I_m, D_m). **M** represents the geocentric magnetic dipole, p is the paleocolatitude, and β refers the longitudinal difference between pole and site. From Butler (1998).

$$\lambda_p = \sin^{-1}(\sin\lambda_s \cos\theta + \cos\lambda_s \sin\theta \cos D_m) \qquad (-90^\circ \leq \lambda_p \leq +90^\circ), \tag{2.8}$$

where θ is calculated from Equation (2.6). The longitude of the paleomagnetic pole is given by:

$$\phi_p = \phi_s + \beta \qquad \text{when} \cos\theta \geq \sin\lambda_p \sin\lambda_s \tag{2.9}$$

or

$$\phi_p = \phi_s + \pi - \beta \qquad \text{when} \cos\theta < \sin\lambda_p \sin\lambda_s, \tag{2.10}$$

where β represents the longitudinal difference between the paleomagnetic pole and the site, defined by:

$$\beta = \sin^{-1}\left(\frac{\sin\theta \sin D_m}{\cos\lambda_p}\right). \tag{2.11}$$

Using Equations (2.8) to (2.11), any instantaneous paleodirection can be converted to a pole position that is called as a VGP (McElhinny & McFadden, 2000). Thus, the paleomagnetic pole can also be calculated from the average of VGP distributions using the R. A. Fisher (1953) statistics (see Appendix B). An interesting fact is that the VGP angular dispersion with respect to the paleomagnetic pole has provided useful information about the paleosecular variation behavior, as will be discussed in Section 2.3. Furthermore, the geographic distribution of continuous VGP records allows investigations into the geomagnetic polarity reversals over geological timescale.

2.1.4 Geomagnetic reversals

The geomagnetic polarity reversals are characterized by drastic changes in the field direction arising from the internal processes of the Earth's core dynamics (Korte & Mandea, 2019). Considering the best-fitting dipole to the geomagnetic field, a polarity reversal is related to an alternation of the geomagnetic poles (i.e., north and south geomagnetic poles swap positions) and involves changes of 180° in magnetic declination and the magnetic inclination sign (McElhinny & McFadden, 2000; Tauxe, 2010). It is a globally synchronous event and provides a means of performing stratigraphic correlations and dating (Lowrie, 2007).

These events are mainly observed in seafloor magnetic anomaly records and magnetostratigraphic studies from sedimentary and volcanic rocks (McElhinny & McFadden, 2000). Based on the known reversals recorded, the geomagnetic polarity time scale (GPTS) was constructed and shows the succession of polarity intervals over time. By convention, periods with the same polarity as the actual geomagnetic field are termed *normal*, while periods with opposite polarity are termed *reverse* (Cormier et al., 2022).

When examining the duration of geomagnetic polarity intervals, the GPTS indicates that average reversal frequency varies considerably during Phanerozoic times (Figure 2.5). The reversal rate is about 5 times/Myr for the 0-10 Ma interval, and the last reversal occurred 0.78 Ma ago (Lowrie, 2007). Long periods of 10^7-10^8 years of stable polarity (absent reversal regimes) are termed *superchons*. As shown Figure 2.5, there are three superchons documented in the literature, the Cretaceous Normal Superchron (CNS; 124-83 Ma; Ogg, 2020), Permo-Carboniferous (Kiaman) Reversed Superchon (PCRS; 318-265 Ma; Opdyke & Channell, 1996), and the Moyero Reversed Superchon (480-460 Ma; Pavlov & Gallet, 2005). The term *chron* refers to intervals of constant polarity of 10^6-10^7 years. Eventually, a *chron* can be interrupted by short intervals of opposite polarity called as *subchrons* of 10^5-10^6 years (McElhinny & McFadden, 2000). The first four chrons were named after the pioneers of geomagnetism (Brunhes, Matuyama, Gauss and Gilbert), whereas the subchrons were labeled based on geographical location of their discoveries (e.g., Jaramilo, Olduvai, Kaena, etc.). The GPTS for the last 6 Myr suggested by Ogg (2020) is displayed in Figure 2.6.

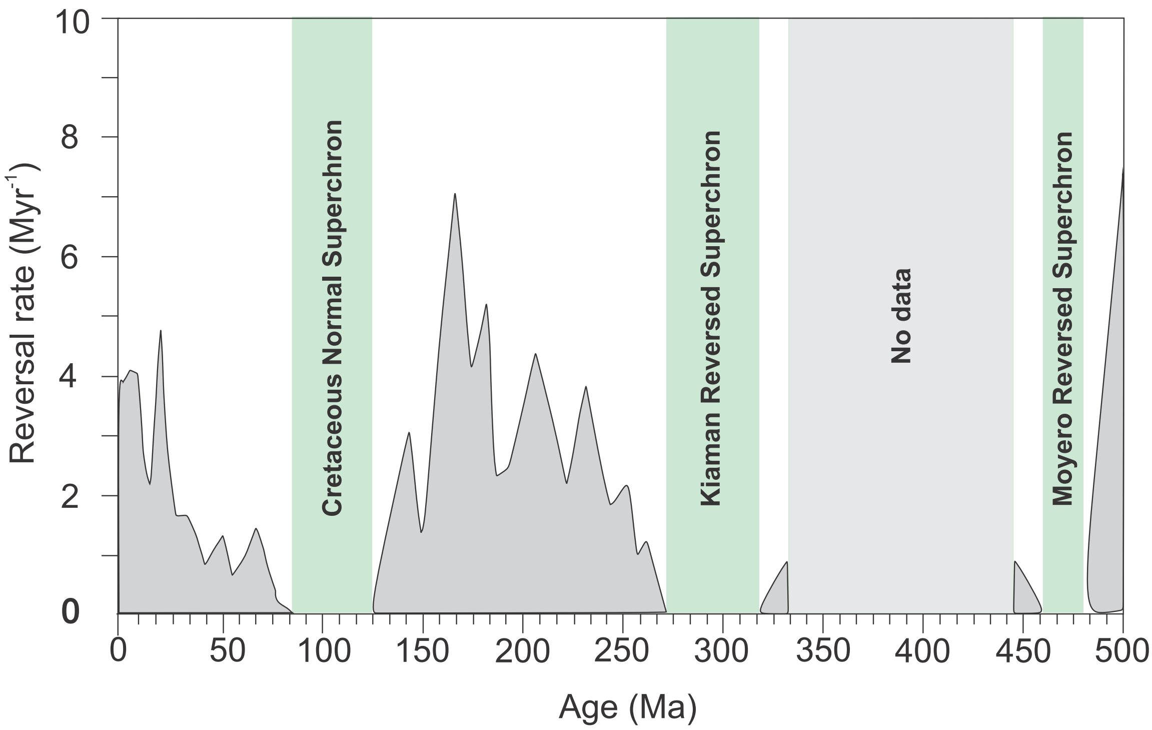

Figure 2.5 – Variations in geomagnetic reversal frequency for the last 500 Myr. Modified from Pavlov and Gallet (2005).

On certain occasions, the geomagnetic field does not exhibit a full change in polarity, the magnetic poles move towards intermediate latitudes, but return to their original position. These episodes are referred to as *geomagnetic excursions* with a duration of $\sim 10^4$ years. They are generally considered in cases where the VGP locations have latitudes less than 45° (A. P. Roberts, 2008). An issue that has been debated concerns the geomagnetic field behavior during a polarity transition (Buffett, 2015; Valet & Fournier, 2016). Paleomagnetic records reveal that these phenomena are associated with a significant reduction in magnetic intensity (e.g., Channell et al., 2009; Valet et al., 2005; Ziegler et al., 2011). Some studies (e.g., M. C. Brown et al., 2007; Guyodo et al., 1999; Merrill & McFadden, 1994) suggest that dominant non-dipole components influence the minimum field intensity during reversals and excursions. Conversely, some authors (e.g., Kent & Schneider, 1995; Kutzner & Christensen, 2004; Laj et al., 2006) argued that intensity decreases due to the reduction of the dipole field.

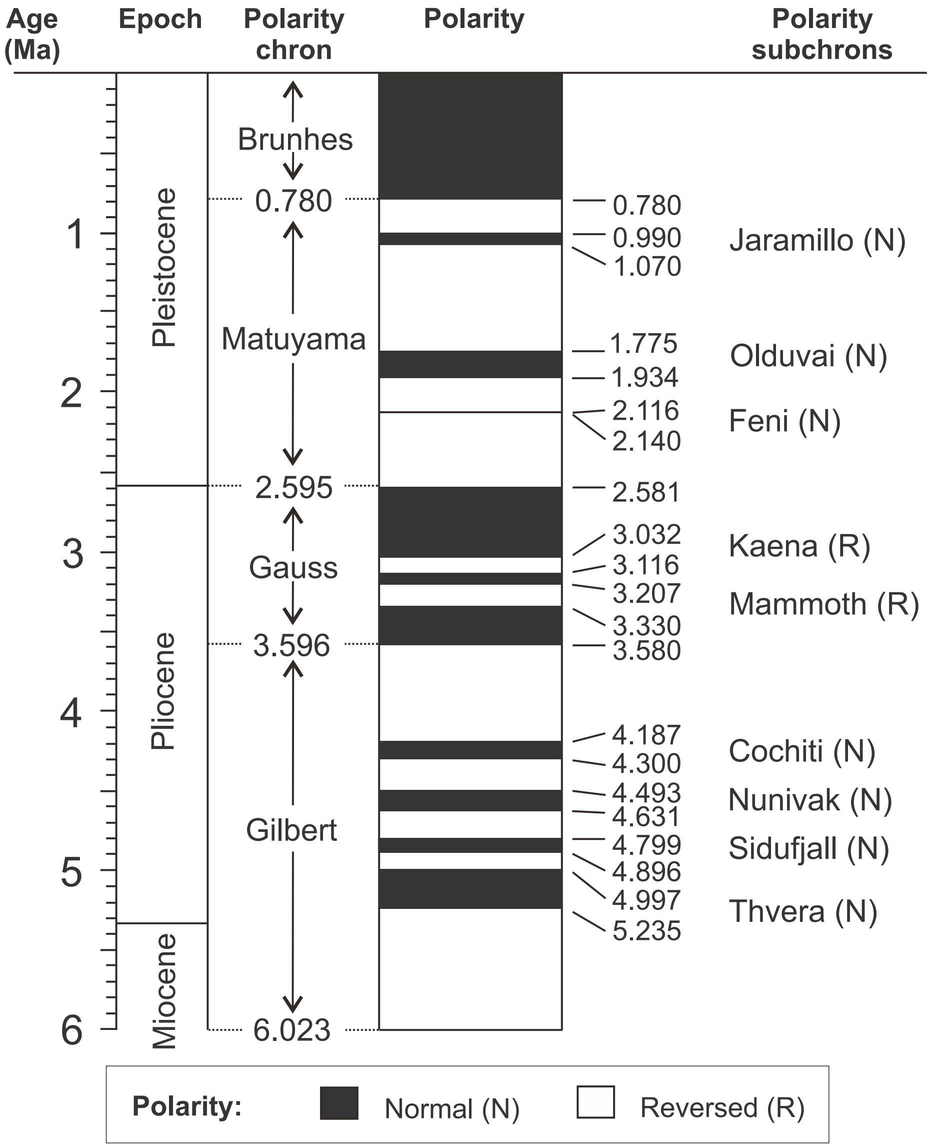

Figure 2.6 – Geomagnetic polarity time scale for the 0-6 Ma interval. Modified from Ogg (2020).

Furthermore, it was pointed out (Clement, 1991; Laj et al., 1991; Love, 1998; McFadden et al., 1993) that the transitional fields seem to define two preferential longitudinal bands for VGP paths, over the Americas and eastern Asia (Figure 2.7). Interestingly, these areas coincide with high seismic wave speeds in the lower mantle (Laj et al., 1991) and have been observed by some geodynamo models (e.g., Costin & Buffett, 2004; Glatzmaier et al., 1999; Kutzner & Christensen, 2004; Olson & Christensen, 2002), assuming lateral variability in the CMB heat flux.

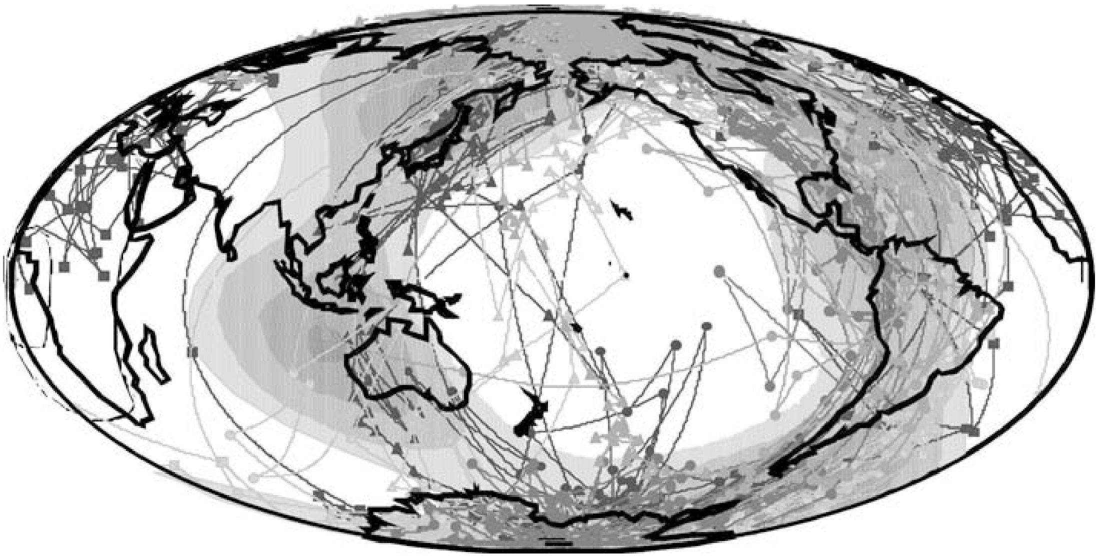

Figure 2.7 – Map showing the two preferred longitudinal sectors for transitional VGPs (black dots). The gray shaded areas indicate the high-velocity regions of seismic waves in the lower mantle. From Laj et al. (1991).

2.2 Paleomagnetic databases over the past 10 Myr

Over timescales of million years, paleodirectional data (D and I) are essentially obtained through indirect measurements on geological materials. Particularly, lava flow data are considered more suited for statistical assessments of the paleofield variability because they provide geologically instantaneous records of the geomagnetic field direction, acquired by a process called thermoremanent magnetization (Butler, 1998; Johnson & McFadden, 2015). In contrast, sedimentary materials reveal temporal smoothed records due to acquisition of detrital remanent magnetization (Aubert et al., 2010).

The 0-5 Ma time interval is the most widely investigated compared to older periods, given a great quantity of paleomagnetic data available and the tectonic plate motions are not significant (Hulot et al., 2010). In this period, several paleodirectional databases from lava flows have been proposed and used to construct PSV and TAF models (Johnson & McFadden, 2015). These compilations differ by the inclusion of new data and the selection criteria employed, such as demagnetization procedures, exclusion of transitional data (or outlier data) applying some VGP cutoff value, sufficient number of specimens measured at the site level, and a certain parameter value by R. A. Fisher (1953) statistics (e.g., Fisher precision parameter, k, and the 95% confidence cone, α_{95}). An overview of Fisher's statistic is provided in Appendix B.

The database suggested by McElhinny and McFadden (1997) (hereafter MM97) consists of 3,719 lava flows and thin dykes from previous datasets (e.g., Johnson & Constable, 1996; Lee, 1983; McElhinny & Merrill, 1975; Quidelleur et al., 1994). The purpose this database was to be as comprehensive as possible, and therefore, the data collection included paleomagnetic studies with at least five sites ($N \geq 5$), a minimum number of two specimens per site ($n \geq 2$), the α_{95} for site-mean directions should be <20°, and any laboratory demagnetization procedure for determining the primary magnetization component. A demagnetization code, called *Demagcode* (DC), was attributed to all sites to assess data quality and the experimental procedures used. This code varies on the scale between 0 and 5 as summarized in Table 2.1. In addition, only sites with VGP latitudes greater than 45° were acc-

Table 2.1 – Description of Demagnetization Codes (DC). From McElhinny and McFadden (2000).

DC	Description
0	No demagnetization carried out. Only Natural remanent magnetization (NRM) values reported.
1	Pilot demagnetizations on some samples suggest stability. Only NRM values reported.
2	Bulk demagnetization carried out on all samples. No supply vector diagrams.
3	Vector diagrams or stereoplots with M/M_0 justify demagnetizaton procedures used.
4	Principal component analysis (PCA) carried out from analysis of Zijderveld diagrams.
5	Magnetic vectors isolated using two or more demagnetization methods (e.g., (alternating Field and thermal) with PCA.

M/M_0 is the ratio between measured remanent magnetization and initial magnetization.

epted. MM97 suggested that most previous studies should be replaced by new data, with a DC = 4 to remove secondary magnetization components. Using this code, the MM97 dataset is reduced to 394 paleodirectional sites. Subsequently, the compilations require modern laboratory methods to obtain reliable data.

Johnson et al. (2008) proposed the first high-quality 0-5 Ma dataset from 17 different locations combined with 8 regional compilations (Figure 2.8a), according to the following selection criteria: (i) studies that have at least ten sites $N \geq 10$, (ii) a value of $n \geq 5$ with an estimated Fisher precision parameter of $k \geq 50$ for each site, (iii) the site-mean directions defined with DC ≥ 4, and (iv) exclusion of sites with VGP latitudes lower than 45°. This database contains 2,107 paleomagnetic sites and offers a latitudinal coverage between 78°S and 53°N. Nonetheless, the data are mainly clustered over the Americas. The temporal distribution of these data is concentrated in the Brunhes (67%) and Matuyama (26%) chrons.

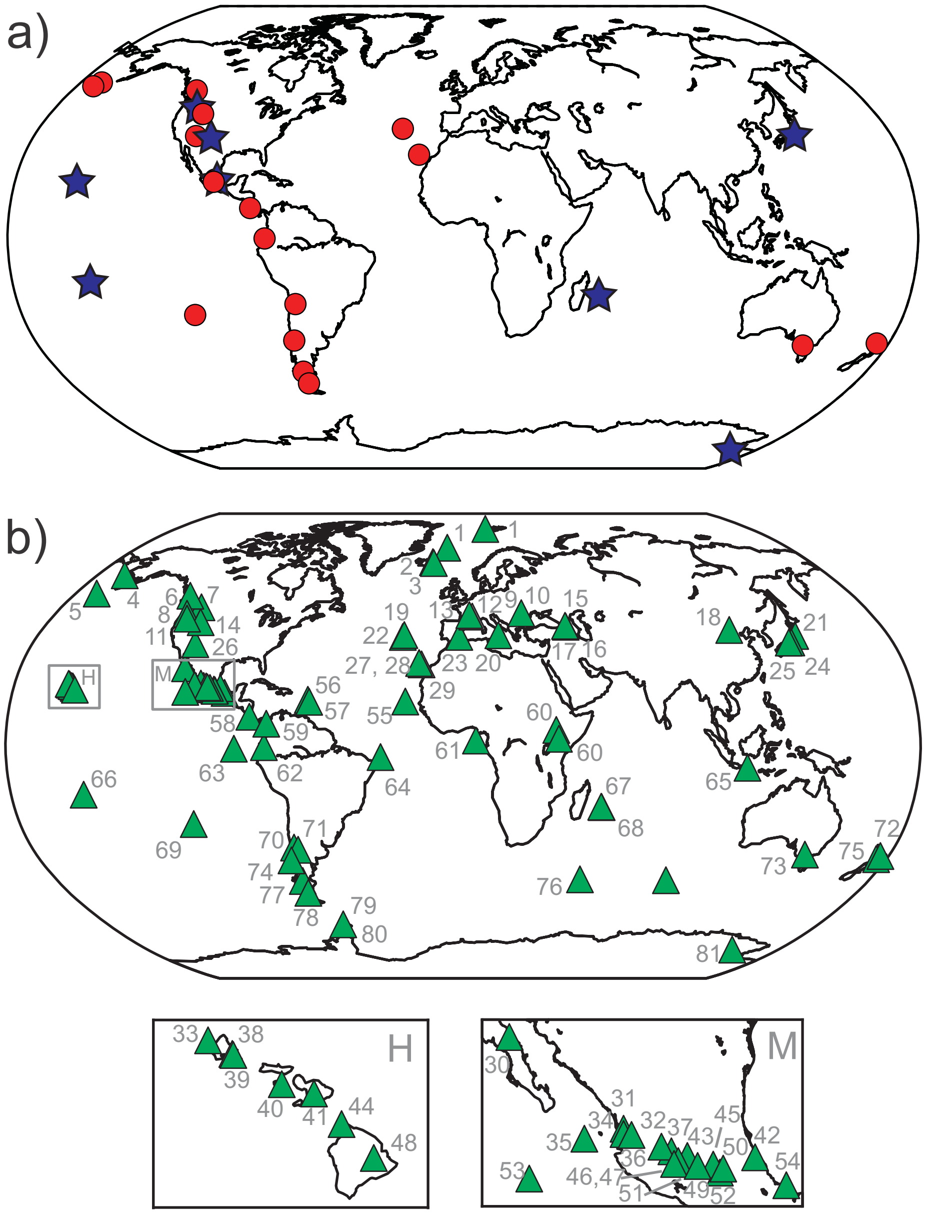

Figure 2.8 – Map with the location of paleomagnetic sites. (a) Database for the 0-5 Ma interval suggested by Johnson et al. (2008). The red circles (blue stars) indicate the locations of selected paleomagnetic studies (regional compilations). (b) Study locations (green triangles) from PSV10 dataset. Numbers correspond to the references reported in Table 2 of Cromwell et al. (2018). Modified from Cromwell et al. (2018).

Recently, Cromwell et al. (2018) presented a new paleodirectional database spanning the last 10 Myr (hereafter PSV10) that comprises 2,401 sites from the collection of 81 paleomagnetic studies published between 1989 and 2017. This compilation differs from the selection criteria used by Johnson et al. (2008), using a value of $n \geq 4$ and does not require a minimum number of sites for each selected study. Regarding geographic sampling, the data are unevenly distributed between both hemispheres, as shown in Figure 2.8b. The Southern Hemisphere contributes only 25% of the PSV10 dataset.

Therefore, the acquisition of new paleomagnetic data is crucial for a better understanding of the paleofield behavior over the past 10 Myr. Especially for statistical studies that assess the latitudinal structure and evolution of the paleomagnetic field from VGP dispersion and inclination anomaly estimates in a broad interhemispheric coverage.

2.3 Paleosecular Variation

2.3.1 Fundamental concepts

PSV is usually used to describe long-period variations of the field (10^5–10^6 years) during stable regimes of geomagnetic polarity (Johnson & McFadden, 2015). On these timescales, geomagnetic variability can be ascribed to geodynamo processes as well as thermal CMB conditions (Biggin et al., 2012; Driscoll & Olson, 2011; R. Heller et al., 2002; Olson et al., 2010). PSV is observable at the Earth's surface from changes in field direction and geomagnetic pole position over time (Figura 2.9). Information about PSV behavior is essential for a better assessment of the temporal geomagnetic field evolution and constraints on numerical geodynamo models (e.g., Biggin et al., 2020; Coe & Glatzmaier, 2006; Davies et al., 2008; Lhuillier & Gilder, 2013; Meduri et al., 2021; Olson et al., 2014; Sprain et al., 2019).

Long-term geomagnetic variations detected in sedimentary rocks can provide continuous records of the paleomagnetic field. Conversely, lava flows offer instantaneous reading of the paleofield and are therefore considered highly suitable for statistical studies of the geomagnetic variability, commonly referred to as *paleosecular variation from lavas* (PSVL; Merrill et al., 1998). PSV is traditionally assessed by angular dispersion (S) of VGP data, expressed by (Cox, 1970):

$$S = \sqrt{\frac{1}{N-1}\sum_{i=1}^{N}\Delta_i^2}, \tag{2.12}$$

where N is the total number of sites and Δ_i is the angular distance of the ith VGP from paleopole or geographic pole. The best PSV estimate is expressed by the between-site VGP dispersion (S_B), generally used to remove errors caused in the sampling process and experimental measurements, then the S_B dispersion is calculated as:

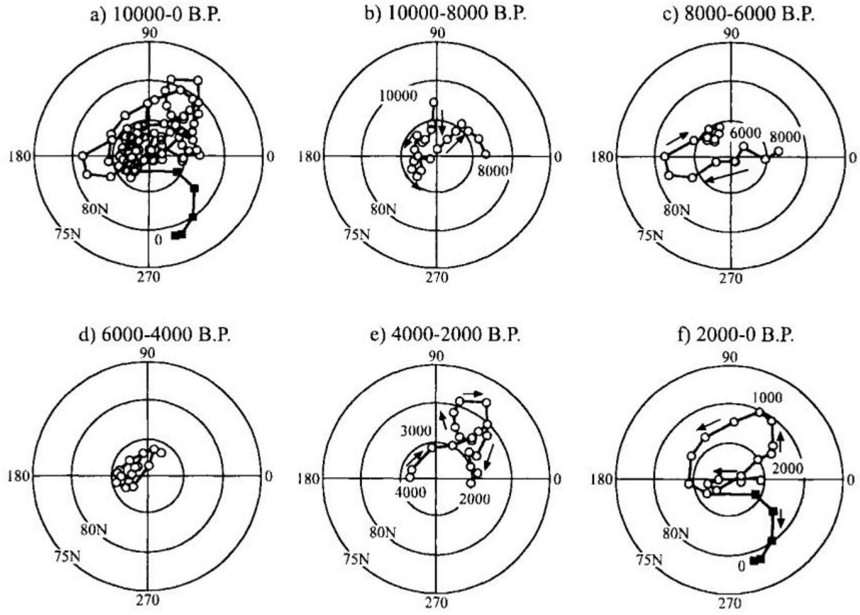

Figure 2.9 – (a) Location of the north geomagnetic pole for the last 10,000 years. (b)-(f) Geomagnetic pole positions for each 2000 year intervals. The dots represent the pole positions at 100 year intervals. From McElhinny and McFadden (2000).

$$S_B = \sqrt{S^2 - \frac{S_w^2}{\bar{n}}}, \tag{2.13}$$

where $\bar{n}$ is the average number of samples at each site. The correction factor for the within-site VGP dispersion ($S_W^2/\bar{n}$) can be determined as follows (McElhinny & McFadden, 1997):

$$\frac{S_w^2}{\bar{n}} = 0.335\bar{\alpha}_{95}^2 \frac{2(1+3\sin^2\bar{\lambda})^2}{(5+3\sin^2\bar{\lambda})}. \tag{2.14}$$

Equation (2.14) depends on the $\bar{\alpha}_{95}$ (mean α_{95} for a given dataset) and $\bar{\lambda}$ is the site mean latitude. According to some studies (e.g., de Oliveira et al., 2018; Haldan et al., 2009), $S_w^2/\bar{n}$ is relatively small with an increase of 1°-2° in VGP dispersion when the correction factor is not applied.

2.3.2 Paleosecular Variation Models

Paleosecular variation models have been developed to describe the latitudinal behavior of VGP dispersion, and are differentiated by the statistical approaches and the time interval evaluated. The first models are designated as *parametric*, in which the angular dispersion of field directions or VGPs as a function of latitude are described by considering three sources (Johnson & McFadden, 2015):

(i) variations in the geomagnetic dipole orientation (dipole wobble);
(ii) variations in the intensity of the dipole wobble;
(iii) changes in the intensity and direction of the non-dipole field.

The parametric models constructed follow the terminology defined by Irving (1964). For a detailed description of these models see Merrill et al. (1998). Overall, the oldest PSV models considered only dipole wobble effects, models: A (Irving & Ward, 1964) and B (Creer, 1962; Creer et al., 1959) , and were succeeded by models that considered the combination the dipole wobble and non-dipole field sources, models: C (Cox, 1962), D (Cox, 1970), E (Baag & Helsley, 1974), F (McFadden & McElhinny, 1984), and M (McElhinny & Merrill, 1975).

The models mentioned above were gradually discarded as new PSV studies were presented. Currently, PSV models allow evaluation of the latitudinal variation of VGP dispersion based on spherical harmonic descriptions of the present geomagnetic field. Grounded in this premise, Model G (McFadden et al., 1988) and Giant Gaussian Process (GGP) models (Constable & Parker, 1988) are the two main types of statistical PSV models, as discussed in the next sections.

2.3.2.1 Model G

The phenomenological Model G was proposed by McFadden et al. (1988) supported by a theoretical study concerning the geodynamo (P. H. Roberts & Stix, 1972). This model assumes that magnetic field solutions can be separated into two independent families, known as primary (or antisymmetric) and secondary (or symmetric) families, represented by spherical harmonic terms of degree l and order m. In primary family, the Gauss coefficients (g_l^m and h_l^m) produce fields that are antisymmetric about the equator (with $l - m$ = odd), whereas the secondary family the fields are symmetric with respect the equator (with $l - m$ = even). The spherical harmonic coefficients assigned to these two dynamo families are shown in Table 2.2.

McFadden et al. (1988) demonstrated that the separation of these two families can be a useful resource to explain the observed latitudinal pattern of VGP dispersion. Thus, the

Table 2.2 – Spherical harmonic coefficients for primary and secondary families. From McFadden et al. (1988).

Field	**Primary Family**	**Secondary Family**
Dipole	g_1^0	g_1^1, h_1^1
		g_2^0
Quadrupole	g_2^1, h_2^1	g_2^2, h_2^2
Octupole	g_3^0	g_3^1 h_3^1
	g_3^2, h_3^2	g_3^3, h_3^3

total VGP dispersion (S) can be described approximately by the quadrature sum of the contributions of the primary (S_P) and secondary (S_S) families, as follows:

$$S(\lambda) \simeq \sqrt{(S_S)^2 + (S_P)^2}. \tag{2.15}$$

Model G was originally designed based on spherical harmonic description using the IGRF65 model (International Reference Geomagnetic Field model for 1965). Further, S can be expressed through two shape parameters a and b, respectively, which are related to the secondary and primary families. The relationship is given by:

$$S(\lambda) = \sqrt{a^2 + (b\lambda)^2}. \tag{2.16}$$

where a ($= S_S$) and b ($= S_P/\lambda$) are determined from the curve fitted to the VGP scatter data by the least squares method. According to this approach the dispersion caused by the secondary family is constant with latitude, while the contribution relative to the primary family varies linearly as a function of λ (Figure 2.10).

McFadden et al. (1988) applied Model G to paleomagnetic data for the 0-5 Ma interval (McFadden & McElhinny, 1984), and observed a similarity in the VGP dispersion curve from this period in relation to the IGRF65 model. Nevertheless, Hulot and Gallet (1996) showed that latitudinal variation of VGP dispersion for earlier historical periods (1800, 1900 and 1980) are significantly different from each other and from the 0-5 Ma paleomagnetic field. Although a physical description of the Model G has not been clearly elucidated, this model has been widely used in PSV studies from Archean to Phanerozoic times (e.g., Biggin et al., 2008a; Biggin et al.,

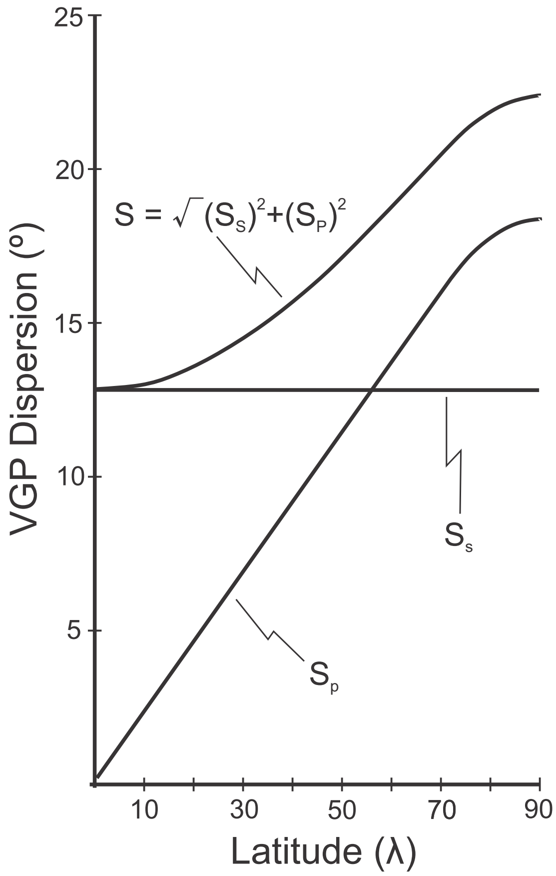

Figure 2.10 – Schematic representation of Model G. Modified from McFadden et al. (1991).

2008b; de Oliveira et al., 2018; Doubrovine et al., 2019; Franco et al., 2019; Handford et al., 2021; Johnson et al., 2008; Smirnov et al., 2011; Veikkolainen & Pesonen, 2014), providing information regarding paleomagnetic field stability (Coe & Glatzmaier, 2006).

A relationship between VGP dispersion patterns and geomagnetic reversal frequency was pointed out by McFadden et al. (1991) through analyses of distinct intervals over the last 195 Myr, using database of Lee (1983). The authors suggested that periods of low reversal rates exhibit a pronounced latitudinal dependence of Model G curve (with lower and higher values for parameters *a* and *b*, respectively) compared to periods of high reversal rates. Recent studies of extreme reversal events have revealed the occurrence of this behavior for two superchons, the PCRS (de Oliveira et al., 2018; Handford et al., 2021) and CNS (Doubrovine et al., 2019) intervals. On the other hand, there are high frequency reversal regimes investigated during the Illawarra Hyperzone of Mixed Polarity (IHMP; 266.7–228.7 Ma; Franco et al., 2019), the Post-PCRS (200-264 Ma; Handford et al., 2021) and Pre-CNS (127-198 Ma; Doubrovine et al., 2019) intervals. However, Doubrovine et al. (2019) disputed the link between PSV and average reversal frequency, given the similarity among the strong latitudinal dependence of the VGP dispersion curves for the superchons (PCRS and CNS) and the 0-5 Ma and 0-10 Ma intervals (with ~4.4-4.8 Myr^{-1}). Furthermore, temporal evolution of Model G parameters (Table 2.3) is not consistent with the with the hypothesis of a inverse correlation between b/a ratio and reversal frequency suggested by Coe and Glatzmaier (2006). Variations in b/a ratio from different PSV studies for the Phanerozoic times are shown in Figure 2.11 .

Table 2.3 – Values of the Model G parameters a_l^u and b_l^u (where $u(l)$ are the upper (lower) bounds for shape parameters) from PSV studies throughout the Phanerozoic.

Event	Age interval (Ma)	average reversal rate (Myr^{-1})	$a_l^u(^\circ)$	b_l^u	$b/a\,(1/^\circ)$	Study
PCRS	265 - 318	0.08	$9.4_{7.5}^{10.9}$	$0.27_{0.22}^{0.29}$	$0.029_{0.021}^{0.037}$	1
PCRS	265 - 318	0.08	$5.5_{0.8}^{8.6}$	$0.33_{0.24}^{0.42}$	$0.059_{0.007}^{0.111}$	2
IHPM	229 - 267	5.9	$13.2_{6.8}^{16.3}$	$0.12_{0.11}^{0.13}$	$0.009_{0.004}^{0.014}$	3
Post-PCRS	200 - 264	2.0	$14.2_{13.3}^{18.1}$	$0.15_{0.05}^{0.27}$	$0.011_{0.004}^{0.018}$	2
Jurassic	145 - 200	4.6	$16.4_{10.3}^{19.0}$	$0.19_{0.00}^{0.46}$	$0.012_{0.000}^{0.028}$	4
Pre-CNS	127 - 198	3.1	$12.7_{10.0}^{14.6}$	$0.13_{0.00}^{0.26}$	$0.010_{0.002}^{0.018}$	5
CNS	84 - 126	0.1	$10.7_{8.3}^{12.9}$	$0.21_{0.00}^{0.26}$	$0.020_{0.001}^{0.032}$	4
CNS	84 - 126	0.1	$8.7_{6.3}^{10.7}$	$0.27_{0.22}^{0.31}$	$0.031_{0.021}^{0.041}$	5
Last 10 Ma	0 - 10	4.8	$11.3_{10.2}^{12.6}$	$0.27_{0.19}^{0.31}$	$0.024_{0.016}^{0.031}$	6
Last 5 Ma	0 - 5	4.4	$11.6_{10.3}^{13.0}$	$0.26_{0.22}^{0.29}$	$0.022_{0.018}^{0.027}$	7
Last 5 Ma	0 - 5	4.4	$14.5_{12.8}^{16.0}$	$0.20_{0.12}^{0.26}$	$0.014_{0.008}^{0.020}$	8

References: 1. de Oliveira et al. (2018); 2. Handford et al. (2021); 3. Franco et al. (2019); 4. Biggin et al. (2008b); 5. Doubrovine et al. (2019); 6. Cromwell et al. (2018); 7. Opdyke et al. (2015); 8. Johnson et al. (2008).

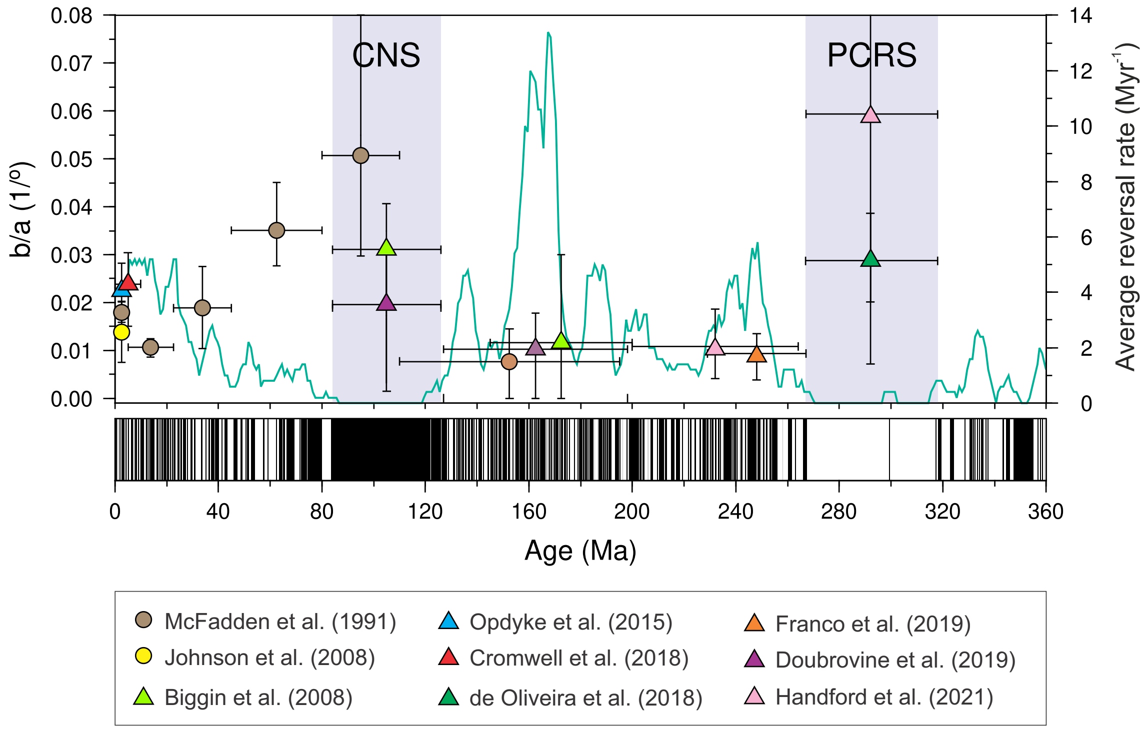

Figure 2.11 – Variations in b/a ratio from paleolecular variation studies covering Phanerozoic times, associated with the geomagnetic polarity time scale of Ogg (2020). Circles and triangles denote the best estimates for Model G parameters provided by studies applying a fixed (45° or 40°) and Vandamme (1994) VGP cutoffs, respectively. The green curve represents the average reversal rate suggested by Doubrovine et al. (2019). The violet areas indicate the CNS (Cretaceous Normal Superchron) and PCRS (Permo-Carboniferous Reverse Superchron) intervals. VGP = virtual geomagnetic pole. Modified from Doubrovine et al. (2019).

2.3.2.2 Model G: Paleosecular variation studies for the last 10 Myr

There is a large number of studies that assess the latitude PSV behavior for the past 5 Myr (e.g., Johnson & Constable, 1996; McElhinny & McFadden, 1997; McFadden et al., 1988; McFadden et al., 1991). From 2008 onward, three high-quality paleomagnetic datasets have been proposed for the 0-5 Ma (Johnson et al., 2008; Opdyke et al., 2015) and 0-10 Ma (Cromwell et al., 2018) intervals. Model G curves fitted to S_B data from these three compilations, suggested by Doubrovine et al. (2019), are illustrated in Figure 2.12.

By comparing the VGP dispersion curves, a close correspondence is observed between best-fit models for the S_B data of Opdyke et al. (2015) and Cromwell et al. (2018), with a strong latitudinal dependence of S_B. In contrast to the low latitudinal variation of Model G curve for the compilation of Johnson et al. (2008). As addressed by Doubrovine et al.

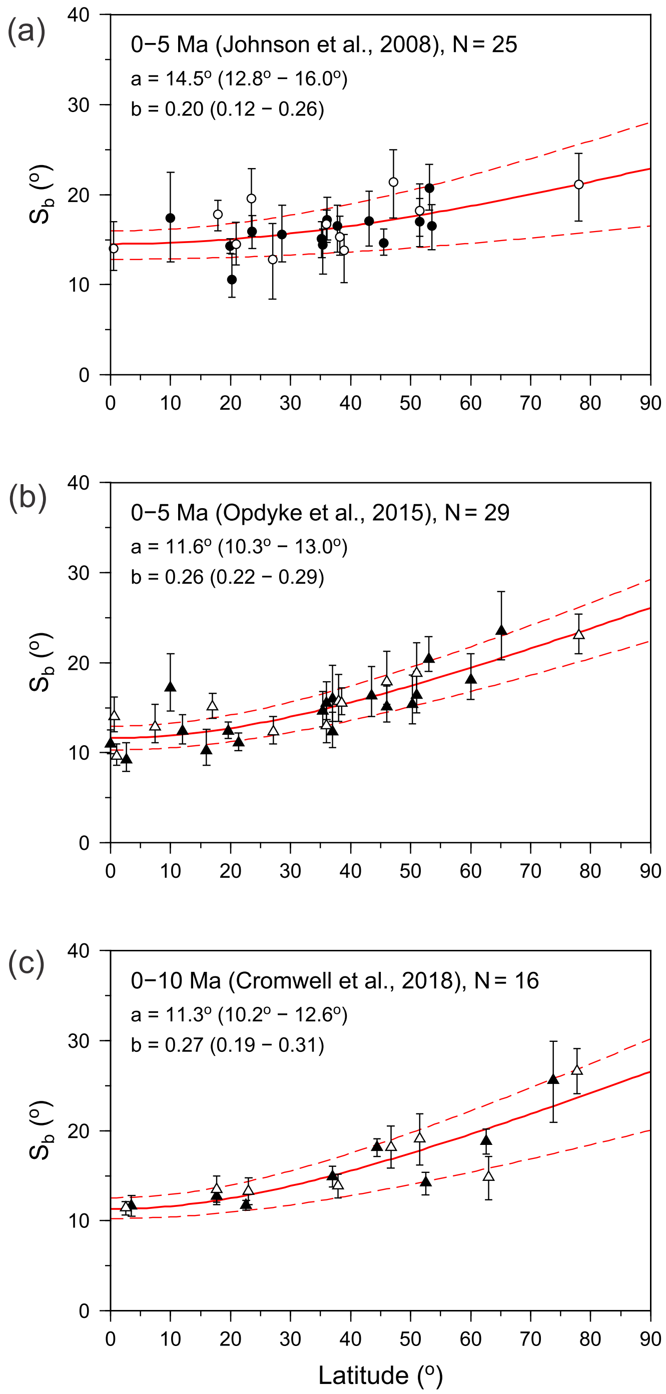

Figure 2.12 – VGP dispersion (S_B) as a function of latitude for three datasets: (a) 0-5 Ma (Johnson et al., 2008), (b) 0-5 Ma (Opdyke et al., 2015), and 0-10 Ma (Cromwell et al., 2018). The red line is the Model G curve with its 95% confidence intervals (dashed lines). N is the number of data used to fit the Model G (McFadden et al., 1988). VGP = virtual geomagnetic pole. Modified from Doubrovine et al. (2019).

(2019), the differences in the shapes of the VGP dispersion curves of these studies are related to the latitudinal coverage of S_B data and the statistical approaches used. Johnson et al. (2008) and Opdyke et al. (2015) determined S_B estimates at the locality level (i.e., for each dataset individually), applying the fixed 45° and Vandamme (1994) VGP cutoffs, respectively. Alternatively, Cromwell et al. (2018) obtained S_B values from data groups separated by 10º latitude bands. For further details about Vandamme (1994) criterion see Appendix C.

2.3.2.3 Giant Gaussian Process Models

GGP models offer a different statistical treatment capable of predicting the distribution of paleomagnetic field vectors (e.g., directional, intensity, and VGP dispersion data) in any geographic position. PSV is described by the statistical variability of each Gauss coefficient from a distribution of normal random variables (Johnson & McFadden, 2015). All non-dipole coefficients have mean zero, the exception applies to some models that assume non-null mean values for the axial quadrupole ($\bar{g}_2^0$) and octupole ($\bar{g}_3^0$) terms. This statistical approach was first introduced by CP88 model of Constable and Parker (1988), who considered the spatial energy spectrum (Lowes, 1974) of the modern magnetic field using the MAGSAT satellite measurements (Langel et al., 1980). CP88 model assumes that the variances ($\sigma_l^{m^2}$) of the Gaussian coefficients are a function of degree l and a parameter α, given by:

$$\sigma_l^{m^2} = \frac{(c/a)^2 l \alpha^2}{(l+1)(2l+1)}, \tag{2.17}$$

where c/a (= 0.547) is the ratio between the Earth's core radius ($c \approx$ 3.486 km) and the Earth's surface radius ($a \approx$ 6.371 km). The CP88 model parameters values are presented in Table 2.4.

Table 2.4 – Statistical parameter values for GGP models.

Parameters	**CP88**	**CJ98**	**QC96**	**TK03.GAD**	**BB18**	**BB18.Z3**	**BCE19**
$\bar{g}_1^0$	$-30.0\mu T$	$-30.0\mu T$	$-30.0\mu T$	$-18.0\mu T$	$-22.04\mu T$	$-22.04\mu T$	$-18.0\mu T$
$\bar{g}_2^0$	$-1.8\mu T$	$-1.5\mu T$	$-1.2\mu T$	0	0	$-0.65\mu T$	0
$\bar{g}_3^0$	0	0	0	0	0	$0.29\mu T$	0
α	$27.7\mu T$	$15.0\mu T$	$27.7\mu T$	$7.5\mu T$	$12.25\mu T$	$12.25\mu T$	$6.7\mu T$
β	1	1	1	3.8	2.82	2.82	4.2
σ_1^0	$3.0\mu T$	$11.72\mu T$	$3.0\mu T$	$6.4\mu T$	$10.80\mu T$	$10.74\mu T$	$6.3\mu T$
σ_1^1	$3.0\mu T$	$1.67\mu T$	$3.0\mu T$	$1.7\mu T$	-	-	$1.5\mu T$
σ_2^0, σ_2^2	$2.14\mu T$	$1.16\mu T$	$1.3\mu T$	$0.6\mu T$	-	-	$0.5\mu T$
σ_2^1	$2.14\mu T$	$4.06\mu T$	$4.3\mu T$	$2.2\mu T$	-	-	$2.2\mu T$
cov	-	-	-	-	$l \leq 4$	$l \leq 4$	-

Subsequently, the models QC96 (Quidelleur & Courtillot, 1996), CJ98 (Constable & Johnson, 1999), and TK03 (Tauxe & Kent, 2004) suggested changes in parameter values and approaches of the CP88 model (Table 2.4), aimed at a better fit to the VGP dispersion data. Thus, it would be possible to observe the latitudinal dependence of VGP dispersion where the CP88 model was unable to predict this behavior (Figure 2.13). However, such models were developed to examine PSV for the last 5 Myr using different paleomagnetic databases. In particular, TK03 model fits the VGP dispersion as a function of latitude from the MM97 database. This model is described based on three parameters: (i) $\bar{g}_1^0$, term estimated by the average field intensity from the global dataset of Selkin and Tauxe (2000) for the 0-5 Ma interval, (ii) α, parameter defined by the CP88 model, and (iii) β', parameter that expresses the ratio of standard deviations of antisymmetric terms to symmetric terms for a given degree.

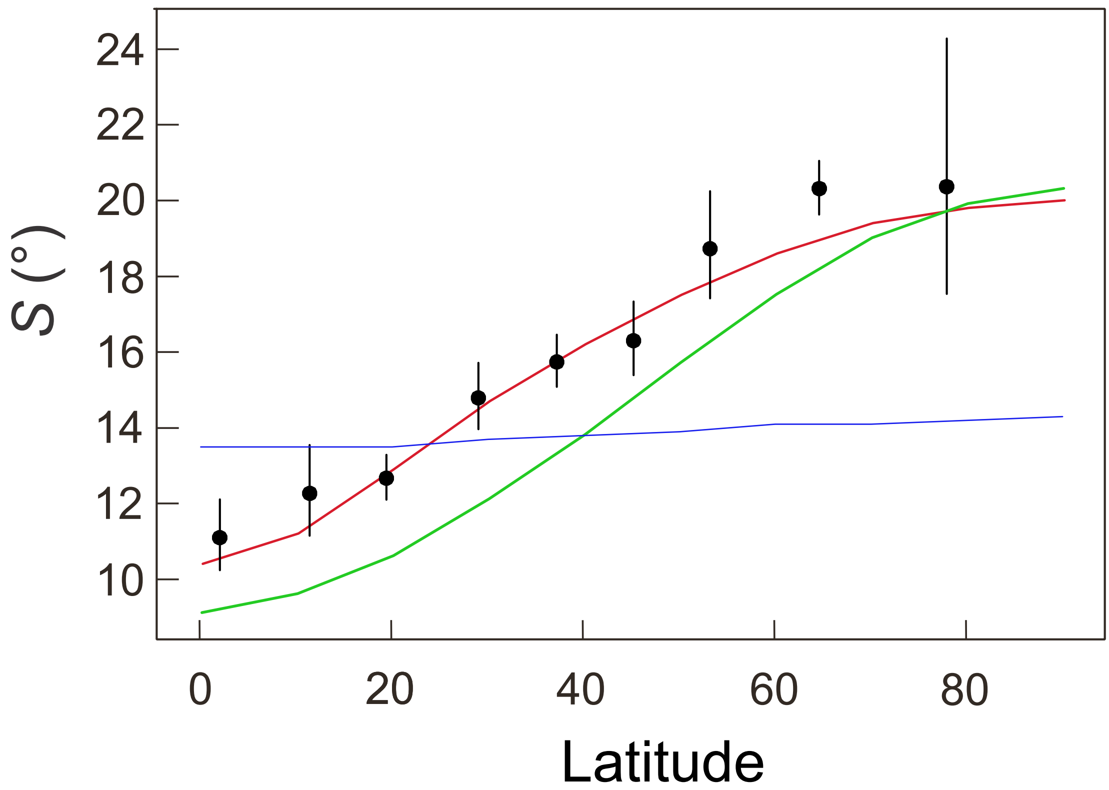

Figure 2.13 – VGP dispersion (S) as a function of latitude for MM97 dataset (McElhinny & McFadden, 1997) represented by black circles. Also shown are VGP dispersions predicted for three GGP models: CP88 (blue curve) of Constable and Parker (1988), CJ98 (green curve) of Constable and Johnson (1999), and TK03.GAD (red curve) of Tauxe and Kent (2004). Modified from Tauxe and Kent (2004).

2.3.2.4 GGP Models developed for the last 10 Myr

Recently, two GGP models named BCE19 (Brandt et al., 2020) and BB18-family models (Bono et al., 2020) were developed to assess the latitudinal PSV behavior for the 0-10 Ma period from the PSV10 dataset.

BCE19 Model: This model was constructed from paleodirection data analysis, considering the shape and dispersion of directions distributions as a function of latitude. The PSV estimates evaluated are the equal-area coordinates of paleodirectional distributions rotated to the origin along two axes, x_E (east-west) and x_N (north-south) and their respective standard deviations σ_E and σ_N. The mean values and standard deviations of x_E and x_N from a distribution N data are calculated as follows:

$$\left\langle x_{E_i} \right\rangle = \frac{\sum_{i=1}^{N} x_{E_i}}{N}; \qquad \left\langle \sigma_{E_i} \right\rangle = \sqrt{\frac{\sum_{i=1}^{N} (x_{E_i} - \left\langle x_{E_i} \right\rangle)^2}{N-1}} \tag{2.18}$$

$$\left\langle x_{N_i} \right\rangle = \frac{\sum_{i=1}^{N} x_{N_i}}{N}; \qquad \left\langle \sigma_{N_i} \right\rangle = \sqrt{\frac{\sum_{i=1}^{N} (x_{N_i} - \left\langle x_{N_i} \right\rangle)^2}{N-1}}. \tag{2.19}$$

The BCE19 model follows the formulation of the TK03 model, however, the statistical parameters are determined by best-fitting of the corrected standard deviations (σ_{Ec} and σ_{Nc}) calculated from PSV10 database, and combining northern and southern paleodirectional data into 10° latitude bins. The parameter values of BCE19 model are listed in Table 2.4. As shown in Figure 2.14a, the mean values of $\bar{x_E}$ of BCE19 model (blue curve) are equal to zero for all latitudes, while the mean values of $\bar{x_N}$ (red curve) vary as a function of latitude with the highest values found between 20º and 30º latitudes. Regarding the σ_E and σ_N estimates, both vary with latitude (Figure 2.14b) with σ_N values always higher compared to σ_E. Nevertheless, the difference between the standard deviations decreases from the equator to the poles.

BB18-family Models: Bono et al. (2020) proposed two new GGP models termed BB18 and BB18.Z3. The BB18 model assumes that all non-dipole harmonic terms have zero mean, while the BB18.Z3 model has non-zero mean for the terms $\bar{g}_2^0$ and $\bar{g}_3^0$. Both models are able to reproduce the paleointensity and VGP dispersion distributions for the past 10 Myr. Moreover, BB18-family models differ from previous GGP models by incorporating a covariance pattern

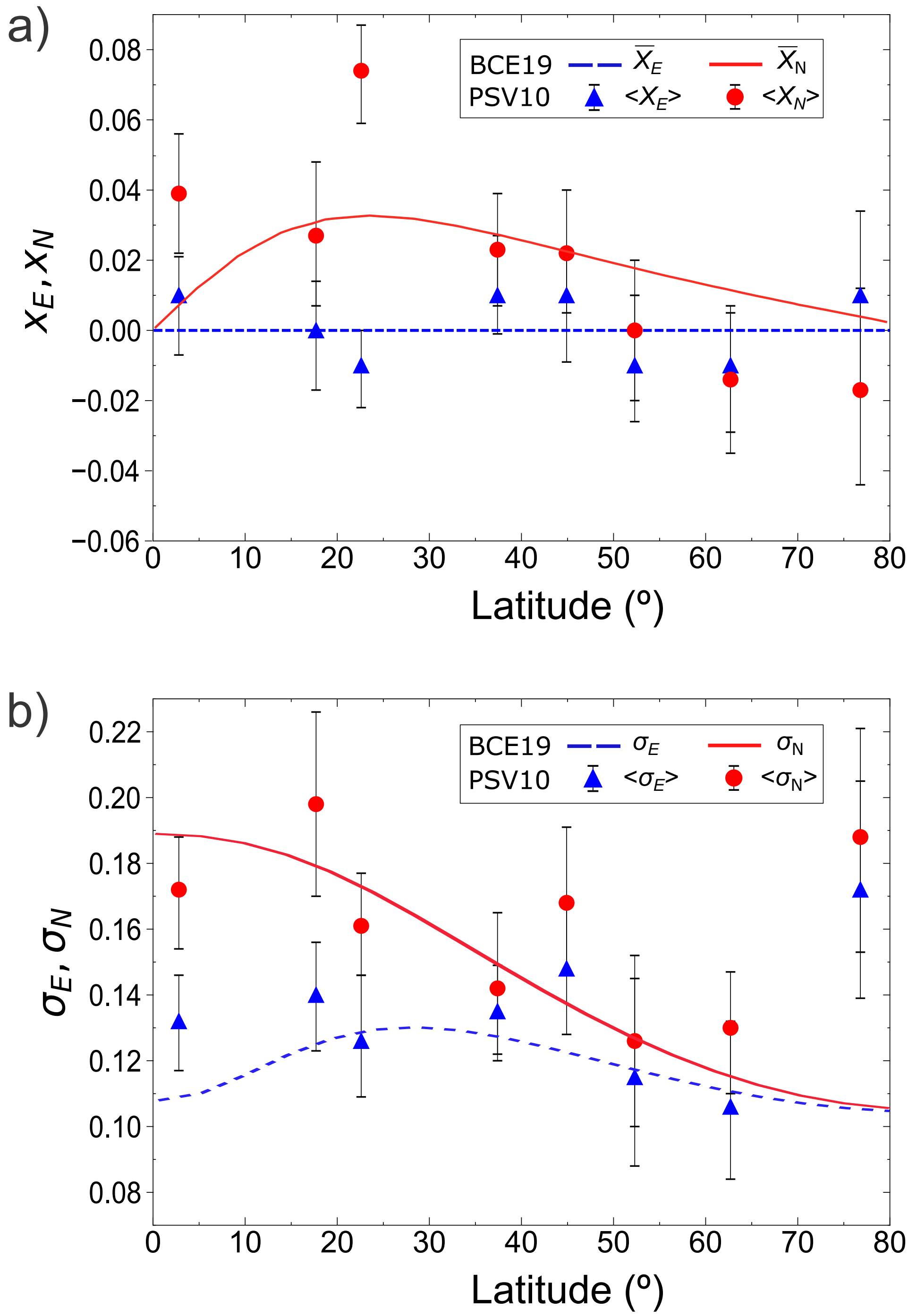

Figure 2.14 – Latitudinal distribution of directional measurements for PSV10 dataset (Cromwell et al., 2018). (a) Equal-area coordinates and (b) standard deviations along the axes north-south (east-west) are represented by red (blue) symbols. The curves are BCE19 model (Brandt et al., 2020) predictions. Modified from Brandt et al. (2020).

(cov) for a specific set of Gauss coefficients with degrees $l \leq 4$, which was deduced from 21 numerical geodynamo models. The statistical parameters (Table 2.4) were obtained as follows: (i) $\bar{g}_1^0$ was determined by the median virtual dipole moment from paleointensity database PINT (Biggin et al., 2015), (ii) the α and β parameters were determined through the best-fit of the S_B

data from the PSV10 compilation, (iii) the standard deviation of $\bar{g}_1^0$ (σ_1^0) is determined from the distribution of paleointensity measurements. For BB18.Z3 model, the zonal terms $\bar{g}_2^0$ and $\bar{g}_3^0$ were estimated using a multiobjective genetic algoritm (Deb & Kalyanmoy, 2001) to obtain the best-fit of the VGP dispersion and inclination anomaly data. The VGP dispersion curves predicted by the BB18-family models are shown in Figure 2.15. The BB18.Z3 model (pink curve) provides a slight improvement in the fit of the dispersion data filtered with Vandamme (1994) criterion compared to the BB18 model (purple curve). According to Bono et al. (2020), these small differences are associated with hemispheric asymmetries probably caused by the zonal quadrupole and octupole contributions included only in the BB18.Z3 model.

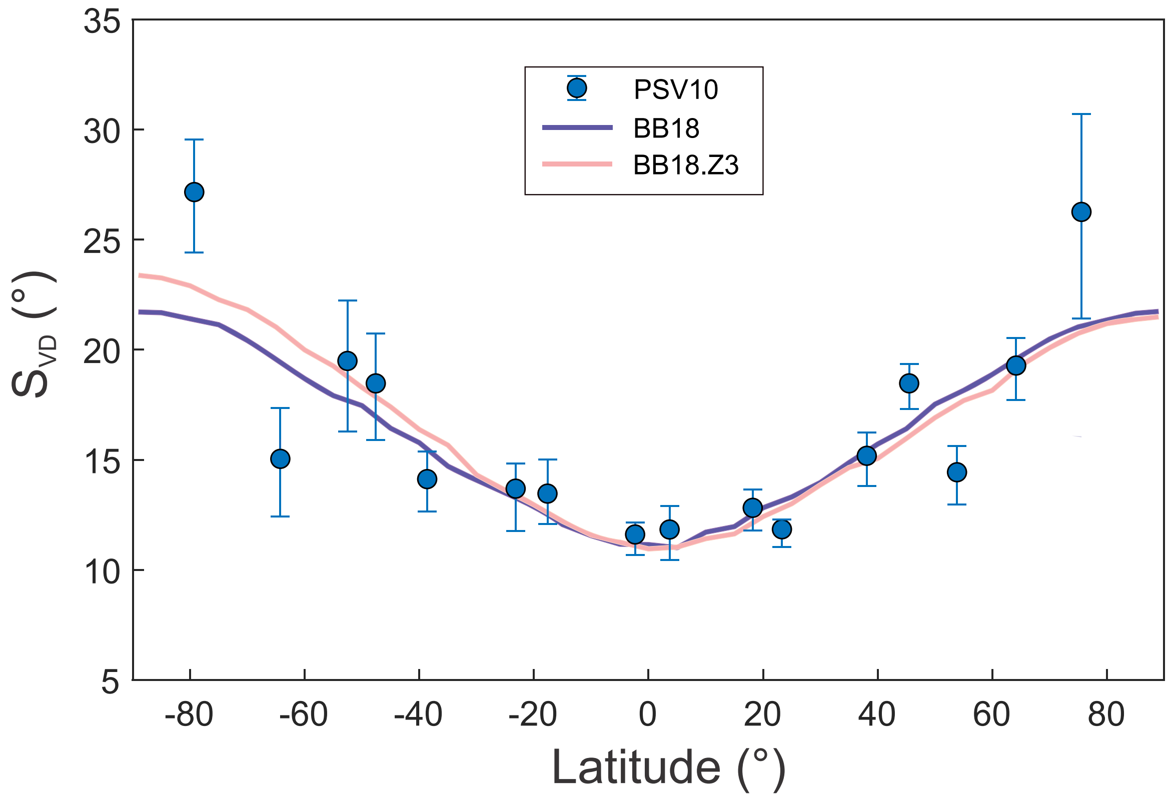

Figure 2.15 – Latitudinal variation of S_{VD} data for PSV10 dataset (Cromwell et al., 2018) are shown by blue circles. The pink and purple curves denote the BB18.Z3 and BB18 models (Bono et al., 2020) predictions, respectively. S_{VD} = VGP dispersion data filtered with Vandamme (1994) criterion. Modified from Bono et al. (2020).

2.4 The time-averaged field structure over the past 5 Myr

2.4.1 Zonal statistical models

The paleomagnetic field can be termed as *time-averaged field* when considering the average field direction of sampled sites for a given time interval (Johnson & Constable, 1996).

The GAD hypothesis has been employed as a first approximation of the time-averaged field for million years timescales. However, it is possible to investigate the non-GAD field contributions through inclination anomaly (ΔI) data distributions, expressed by (Cox, 1975):

$$\Delta I = I_{OBS} - I_{GAD}, \tag{2.20}$$

where I_{OBS} is the observed inclination that traditionally have been calculated by the Fisher mean inclination, and I_{GAD} corresponds to expected inclination for a GAD field. Cox (1975) was the first to demonstrate that ΔI estimates can be used to determine the low-degree axial non-dipole (g_2^0, g_3^0) terms with respect to the g_1^0 term. As reported by McElhinny et al. (1996), a field model can be fitted to ΔI data as a function of colatitude θ. For a purely dipole field, I_{GAD} is defined as:

$$\tan I_{GAD} = 2\cot\theta. \tag{2.21}$$

Considering only the zonal harmonics g_2^0 and g_3^0, the observed inclination model (see Appendix A.3) can be determined according to the following equation (McElhinny et al., 1996):

$$\tan I^*_{OBS} = \frac{2\cos\theta + G2\left(\frac{9}{2}\cos^2\theta - \frac{3}{2}\right) + G3\left(10\cos^3\theta - 6\cos\theta\right)}{\sin\theta + G2\left(3\cos\theta\sin\theta\right) + G3\left(\frac{15}{2}\cos^2\theta\sin\theta - \frac{3}{2}\sin\theta\right)}. \tag{2.22}$$

The zonal quadrupole ($G2 = g_2^0/g_1^0$) and octupole ($G3 = g_3^0/g_1^0$) components are obtained using a least squares method between the observed anomalies and the inclination anomaly model from Equations (2.20) to (2.22). For instance, latitudinal pattern for three inclination anomaly models is shown in Figure 2.16. In the first case, the field model depends only on the zonal quadrupole term with $G2 = 0.10$, ΔI has negative values in both hemispheres with large deviations from a GAD model ($\Delta I = 0$) at low latitudes. In the second case, the field model contains only the octupole contribution with $G3 = 0.10$, ΔI has negative (positive) values for the northern (southern) hemisphere. Note that the highest ΔI values are located at intermediate latitudes for both hemispheres. The last case consists of a field model with the combination of the terms $G2$ and $G3$ (both with the same value of 0.10), the highest ΔI values are observed in the northern hemisphere.

Through statistical analyses of ΔI data distribution over the past 5 Myr, the earlier zonal TAF models (e.g., McElhinny et al., 1996; Merrill & McElhinny, 1977; Schneider & Kent, 1990) indicated that the dominant component is the zonal quadrupole term ($G2 \sim 3\%$) with

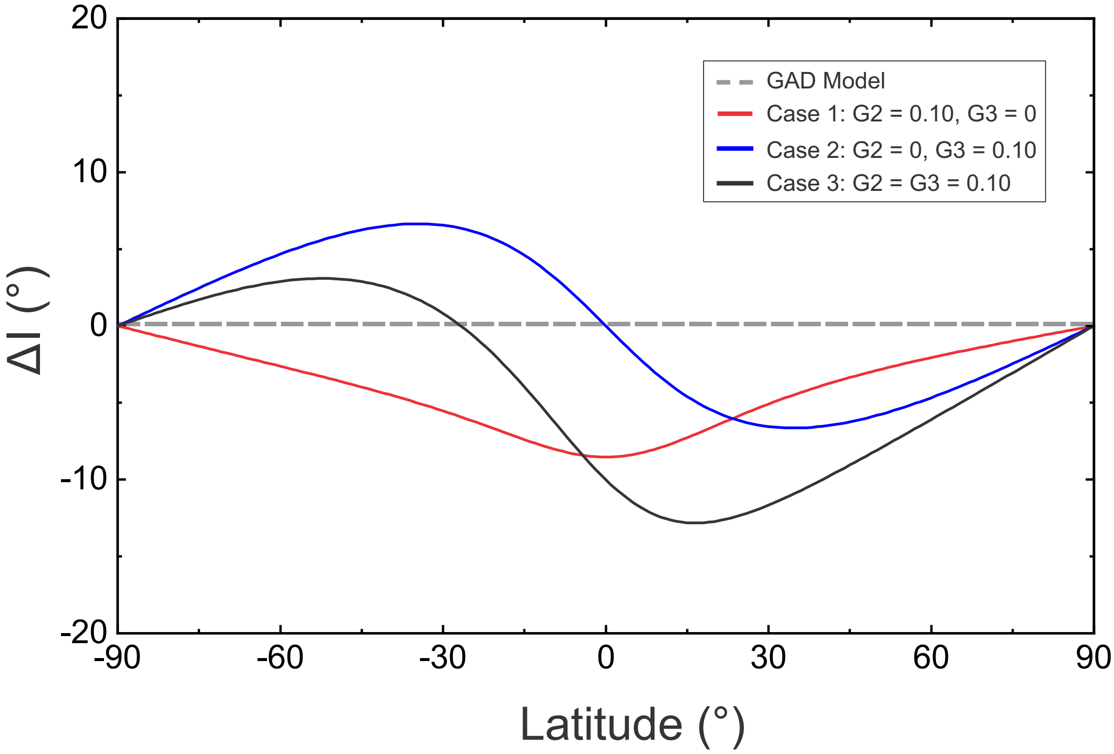

Figure 2.16 – Zonal models for the inclination anomaly (ΔI) as a function of latitude.

a small octupole contribution ($G3 \sim 1\%$). Johnson et al. (2008) proposed a 0-5 Ma TAF model using high-quality paleomagnetic data, with best estimates for $G2 = 3\%$ and $G3 = 3\%$. The authors also investigated the latitudinal structure of ΔI for the Brunhes normal and Matuyama reverse polarity chrons. Their results revealed the higher contributions of the $G2$ and $G3$ terms to the Matuyama chron compared to the Brunhes chron (Table 2.5), suggesting differences between normal and reverse polarity fields.

Table 2.5 – Values of $G2$ and $G3$ terms from time-averaged field models for the last 5 Myr. From Johnson et al. (2008).

Time interval	$G2 = g_2^0/g_1^0$	$G3 = g_3^0/g_1^0$
Brunhes (0 - 0.78 Ma)	0.02	0.01
Matuyama (0.78 - 2.58 Ma)	0.04	0.05
0 - 5 Ma	0.03	0.03

2.4.2 Non-zonal Time-averaged field models

An alternative approach to examining the spatial features (latitudinal and longitudinal variations) of the paleomagnetic field over the past few million years, is based on the spherical harmonic representation (Aubert et al., 2010). Several non-zonal TAF models (e.g., Carlut & Courtillot, 1998; Gubbins & Kelly, 1993; Hatakeyama & Kono, 2002; Johnson & Constable, 1995, 1997; Kelly & Gubbins, 1997) have been proposed for the interval 0-5 Ma, in which the Gauss coefficients are truncated at degree and order 10. In general, these models fit the paleodirectional data within a specified tolerance level through non-linear inversion techniques. Nonetheless, TAF models differ in the methodological approaches and paleomagnetic databases used (see Johnson and McFadden (2015) for details). An aspect discussed by some authors (e.g., Hulot et al., 2010; McElhinny, 2004) concerns the use of low quality and spatial distribution of paleomagnetic data in TAF models, which could produce biased results from non-zonal field structures.

Recently, Cromwell et al. (2018) suggested the first global TAF model (referred to as LN3) from the high-quality normal lava data for the 0-5 Ma period using the PSV10 database. The dominant non-dipole contribution to the LN3 model corresponds to the g_2^0 term that is 3.0% of g_1^0. This model is a direct update of the LN1 model (Johnson & Constable, 1995) with improvements in spatial data coverage. Cromwell et al. (2018) detected similarities in the ΔI structure between the LN3 and LN1 models (Figure 2.17). However, the spatial features are quite different in the South American region where the LN3 model (Figure 2.17a) exhibits negative inclination anomalies, in contrast to the large positive ΔI observed in the LN1 model (Figure 2.17b). As pointed out by Cromwell et al. (2018), these differences result from a better distribution of paleomagnetic data over Americas using the PSV10 compilation compared to the previous databases. Therefore, improvements in the geographic and temporal coverage of paleomagnetic data are fundamental for a better assessment of TAF structure for the past few million years.

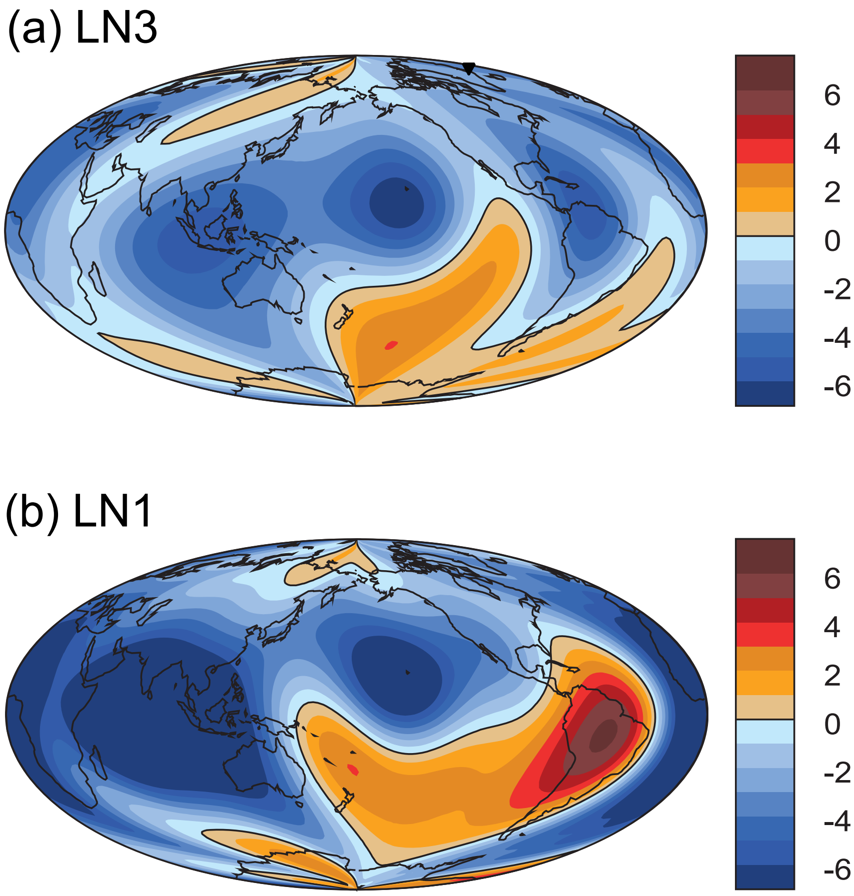

Figure 2.17 – Spatial variations of the inclination anomaly (in degrees) on the Earth's surface for the TAF models (a) LN3 and (b) LN1. Modified from Cromwell et al. (2018).

3. GEOMAGNETIC FIELD FOR 0-10 Ma: NEW INVESTIGATIONS

This chapter presents a scientific paper published in *Geochemistry, Geophysics, Geosystems*. The supplementary material is available in the online version of the article below and at the Earth Reference Digital Archive (http://earthref.org/ERDA/2476/).

de Oliveira, W. P., Hartmann, G. A., Terra-Nova, F., Brandt, D., Biggin, A. J., Engbers, Y. A., Bono, R. K., Savian, J. F., Franco, D. R., Trindade, R. I. F., & Moncinhatto, T. R. (2021). Paleosecular Variation and the Time-Averaged Geomagnetic Field Since 10 Ma. *Geochemistry, Geophysics, Geosystems*, *22*(10). https://doi.org/10.1029/2021GC010063

3.1 Paleosecular variation and the time-averaged geomagnetic field since 10 Ma

Abstract

Investigations into long-term geomagnetic variations provide useful information regarding paleomagnetic field behavior. In this study, we assess the latitudinal structure of paleosecular variation (PSV) and the time-averaged field (TAF) for the Brunhes normal and Matuyama reverse chrons, and for the 0-10 Ma period, from an updated and reviewed paleodirectional database spanning the past 10 Myr. The new database comprises 2543 paleomagnetic sites from igneous rocks, providing improvements in the geographic and temporal distributions of the high-quality data relative to previous compilations. In addition, the new data collection differs considerably in application of strict selection criteria. Statistical analysis of the virtual geomagnetic pole (VGP) dispersion curve of Model G reveals a low latitudinal dependence of PSV for the last 10 Myr. For this period, we present a zonal TAF model based on the latitudinal distribution of inclination anomaly data. The best estimates found for axial quadrupole and octupole components were about 3% and 1% relative to axial dipole component, respectively. The new statistical models for the Brunhes and Matuyama chrons have different patterns in both PSV and TAF, in compliance with earlier studies. Our quantitative assessments indicate an apparent hemispheric PSV asymmetry, particularly in the Brunhes chron, with a stronger latitudinal signature in the southern hemisphere compared to the north. These findings suggest that equatorial PSV asymmetry, that has previously been found in modern, historical and millennial scale geomagnetic models, has persisted over the

past 0.78 Ma.

Keywords: Paleosecular Variation, Time-Averaged Field, Equatorial PSV Asymmetry.

3.1.1 Introduction

Spatial and temporal geomagnetic field variations have been observed over different geological timescales. Ancient field measurements, mainly obtained from geological materials (sedimentary and igneous rocks), allow investigations of directional and intensity variability of the paleomagnetic field that result from processes operating in Earth's fluid core (see, e.g., Hulot et al., 2010). Particularly, information about paleosecular variation (PSV), long-term variations of the order of 10^5-10^6 years (e.g., Johnson & McFadden, 2015), is essential to better understand temporal geomagnetic field evolution and to constrain numerical geodynamo models (Biggin et al., 2020; Coe & Glatzmaier, 2006; Davies et al., 2008; Meduri et al., 2021; Sprain et al., 2019). On these long timescales, a basic assumption of paleomagnetism concerns the time-averaged field (TAF) structure, which can be described approximately by a geocentric axial dipole (GAD) where the dipole aligns with Earth's spin axis (Merrill & McFadden, 2003).

PSV and TAF studies have focused on the 0-5 Ma interval because of the large availability of paleodirectional data relative to earlier epochs, and due to the reduced effects of plate tectonic motion. Various global paleomagnetic databases for lava flows and thin dykes data (e.g., Johnson et al., 2008; Lee, 1983; McElhinny & Merrill, 1975; McElhinny & McFadden, 1997) have been developed to construct PSV and TAF models. The main differences among 0-5 Ma databases relate to the selection criteria adopted (see Johnson and McFadden (2015) for a detailed review). Additionally, data collections are affected by poor spatial and temporal coverage and low-quality data. As addressed by some authors (e.g., Johnson et al., 2008; McElhinny & McFadden, 1997), these factors can influence PSV and TAF modeling, and make it difficult to understand paleofield behavior. Over the past two decades, significant progress has been achieved in obtaining high-quality data for the last 10 Myr (Cromwell et al., 2018; Johnson et al., 2008; Opdyke et al., 2015). These studies imposed rigorous selection criteria for obtaining acceptable data, requiring improved statistical parameters and determined from modern laboratory methods. In essence, these high-quality data compilations provide support for statistical investigations of non-GAD field contributions, detection of distinctions between normal and reverse polarity fields, and evaluation of possible hemispheric asymmetries in PSV and TAF estimates.

PSV is usually assessed by the angular dispersion of virtual geomagnetic poles (VGPs) assuming a GAD field (Merrill & McFadden, 2003). The latitudinal variation in VGP dispersion has been described by two main types of statistical PSV models: Model G (McFadden et al., 1988) and Giant Gaussian Process (GGP) models (Constable & Parker, 1988). These models were designed based on observable modern geomagnetic field properties, but use different statistical approaches. Both models consider the surface magnetic field in spherical harmonic form, where Gauss coefficients g_l^m and h_l^m (l is the degree and m is the order) define the field geometry. In the phenomenological Model G of McFadden et al. (1988), the overall VGP angular dispersion (S) is composed of two independent dynamo families, known as primary (or antisymmetric) and secondary (or symmetric) families, expressed by:

$$S(\lambda) = \sqrt{S_s^2 + S_p^2}. \tag{3.1}$$

The contribution relative to the primary family (S_p) comprises spherical harmonic terms with odd-numbered $l-m$ (i.e., equatorially antisymmetric terms), which was assumed to vary linearly with latitude (λ). The secondary family (S_s) that contributes to the VGP dispersion is given by the equatorially symmetric terms for which $l - m$ is even and is assumed to be approximately constant for all latitudes. In this respect, Model G can be described by a latitudinal variation curve fitted to the dispersion data, considering two shape parameters a (= S_s) and b (= S_p/λ), respectively, which are related to the secondary and primary families (McElhinny & McFadden, 2000).

GGP-type models offer a different statistical perspective capable of predicting the distribution of geomagnetic field vectors in any geographical location, by describing the variances of Gauss coefficients. Initially defined by Constable and Parker (1988) who considered each Gauss coefficient as a normally distributed random variable, and the prescribed variances that reproduce the spatial power spectrum (Lowes, 1974) of the modern field. All non-dipole spherical harmonic terms have zero mean except for the axial quadrupole component. Prior to 2020, four GGP models: CP88 (Constable & Parker, 1988), QC96 (Quidelleur & Courtillot, 1996), CJ98 (Constable & Johnson, 1999), and TK03 (Tauxe & Kent, 2004) were presented, and are differentiated by the analytical methods and paleomagnetic 0-5 Ma database used (see Johnson & McFadden, 2015). Recently, the GGP models of BCE19

(Brandt et al., 2020), BB18 and BB18.Z3 (Bono et al., 2020) have been used to evaluate the latitudinal behavior of PSV spanning the last 10 Myr using the 0-10 Ma database (hereafter PSV10) of Cromwell et al. (2018). The BCE19 model was constructed from analysis of paleodirectional data, taking into account the shape and dispersion of directional distributions at any latitude. It assumes that only the axial dipole term $\bar{g}_1^0$ has a non-null mean value, and the variances ($\sigma_l^{m^2}$) of any Gaussian coefficients depend on the degree l and m, and the parameters α and β, respectively, which are associated with the secondary and primary family coefficients (following the formulation of the TK03 model). The BB18-family models introduce a covariance between the Gauss coefficients for a specific set of terms with degrees $l \leq 4$ deduced from numerical geodynamo simulations. The BB18 model considers only a mean $\bar{g}_1^0$ term, while the BB18.Z3 model includes the axial quadrupolar $\bar{g}_2^0$ and octupolar $\bar{g}_3^0$ terms. In addition, BB18 models improve the fit to the latitudinal dependence of VGP dispersion estimates and the paleointensity records for the last 10 Myr.

Regarding the TAF geometry, the presence of non-GAD components over the past few million years has been debated (Aubert et al., 2010). Through analyses of the latitudinal distribution of inclination anomaly (ΔI) data, zonal TAF models for the 0-5 Ma period (McElhinny et al., 1996; Merrill et al., 1990; Merrill & McElhinny, 1977) indicate that the prominent component is the axial quadrupole term ($g_2^0 \sim 4\%$ of g_1^0), with a small octupole contribution ($g_3^0 \sim 1\%$ of g_1^0). In addition, higher PSV estimates and larger non-dipole contributions were reported for reverse polarity periods compared to normal polarity periods (Johnson et al., 2008; McElhinny & McFadden, 1997).

A further debate concerns potential hemispheric paleomagnetic field asymmetries (Cromwell et al., 2013a; Engbers et al., 2020). In particular, the latitudinal PSV structure for the past few million years suggests higher southern hemisphere VGP dispersion than northern hemisphere (Cromwell et al., 2018; Cromwell et al., 2013a; Lawrence et al., 2009). Predictions from numerical geodynamo simulations indicate that lateral thermal variations at the core-mantle boundary (CMB) could influence geomagnetic field morphology and promote asymmetries (Aubert et al., 2013; Davies et al., 2008; Terra-Nova et al., 2019). However, our knowledge of long-lived PSV and TAF asymmetries is limited by the uneven temporal and geographic sampling of paleomagnetic records. In this context, improvements and expansion to the current 0-10 Ma database are important to better assess the TAF structure, and to constrain Earth-like geodynamo models.

Here we review and update the paleodirectional database derived from igneous rocks for the past 10 Myr using stringent selection criteria compared to the previous compilations. We then evaluate the latitudinal PSV and TAF structure for three age intervals corresponding to the Brunhes and Matuyama chrons, and the 0-10 Ma period. VGP dispersion estimates from Model G are compared with recent PSV studies and with the BCE19 and BB18 model family. We also quantitatively assess VGP dispersion patterns for the northern and southern hemispheres and extend investigations for the historical period from the COV-OBS geomagnetic field model (Gillet et al., 2015). We present new zonal TAF models for each age interval based on robust inclination anomaly estimates, and discuss the presence of non-dipole components relative to the GAD term.

3.1.2 Paleomagnetic Database

In order to investigate PSV behavior and TAF structure in the 0-10 Ma interval, we compiled an updated database of high-quality paleodirections from published studies. They include: the Magnetics Information Consortium (MagIC) database (https://www2.earthref.org/MagIC; Tauxe et al., 2016), academic search engines (e.g., Scopus at https://www.scopus.com/home.uri), and the PSV10 compilation (Cromwell et al., 2018). Only paleomagnetic data derived from volcanic rocks and thin dykes were accepted because these are considered most suitable for PSV and TAF analysis because they provide instantaneous paleomagnetic field records in contrast to smoothed sedimentary records (Johnson & McFadden, 2015). We further employ the following selection criteria.

1. All paleomagnetic data must be within the age interval 0-10 Ma.

2. The characteristic remanent magnetization (ChRM) directions must have been acquired using modern demagnetization procedures and processing techniques. Additionally, site-level data must have an associated demagnetization code (the number of demagnetization site used for ChRM determination) equal to four or five (DC $\geq$ 4; McElhinny & McFadden, 2000).

3. Studies that did not provide site-mean directions and site coordinates were rejected.

4. Studies where the sampling region has been subjected to significant post-emplacement tectonism (e.g., tilting) were not included, based on information provided in the original publications.

5. All studies must comprise paleodirectional data from at least ten sites (i.e., $N \geq 10$) related to independent geomagnetic field records, for a given study location.

6. We require a minimum of five samples per site ($n \geq 5$), with an estimated Fisher precision parameter (Fisher, 1953) of $k \geq 50$ for each site-mean direction.

Detailed discussion of these six selection criteria can be found in Text S1 in Supporting Information S1.

The paleomagnetic database contains 2543 directional sites from 80 paleomagnetic studies published between 1989 and 2020 that meet our selection criteria. Selected data sets associated with their respective geographic locations, average ages, DC values, and references are listed in Table S1 (see Table D.1 in Appendix D). Moreover, our compilation supplies additional information for all site-level data (summarized in Table S2), including site coordinates, paleolocations (computed using the NNR-MORVEL 56 model (Argus et al., 2011) for plate motion corrections), Fisher site-mean directions, paleomagnetic statistical parameters, ages, and VGP coordinates. We consider here site locations corrected for plate tectonic motions in the PSV and TAF statistical analyses (as adopted by Cromwell et al. (2018)), as discussed below.

Regarding the number of paleomagnetic sites and quality criteria, the new database supersedes the PSV10 data set (as discussed in section 3.1.5.1), and offers a latitudinal coverage from 78°S to 78°N (Figure 3.1). There is an uneven spatial distribution of paleodirectional data between the northern and southern hemispheres; the latter consists of 23 data sets which corresponds to 29% of the collection.

Most of paleodirectional data are associated with high-level demagnetization procedures (DC = 5; 72% of the paleomagnetic sites; Table S2, Figure S1). The number of samples per site are mainly within the 5-10 range (~89% of paleodirectional sites), whereas the Fisher precision parameter, k is concentrated between 50 and 200. Only 844 paleodirectional sites (~33%) are associated with radiometric dating based on information from the original references. For other sites, average ages were inferred from stratigraphic and historic records discussed in selected studies. Paleomagnetic sites for last 10 Myr are mainly from the Brunhes (39%) and Matuyama (29%) chrons.

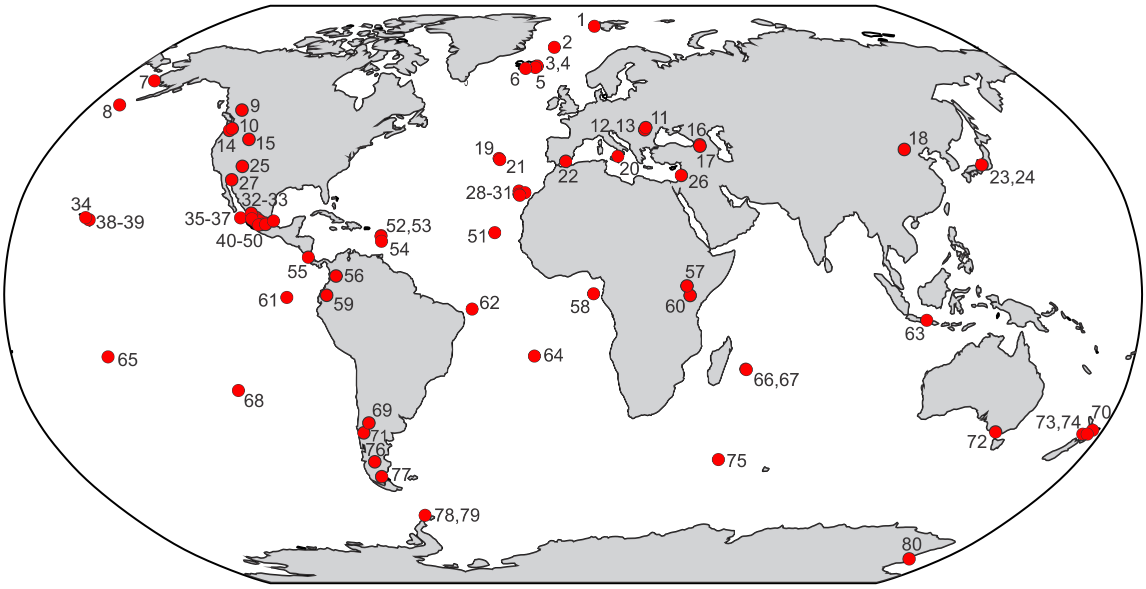

Figure 3.1 – Global distribution of selected paleodirectional data over the past 10 Myr. Numbers represent identification numbers reported in Table S1.

3.1.3 Methods

We examined the statistical behavior of the paleofield during three time periods similar to Johnson et al. (2008) (hereafter J08): (1) the entire 0-10 Ma data sets, (2) Matuyama (0.78-2.58 Ma) reverse polarity data, and (3) Brunhes (0-0.78 Ma) normal polarity data. We aim to ascertain whether there are differences between normal and reverse polarity intervals. Data sets assigned to the Gauss and Gilbert chrons were not assessed due to insufficient data to perform a separate analysis for these time intervals.

3.1.3.1 Estimate of paleosecular variation

To assess PSV behavior, the between-site dispersion (S_B) for each data set was calculated according to (McElhinny & McFadden, 1997):

$$S_B = \sqrt{S^2 - \frac{S_w^2}{\bar{n}}}, \tag{3.2}$$

First, it is necessary to calculate the total angular VGP dispersion (S) given by (Cox, 1970):

$$S = \sqrt{\frac{1}{N-1}\sum_{i=1}^{N}\Delta_i^2}, \tag{3.3}$$

where N is the number of sites and Δ_i corresponds to the angular deviation between the ith VGP and the mean VGP. All VGP data associated with reverse polarity directions were converted to normal poles before calculating S values. In equation (3.2), the correction factor $(S_w^2/\bar{n})$ is used to remove random errors associated with the within-site dispersion, calculated from Equation (2.14).

To investigate the latitudinal variation of S_B data, we used Model G (McFadden et al., 1988), which describes the latitudinal dependence of VGP dispersion curves by:

$$S_B(\lambda) = \sqrt{a^2 + (b\lambda)^2}. \tag{3.4}$$

where a and b are empirical constants related to the symmetric ($S_s = a$) and antisymmetric ($S_p = b\lambda$) geodynamo families, respectively. Shape parameters a and b values were estimated by fitting to S_B data using a Python-based algorithm (defined with the *scipy.optimize.leastsq* package) that employs the Levenberg-Marquardt method, which is suitable for solving nonlinear least squares regressions (Aster et al., 2012), and has been used in two recent PSV studies (de Oliveira et al., 2018; Franco et al., 2019).

3.1.3.2 Estimate of the time-averaged paleomagnetic field

For analysis of the latitudinal structure of the 0-10 Ma TAF, we calculate the inclination anomaly (ΔI) that is the difference between observed inclination (I_{OBS}) and the inclination expected for a GAD field according to the Equation (2.20).

Before calculating ΔI, reverse polarity site-mean directions were converted to antipodal directions. Thus, ΔI values for each data set were estimated by the difference between the mean inclination (R. A. Fisher, 1953) and the GAD inclination (I_{GAD}), calculated from the site mean latitude λ:

$$I_{GAD} = \tan^{-1}(2\tan\lambda). \tag{3.5}$$

The distribution of ΔI anomalies allows estimation of the zonal quadrupole (g_2^0) and octupole (g_3^0) contributions relative to the axial dipole term (g_1^0) from the predicted field model for observed inclination (I^*_{OBS}) as a function of colatitude θ (90° - latitude), using Equation (2.22).

We determined the zonal quadrupole ($G2 = g_2^0/g_1^0$) and octupole terms ($G3 = g_3^0/g_1^0$) by weighted least squares fittings between the observed ΔI anomalies and the predicted inclination anomaly (from Equations 2.20, 3.5 and 2.22), where the weighting factors correspond to 95% uncertainties in the observed ΔI data. The best-fit TAF model was obtained based on the Levenberg–Marquardt method (see section 3.1.3.1).

3.1.3.3 Transitional VGPs

Anomalous VGP data (characterized by large deviations from the mean pole) are generally excluded in PSV and TAF studies to ensure that data reflect stable field regimes. These anomalous VGPs (also referred to as outliers; Biggin et al. (2008b)) can be associated with geomagnetic excursions, polarity transitions, or spurious data caused by experimental measurement errors or secondary magnetizations (Johnson & McFadden, 2015). To evaluate the effects of transitional data on PSV and TAF estimates, we calculate the dispersion S_B and ΔI after applying three approaches for each time period. The first applied no VGP cutoff and considered all directional data. The second used a fixed 45° cutoff angle, removing paleodirectional sites with VGPs that deviate $> 45°$ from the mean paleomagnetic pole. The third used the criterion of Vandamme (1994), where the cutoff angle (A) relative to mean pole is calculated as a function of dispersion S, by:

$$A(^\circ) = 1.8S(^\circ) + 5(^\circ) \tag{3.6}$$

An iterative method is employed according to the A value for a given data set; if VGP data are larger than the A estimate, they are excluded, S is recalculated, and the procedure is repeated until there are no larger deviations than the value determined from Equation (3.6).

Approximately 3% of paleodirectional sites from the entire 0-10 Ma data set are regarded as anomalous or transitional after applying a fixed 45° cutoff; this increased to 5% for the Vandamme (1994) criterion. The statistical distribution of paleomagnetic sites retained after applying a VGP cutoff for the three time periods is shown in Figure S2.

3.1.4 Results

3.1.4.1 Analysis of latitudinal variation of VGP dispersion

S_B estimates for three temporal subsets: 0-10 Ma, Matuyama, and Brunhes age intervals are presented in Tables S3, S4 and S5, respectively. Tables S3-S5 also include, for each age group, S_B results with lower and upper 95% confidence limits determined by the bootstrap method (Efron & Tibshirani, 1993), alongside values of average site latitude and longitude, mean direction, corresponding paleomagnetic pole, and paleomagnetic statistical parameters. Some data sets have substantially higher or lower S_B estimates, so we apply an additional criterion proposed by Deenen et al. (2011) to assess whether the data adequately sample PSV, which is defined by an envelope A_{95} limited by a range of values between A_{95min} and A_{95max} (see Supporting Information, Section S2). This criterion was used to identify data with extremely different behaviors from that generally observed in paleomagnetic studies; these data were not considered in our PSV and TAF analyses. Furthermore, this criterion was used here because it was designed for datasets and models from targets with ages of a few million years and with thermoremanence acquisition similar to those found here, i.e., data derived from rapidly cooling igneous rocks. In the 0-10 Ma period, we identify a maximum of eleven data sets that do not meet the criterion of Deenen et al. (2011)(see Table S3). These possible PSV estimate biases may be related to transitional data that are over-represented in some data sets, especially when no VGP cutoff or a variable cutoff is employed (data sets # 5, 12, 22, 31, 76, and 80). In addition, data that are serially correlated or that are temporally underrepresented may contribute to anomalously low S_B values in three paleomagnetic studies (data sets # 32, 39, and 48). Another relevant factor might be undetected regional tectonic effects that can enhance S_B estimates.

For analysis of latitudinal variation of VGP dispersion, following the assumption of Model G that PSV is hemispherically symmetric, S_B values for northern and southern hemispheres (represented by closed and open symbols, respectively, in Figures 3.2b-d to 3.4b-d) are plotted on the same axis as a function of absolute latitude value. Curves for Model G are first presented for the 0-10 Ma data (Figure 3.2), and then for the Matuyama and Brunhes subsets separately (Figures 3.3 and 3.4, respectively). Shape parameters *a* and *b* estimates and their 95% confidence limits for the three time periods are summarized in Table 3.1. Furthermore, the S_B data distribution is compared with three recent GGP models: BCE19, BB18, and BB18.Z3. The method employed for predicted dispersions is described in Text S3 in Supporting Information.

Table 3.1 – Estimates of *a* and *b* parameters for Model G and estimates of the zonal quadrupole ($G2$) and octupole ($G3$) terms from this study.

PSV and TAF estimates	N_{fd}	$a_l^u(^\circ)$	b_l^u	$G2_l^u$	$G3_l^u$
0-10 Ma					
S_B and ΔI, no cutoff	69	$14.8_{13.1}^{16.6}$	$0.20_{0.12}^{0.28}$	$0.037_{0.016}^{0.058}$	$0.015_{-0.005}^{0.034}$
S_B and ΔI, 45° cutoff	75	$13.2_{11.8}^{14.5}$	$0.23_{0.18}^{0.28}$	$0.035_{0.015}^{0.054}$	$0.018_{0.001}^{0.036}$
S_B and ΔI, Vandamme cutoff	70	$12.4_{10.9}^{13.7}$	$0.23_{0.18}^{0.27}$	$0.032_{0.004}^{0.050}$	$0.012_{-0.004}^{0.028}$
Matuyama					
S_B and ΔI, no cutoff	13	$15.3_{12.6}^{18.1}$	$0.22_{0.13}^{0.32}$	$0.031_{-0.033}^{0.095}$	$0.020_{-0.038}^{0.079}$
S_B and ΔI, 45° cutoff	18	$14.7_{11.5}^{17.8}$	$0.22_{0.13}^{0.30}$	$0.019_{-0.043}^{0.080}$	$0.027_{-0.027}^{0.081}$
S_B and ΔI, Vandamme cutoff	16	$12.1_{8.7}^{15.6}$	$0.24_{0.16}^{0.31}$	$0.036_{-0.019}^{0.091}$	$0.029_{-0.018}^{0.077}$
Brunhes					
S_B and ΔI, no cutoff	42	$13.3_{11.1}^{15.4}$	$0.18_{0.08}^{0.28}$	$0.029_{0.003}^{0.054}$	$0.017_{-0.004}^{0.039}$
S_B and ΔI, 45° cutoff	43	$12.4_{10.8}^{14.0}$	$0.20_{0.14}^{0.26}$	$0.031_{0.005}^{0.056}$	$0.018_{-0.004}^{0.040}$
S_B and ΔI, Vandamme cutoff	41	$11.2_{9.5}^{13.0}$	$0.24_{0.18}^{0.29}$	$0.020_{-0.005}^{0.045}$	$0.013_{-0.008}^{0.035}$

Note. N_{fd} is the number of fitted data to the PSV and TAF models that meet the criterion of Deenen et al. (2011) (see Tables S3–S5). ^{u}Upper 95% confidence limit. $_l$Lower 95% confidence limit.

S_B estimates for the 0-10 Ma interval (80 data sets, Table S3), defined using three VGP cutoff approaches, are displayed in an interhemispheric representation in Figure 3.2a. Overall, an increasing dispersion S_B trend can be observed as a function of latitude for both hemispheres. Differences in PSV estimates are identified when the fixed (45°) cutoff and Vandamme (1994) criterion exclude transitional data. Model G fits most S_B data reasonably well, regardless of the VGP cutoff employed (Figure 3.2b-d). S_B data with no VGP cutoff (69 data sets, Figure 3.2b) produces a best-fit Model G curve with parameters $a = 14.8_{13.1}^{16.6^\circ}$ and $b = 0.20_{0.12}^{0.28}$. Using the 45° cutoff angle (75 data sets, Figure 3.2c) yields a slight 1.6° decrease of parameter $a = 13.2_{11.8}^{14.5^\circ}$, while parameter $b = 0.23_{0.18}^{0.28}$ is slightly higher than in Figure 3.2b. The Model G curve is also similar to the S_B data when subjected to the Vandamme (1994) cutoff (70 data sets, Figure 3.2d), and only differs in the value of $a = 12.4_{10.9}^{13.7^\circ}$, with $b = 0.23_{0.18}^{0.27}$. These two parameters are statistically compatible at the 95% confidence level in relation to the data filtered with a fixed 45° cutoff and with no cutoff. Dispersions predicted using the GGP models (Figure 3.2d) have low values compared to the Model G curve. The BB18 and BB18.Z3 models (purple and pink dash-dot lines, respectively) have lower dispersions at equatorial and high latitudes, while BCE19 (green dash-dot line) is lower at all latitudes. In addition, the BB18-family models better fit observed S_B data compared to the BCE19 model.

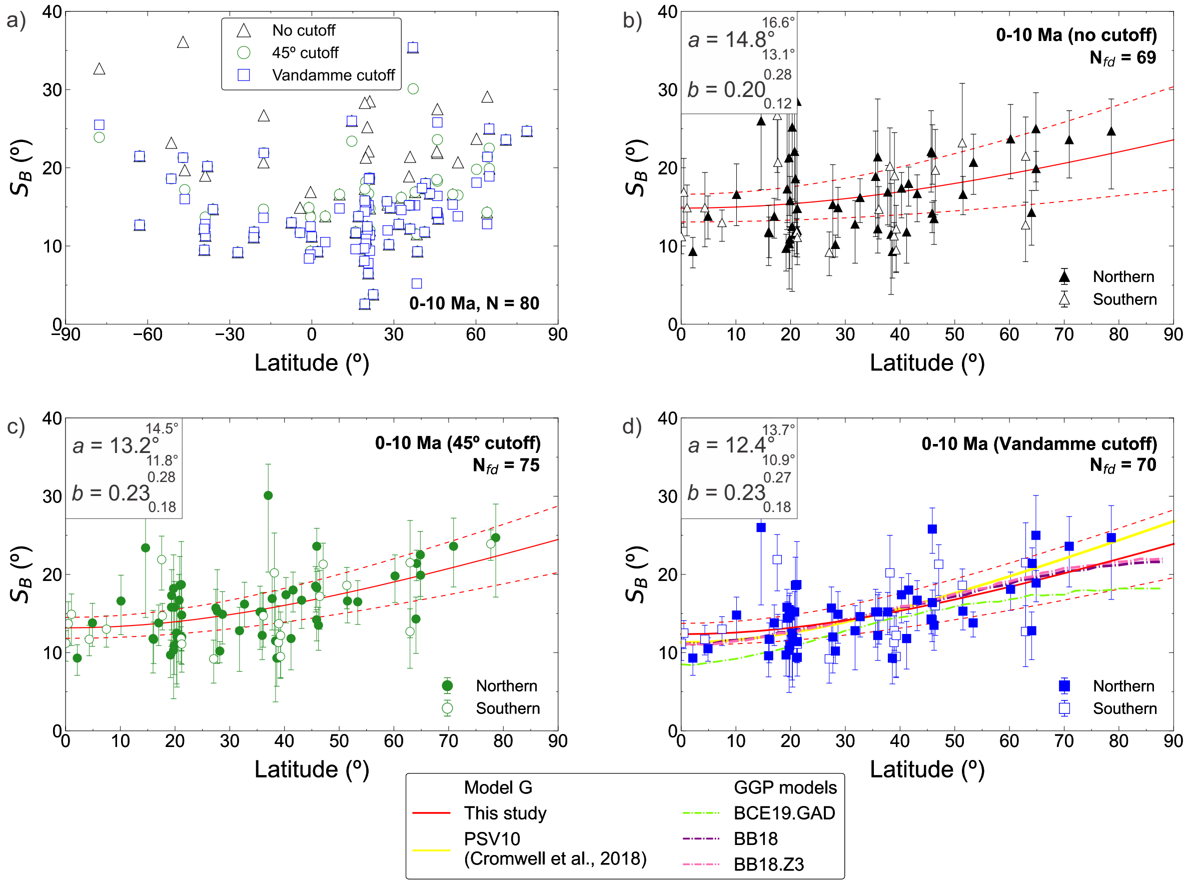

Figure 3.2 – VGP dispersion (S_B) as a function of latitude for (a) 0-10 Ma S_B results with interhemispheric coverage defined using three VGP cutoff approaches. (b-d) S_B estimates with 95% bootstrap confidence limits projected onto a single hemisphere. Closed (open) symbols correspond to data from the northern (southern) hemisphere. The best-fit Model G curves (McFadden et al., 1988) to S_B data are represented by red lines, associated with 95% confidence intervals (red dashed lines). (b) No cutoff applied, (c) 45° cutoff, and (d) Vandamme (1994) cutoff. In (d), the yellow line denotes the Model G curve fitted to the PSV10 data compilation (Cromwell et al., 2018). Also shown are VGP dispersions predicted for three GGP models: BCE19.GAD model of Brandt et al. (2020); light green dash-dot line; BB18 and BB18.Z3 models (Bono et al., 2020) purple and pink lines, respectively.

For the Matuyama reversed polarity chron (19 data sets, Table S4), a pattern of increased S_B values is observed as a function of latitude for both hemispheres (Figure 3.3a). Nevertheless, there is a data gap at low (0-25°N) and high (>65°N) northern latitudes, and data coverage is even more restricted in the southern hemisphere. When a VGP cutoff (variable or fixed) is employed, S_B estimates are especially different for data sets from Antarctica at 78°S

(Lawrence et al., 2009) and North America at latitudes 60°N (Coe et al., 2000), and 46°N (Lhuillier et al., 2017). Model G for data sets with no cutoff (13 data sets, Figure 3.3b) yields $a = 15.3_{12.6}^{18.1^\circ}$ and $b = 0.22_{0.13}^{0.32}$. Applying the fixed 45° cutoff (18 data sets, Figure 3.3c) decreases a from 15.3° to $14.7_{11.5}^{17.8^\circ}$ and $b = 0.22_{0.13}^{0.30}$, but these estimates are not statistically different considering the 95% confidence intervals. When the Vandamme (1994) criterion (16 data sets, Figure 3.3d) is used, Model G yields $a = 12.1_{8.7}^{15.6^\circ}$ and $b = 0.24_{0.16}^{0.31}$, which are similar to those with no VGP cutoff. Considering the GGP models in Figure 3.3d, predicted VGP dispersion values for BB18-family models are lower at low and high latitudes compared to the Model G fit, whereas the BCE19 model has lower dispersion along the entire latitudinal range relative to the Model G. BB18 and BB18.Z3 models fit the S_B data better as a function of latitude compared to the BCE19 model.

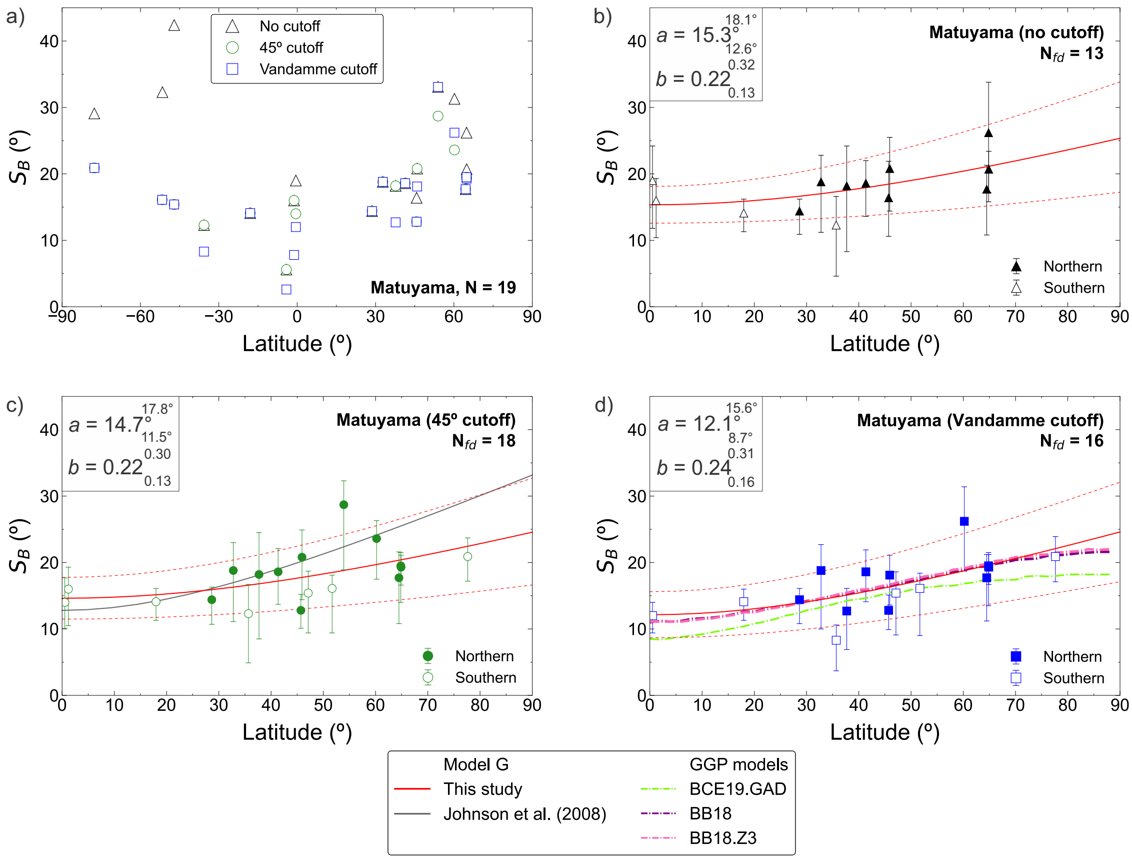

Figure 3.3 – VGP dispersion (S_B) as a function of latitude for the Matuyama reverse polarity chron. (a) S_B results with interhemispheric coverage defined using three VGP cutoff approaches. See Figure 3.2 caption for details. The gray line in (c) denotes the Model G curve fitted to the Matuyama data of Johnson et al. (2008).

The interhemispheric distribution of Brunhes normal polarity data (46 data sets, Table S5) is illustrated in Figure 3.4a. The northern hemisphere has good data coverage to

70°N, while the southern hemisphere presents a sparse data coverage, especially in mid- to high-latitudes (40°-60° S). Most studies have small differences in VGP dispersion when fixed or variable cutoffs are used. The best-fit curve for S_B estimates when no VGP cutoff is applied (42 data sets) for Model G yields $a = 13.3^{15.4^\circ}_{11.1}$ and $b = 0.18^{0.28}_{0.08}$ (Figure 3.4b). Applying a constant 45° cutoff (43 data sets, Figure 3.4c) and the Vandamme (1994) criterion (41 data sets, Figure 3.4d), estimated shape parameters are $a = 12.4^{14.0^\circ}_{10.8}$, $b = 0.20^{0.26}_{0.14}$ and $a = 11.2^{13.0^\circ}_{9.5}$, $b = 0.24^{0.29}_{0.18}$, respectively. All Model G parameters are similar regardless of cutoff employed. Regarding the GGP models, predicted dispersions for BB18 and BB18.Z3 models are compatible with the observed S_B data in a broad range of latitudes, while the BCE19 model is compatible with some data at low to mid-latitudes. When GGP models are compared to the Model G curve, the expected dispersions for BB18-family models are slightly higher for latitudes from 20° to 70°, whereas the BCE19 model provides lower dispersion estimates for all latitudes.

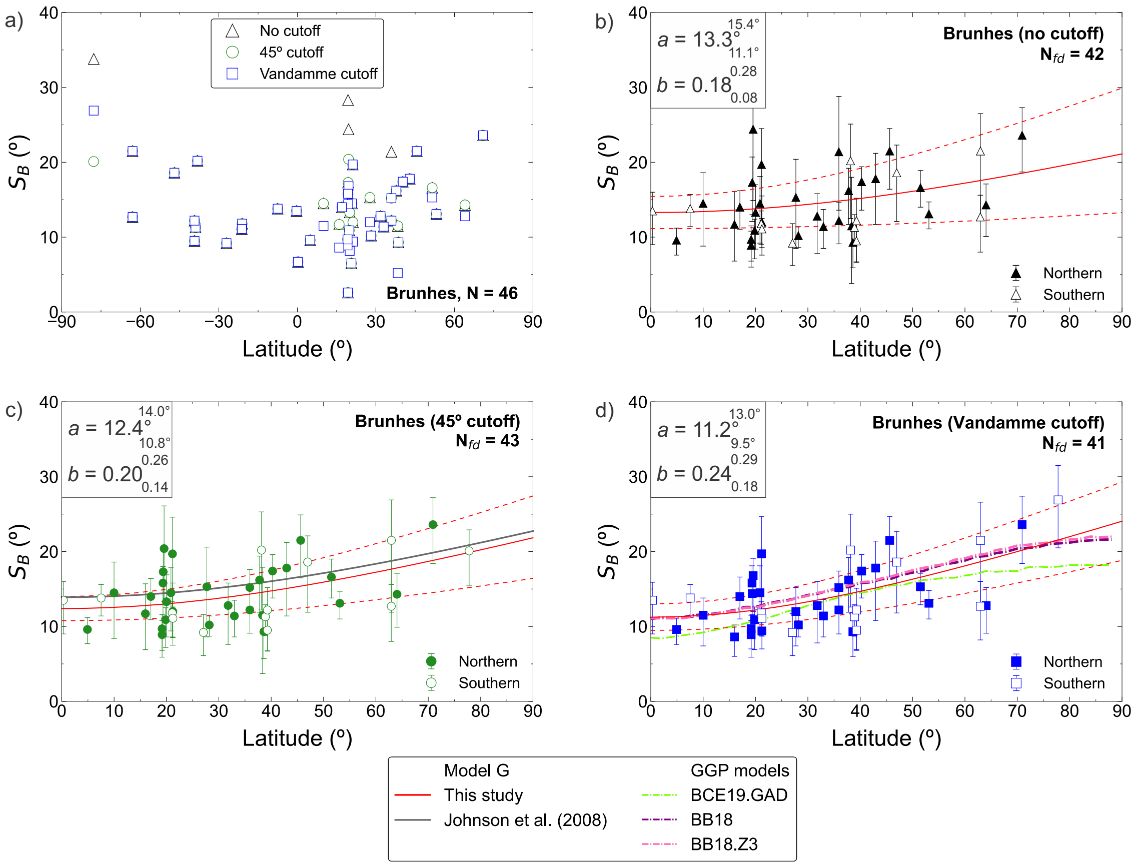

Figure 3.4 – VGP dispersion (S_B) as a function of latitude for the Brunhes normal polarity chron. (a) S_B results with interhemispheric coverage defined using three VGP cutoff approaches. See Figure 3.2 caption for details. The gray line in (c) denotes the Model G curve fitted to the Brunhes data of Johnson et al. (2008).

3.1.4.2 Analysis of latitudinal structure of inclination anomaly

In general, ΔI data for the 0-10 Ma interval (Table S3 and Figures 3.5a-c) are not statistically distinguishable from the GAD field model (dashed line) at mid- to high-latitudes for both hemispheres, which contrasts with the large negative inclination anomalies at low latitudes (0-30° N and S). The best-fit field model for 0-10 Ma data without VGP cutoff (Figure 3.5a) yields estimates of $G2 = 0.037^{0.058}_{0.016}$ and $G3 = 0.015^{0.034}_{-0.005}$. These values are statistically compatible with estimates $G2 = 0.035^{0.054}_{0.015}$ and $G3 = 0.018^{0.036}_{0.001}$ obtained with a fixed 45° cutoff (Figure 3.5b), and $G2 = 0.032^{0.050}_{0.014}$ and $G3 = 0.012^{0.028}_{-0.004}$ for subsets using the Vandamme (1994) cutoff (Figure 3.5c). Some data differ significantly from the predicted zonal field model within the 95% confidence intervals (Table 3.1), for instance, the high negative or positive ΔI values in Norway (78°; Cromwell et al., 2013a) and Saint Helena Island (Engbers et al., 2020) at 18°S, respectively.

ΔI estimates for the Matuyama chron (Table S4 and Figures 3.5d-f) are more limited, with negative and positive values in mid- to high-northern latitudes, while the southern hemisphere has positive (<10°) anomalies; exceptions are low negative ΔI values at low latitudes from Ecuador at 0.5°S (Opdyke et al., 2006) and French Polynesia at 18°S (Yamamoto et al., 2002). The distribution of ΔI estimates with no VGP cutoff (Figure 3.5d) is limited, particularly in the southern hemisphere. The best-fit field model yields values of non-dipole contributions $G2 = 0.031^{0.095}_{-0.033}$ and $G3 = 0.020^{0.079}_{-0.038}$ that are statistically compatible within 95% uncertainty limits compared to parameters obtained for the Matuyama subsets with fixed 45° cutoff ($G2 = 0.019^{0.080}_{-0.043}$ and $G3 = 0.027^{0.081}_{-0.027}$, Figure 3.5e) and Vandamme (1994) cutoff ($G2 = 0.036^{0.091}_{-0.019}$ and $G3 = 0.029^{0.077}_{-0.018}$, Figure 3.5f).

Lastly, the inclination anomaly distribution for Brunhes subsets (Table S5 and Figures 3.5g-i) has higher negative (>-5°) ΔI values at low southern and northern latitudes. The fitted field model with no VGP cutoff (Figure 3.5g) has $G2 = 0.029^{0.054}_{0.003}$ and $G3 = 0.017^{0.039}_{-0.004}$. Non-dipole zonal terms are statistically identical when transitional data are removed, with $G2 = 0.031^{0.056}_{0.005}$, $G3 = 0.018^{0.039}_{-0.004}$ and $G2 = 0.020^{0.045}_{-0.005}$, $G3 = 0.013^{0.035}_{-0.008}$ for Brunhes subsets with a fixed 45° cutoff (Figure 3.5h) and variable cutoff (Figure 3.5i), respectively.

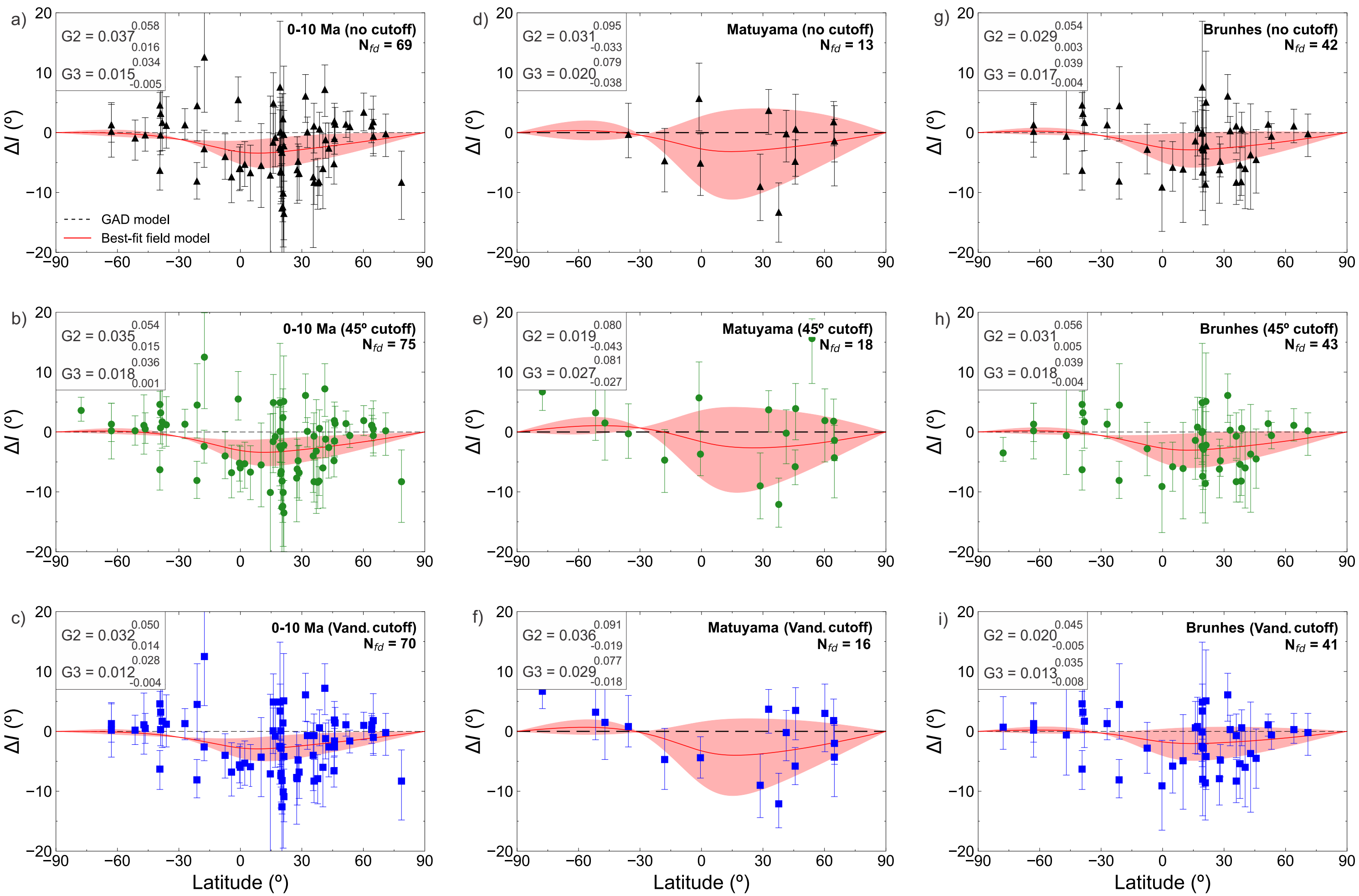

Figure 3.5 – Inclination anomaly (ΔI) as a function of latitude defined using three VGP cutoff approaches. ΔI estimates with 95% bootstrap confidence limits for (a-c) the 0-10 Ma interval, (d-f) Matuyama reverse chron, and (g-i) Brunhes normal chron. Red curves are the best-fit field model for each time period. Red-shaded areas represent the 95% confidence region associated with uncertainties for the zonal quadrupole ($G2$) and octupole ($G3$) terms. Each figure includes a GAD field model (black dashed line) at ΔI = 0. Vand. = Vandamme (1994).

3.1.5 Discussion

3.1.5.1 The New Paleomagnetic Database for 0–10 Ma

Statistical analyses of the latitudinal structure of PSV and TAF were performed for carefully selected paleomagnetic data for the 0-10 Ma period, which provides a high-quality database. About 84% of the new compilation is derived from the PSV10 database of Cromwell et al. (2018). As the primary data source, it is worth mentioning differences between the results obtained by Cromwell et al. (2018) and the present study, particularly regarding data quantity and quality, and the methods used here.

The PSV10 database consists of 2401 paleodirectional sites from 81 studies. Our data collection increases the number of sites (2543 records; Table S1), although the number of paleomagnetic studies (80) is a little lower compared to the PSV10 compilation because of the stricter criteria employed here. An improved spatial data distribution is achieved by inclusion of new records from the East Carpathians (Vişan et al., 2016), Israel (Behar et al., 2019), and Saint Helena Island (Engbers et al., 2020). In terms of temporal distribution, there was a 5% increase in data coverage for the age interval older than 5 Ma.

Moreover, our stricter selection criteria incorporate a minimum number of paleodirectional sites per study ($N \geq 10$) and number of samples per site $n \geq 5$, which differs from PSV10 database (with $n \geq 4$). These criteria exclude 15 of the original 81 data sets from the PSV10 compilation. Through inspection of the S_B distribution for individual PSV10 data sets by applying the Vandamme (1994) criterion (hereafter PSV10$_{vcut}$; Table S6), higher S_B estimates are obtained for some data than are expected from Model G, suggested by Doubrovine et al. (2019), at mid northern latitudes (Figure S3). Most of these overestimates may be associated with data undersampling, with $N < 10$, in accordance with the analyses of J08. Large N and n values are recommended to reduce bias in PSV and TAF estimates (Biggin et al., 2008b; Johnson & McFadden, 2015). Cromwell et al. (2018) demonstrated that intrasite directional variance is reduced by $\sim 7\%$ for $n = 5$ compared to $n = 4$. These assessments indicate the high-quality of data sets in the present study that can be used to examine paleofield latitudinal structure.

By comparing the Model G curve fitted to the PSV10$_{vcut}$ subset (yellow line in Figure 3.2d) and the best-fit curve for the new 0-10 Ma data sets using a variable cutoff, a lower latitudinal dependence of the VGP dispersion curve is observed here (Figure 3.2d). The estimated shape parameter $a = 12.4_{10.9}^{13.7^{\circ}}$ is not statistically distinguishable from that for the PSV10$_{vcut}$ compilation with $a = 11.3_{10.2}^{12.6^{\circ}}$, and b also overlaps the 95% confidence intervals ($b = 0.23_{0.18}^{0.27}$ for the present study and $b = 0.27_{0.19}^{0.31}$ for PSV10$_{vcut}$ subset; Table S7). The small differences in the VGP dispersion curves are probably associated with the method used to estimate PSV. We determined the VGP dispersion for each data set individually, in contrast to the mean S_B calculated for 10° latitude bands by Cromwell et al. (2018). We choose a statistical approach that allows us to investigate PSV and TAF at the study level, as has been widely employed for studies over the Phanerozoic and Archean time scales (e.g., de Oliveira et al., 2018; Doubrovine et al., 2019; Franco et al., 2019; Veikkolainen & Pesonen, 2014). In addition, it is possible to analyze differences between S_B estimates that may be caused by the paleomagnetic study location where binning is not viable.

3.1.5.2 Evidence for hemispheric asymmetry of paleosecular variation

In order to identify possible VGP dispersions pattern differences between the northern and southern hemispheres, we tested PSV equatorial symmetry by evaluating the latitudinal behavior of the Model G curves fitted to reliable S_B data for the 0-10 Ma interval (Figure 3.6a) and Brunhes chron (Figure 3.6b) for the northern and southern hemispheres (closed and open symbols, respectively). The Matuyama subset was not considered separately due to poor S_B coverage data over a broad latitudinal range. For the past 10 Myr, the overall patterns of the VGP dispersion curves for the northern and southern hemispheres are similar, regardless of the VGP cutoff filter used (see also Figures S4 and S5). The best-fit curve for S_B data using the Vandamme (1994) criterion (Figure 3.6a) resulted in Model G parameters $a = 12.4_{10.7}^{14.0^{\circ}}$ and $b = 0.23_{0.18}^{0.29}$ for the northern hemisphere, which are statistically indistinguishable at the 95% confidence level compared to the southern hemisphere ($a = 12.4_{9.7}^{15.1^{\circ}}$ and $b = 0.20_{0.09}^{0.31}$). Model G curves for S_B subsets with no VGP cutoff and a 45° cutoff are presented in Figure S4.

For the Brunhes subsets, the best-fit Model G curves suggest northern-southern hemisphere asymmetry. When the variable cutoff is employed (Figure 3.6b), Model G parameters are $a = 11.6_{9.5}^{13.6^{\circ}}$ and $b = 0.22_{0.14}^{0.30}$ for the northern hemisphere VGP dispersion curve, which are respectively higher and lower than for the southern hemisphere ($a = 10.7_{6.9}^{14.5^{\circ}}$ and $b = 0.25_{0.16}^{0.34}$). However, the differences between the Model G parameters are both within the

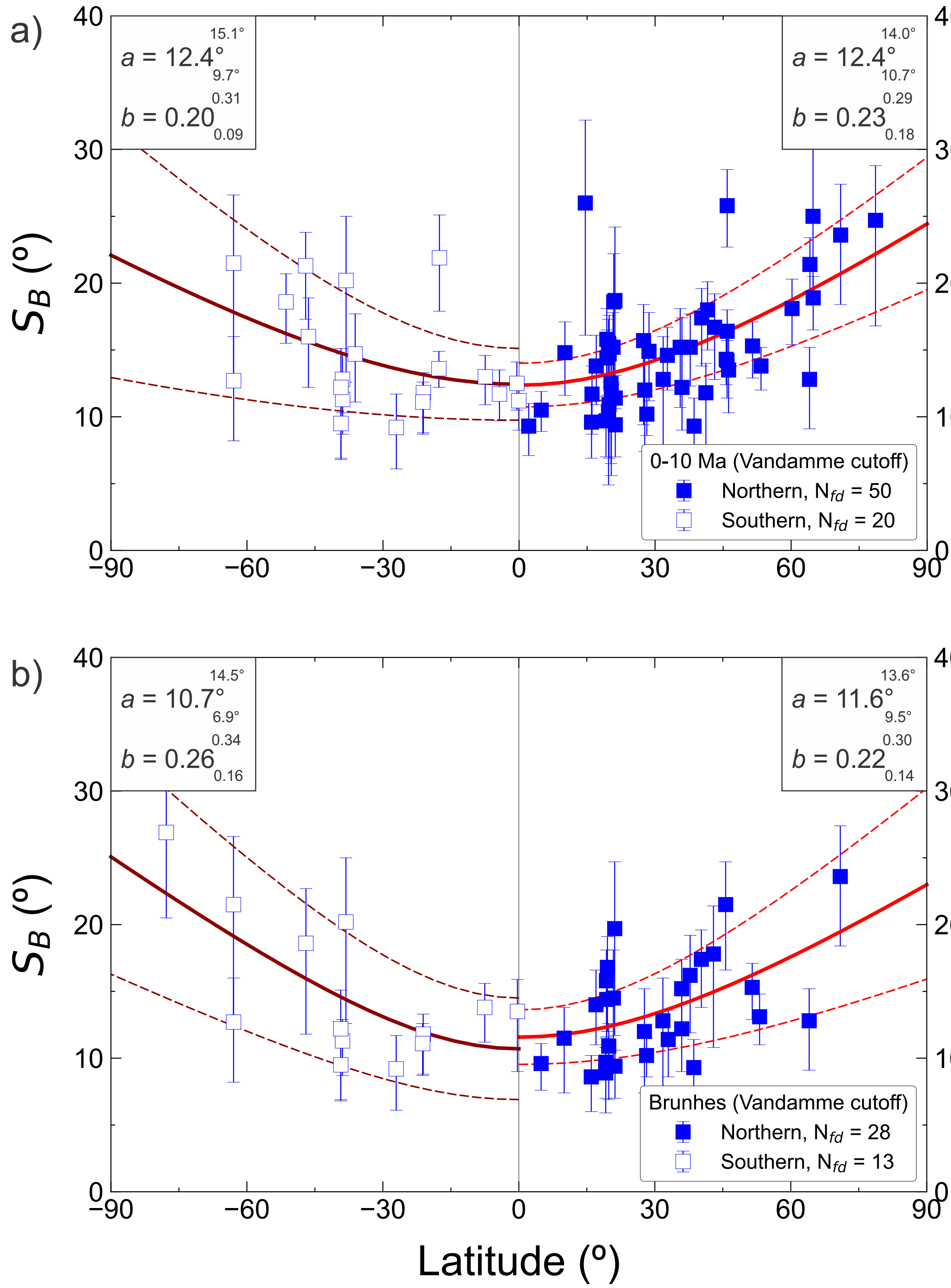

Figure 3.6 – VGP dispersion (S_B) as a function of latitude for (a) the 0-10 Ma interval, and (b) Brunhes chron applying the Vandamme (1994) cutoff. Light (dark) red lines represent the Model G curve fitted to northern (southern) hemisphere data, with its 95% confidence intervals (dashed lines).

95% confidence interval (see also Figure S5 for Brunhes subsets without a VGP cutoff and using a constant 45° cutoff).

Based on comparative assessments among VGP dispersion curves for the northern and southern hemispheres for 0-10 Ma and Brunhes data, the latter provides evidence of a hemispheric PSV asymmetry, especially when the Vandamme (1994) criterion is applied. These findings support the hypothesis of higher (lower) VGP dispersion in the southern (northern) hemispheres for at least the past 0.78 Ma. In addition, our quantitative assessment differs from previous observations (Cromwell et al., 2018; Cromwell et al., 2013a). Recent geomagnetic field models that evaluate PSV indices (P_i, a measure of regional field variability) for present, historical (Panovska & Constable, 2017), multimillennial (0-10 ka; Constable et al. (2016), and 0-100 ka (Panovska et al., 2018a; Panovska et al., 2018b)) timescales yield higher P_i values in the southern hemisphere than the northern hemisphere. These differences are associated with low field intensities, which suggest that the equatorial PSV asymmetry is a long-period feature of the geomagnetic field.

Hemispheric field structure differences have been attributed to lateral core-mantle boundary (CMB) heat flux heterogeneity, based on numerical dynamo simulations (e.g., Aubert et al., 2013; Christensen & Olson, 2003; Terra-Nova et al., 2019). Davies et al. (2008) reported a higher latitudinal variation of synthetic VGP dispersion in the southern hemisphere than the north, from a dynamo model run under thermal heterogeneous CMB conditions. However, VGP dispersion estimates observed from the geodynamo models were significantly lower when compared to PSV models (e.g., Johnson et al., 2008; McElhinny & McFadden, 1997).

3.1.5.3 Comparison with historical equivalent VGP dispersion

It is well known that snapshots of geomagnetic field models are not equivalent to TAF models (Hulot & Gallet, 1996; Kono & Tanaka, 1995; Merrill et al., 1998). Even so, McFadden et al. (1988) showed that VGP dispersion curve for the present geomagnetic field (computed from the IGRF65 model) is similar to the 0-5 Ma paleomagnetic field. Nevertheless, their results only considered the average VGP dispersion over both southern and northern hemispheres. Furthermore, Hulot and Gallet (1996) showed that historical VGP dispersion is highly time-dependent; for earlier historical periods, the similarity observed by McFadden et al. (1988) no longer holds. They also showed that the Gauss coefficients of degree and order (1,1), (2,1), (3,1), and (4,1) are the main terms that influence the shape of the VGP dispersion curve. Here, we further investigate the time dependence of the equatorial asymmetry in VGP scatter curves.

We evaluate the equivalent VGP dispersion for the historical period using the time-dependent geomagnetic field model COV-OBS based on stochastics methods (Gillet et al., 2015). Distributions of dispersion data were computed for each 5° latitude band, with 5° longitude spacing. Equivalent VGP dispersion curves from 1840 to 2015 in five-year intervals are shown in Figure 3.7a, considering VGP dispersion estimates between northern and southern hemispheres. As expected from previous observations (e.g., Hulot & Gallet, 1996; McFadden et al., 1988), the VGP dispersion tends to increase from the equator to the pole. However, for earlier epochs (before 1880) a decreasing dispersion from 60° latitude is observed. By comparing the Model G best-fit curves from this study with those for previous PSV studies for the 0-5 Ma (Opdyke et al., 2015) and 0-10 Ma (Cromwell et al., 2018) intervals, we detect an incompatibility between paleomagnetic VGP dispersions and equivalent VGP dispersions from a snapshot of historical geomagnetic fields, in contrast to the observations of McFadden et al. (1988). Nevertheless, latitudinal geomagnetic field variation for older periods (yellow curves in Figure 3.7a) and the 0-10 Ma paleomagnetic field (from this study using the Vandamme (1994) criterion) capture a similar pattern within the 0° to 40° latitudinal range.

When historical equivalent VGP dispersions are examined separately for each hemisphere, there is a pronounced equatorial PSV asymmetry especially for recent intervals of geomagnetic field behavior (Figure 3.7b). Neither the northern nor the southern hemisphere equivalent dispersions have any striking similarity compared to VGP dispersion curves from PSV data (Figure 3.7a). Southern hemisphere scatter is higher with a bump around 20°, which probably relates to the historical latitudinal position of the South Atlantic Anomaly (e.g., Amit et al., 2021; Hartmann & Pacca, 2009; Terra-Nova et al., 2017). In the northern hemisphere, there is a VGP dispersion decrease with latitude, with a bump at around 50-60° N. A similar feature was found by McFadden et al. (1988) for the IGRF65 model. These results highlight that the historical equivalent VGP dispersions produce higher equatorial asymmetry than that discussed in PSV studies. This could relate to the short time span of the geomagnetic field model, but should not be over-interpreted. Curiously, equivalent southern hemisphere dispersion better describes the paleomagnetic data than the equivalent northern hemisphere dispersion.

We also investigate the spherical harmonics responsible for the observed time evolution of equivalent VGP dispersion curves. First, we calculate dispersion distributions in terms of specific Gauss coefficients from the COV-OBS model for 1965 (Figure 3.7a). Following Hulot and Gallet (1996), we expand the investigation of how non-zonal harmonic

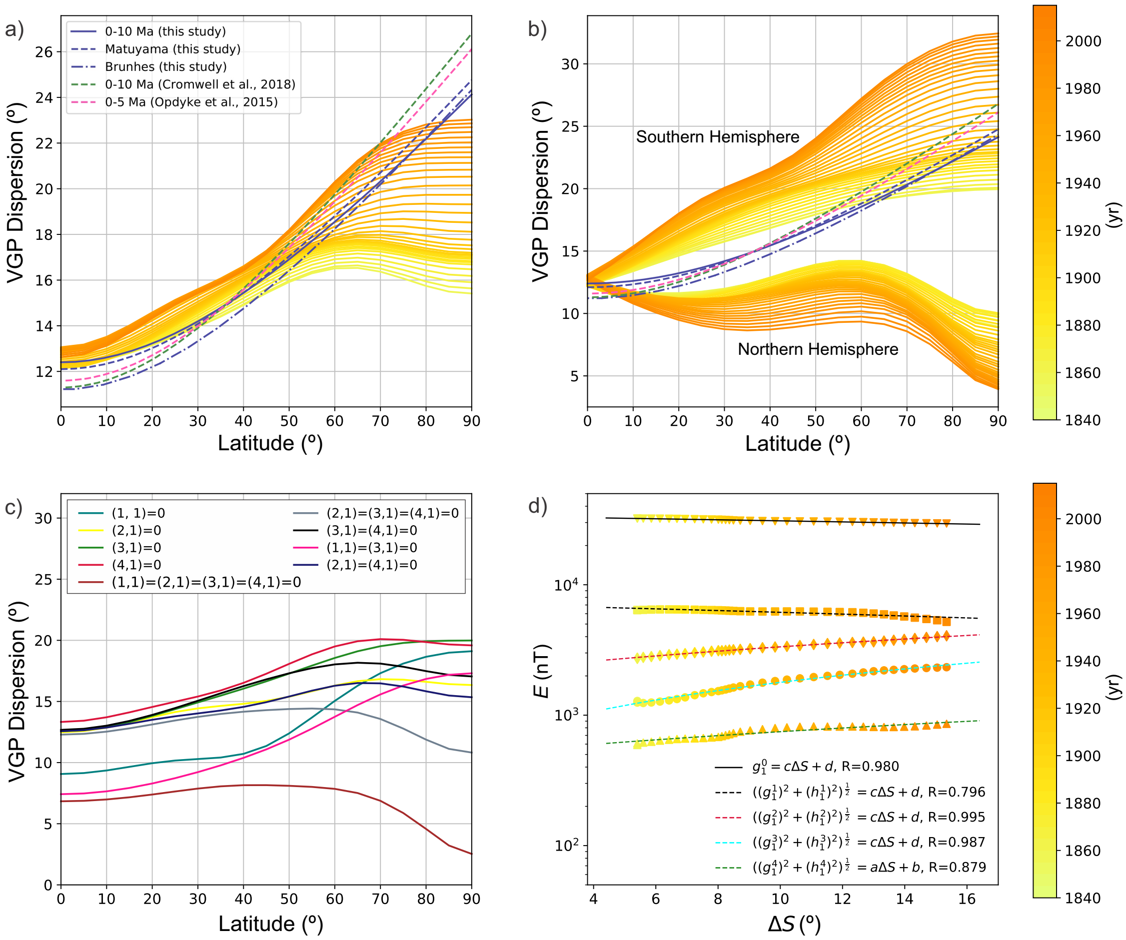

Figure 3.7 – Equivalent VGP dispersion as a function of latitude for the historical period from the COV-OBS field model (a) averaged over both hemispheres, (b) for the northern and southern hemispheres separately. (c) Equivalent VGP dispersion curves defined in terms of the Gauss coefficients filtered from the COV-OBS model for the 1965 epoch. (d) Average spherical harmonics energy as a function of interhemispheric variance (ΔS) from historical VGP dispersions. Solid and dashed lines correspond to linear regressions fitted to ΔS estimates defined for the axial dipole term (g_1^0) and four non-zonal harmonic terms, respectively.

terms of low degree ($l = 1, 2, 3, 4$) and order $m = 1$ alter the shape of the VGP dispersion curve. The nullifying of certain non-zonal harmonics changes significantly the latitudinal behavior of VGP dispersions. For instance, when the four non-zonal terms are reduced to zero, the dispersion distributions tend to decrease at high latitudes (> 60°; brown curve in Figure 3.7c).

To quantify hemispherical differences in the time evolution of historical equivalent VGP dispersions, we define the interhemispheric variance (ΔS) expressed by:

$$\Delta S(\lambda, t) = \sum_{0}^{\lambda=90} |S_{NH}(\lambda, t) - S_{SH}(\lambda, t)|, \tag{3.7}$$

where S_{NH} and S_{SH} are dispersion estimates for the northern and southern hemispheres, respectively. The higher ΔS, the more asymmetric are the northern and southern equivalent VGP dispersion curves. By evaluating the average energy of non-zonal harmonics as a function of ΔS estimates (Figure 3.7d), ΔS is observed to increase progressively with dipole field decay (including the axial g_1^0 term) and increased non-dipole field contributions over historical time. When establishing a linear regression to the data, a best-fit was found for the (2,1) term. Further investigation of ratios of non-dipolar fields at the CMB might clarify the source of this asymmetry but is beyond the scope of this study.

3.1.5.4 Evaluations of non-dipole zonal terms over the last 10 Myr

The new zonal TAF models fitted to ΔI data indicate a small non-dipole field contribution. Specifically, for the 0-10 Ma period, the best estimate for the axial quadrupole g_2^0 term is 3.2-3.7% of g_1^0, with a smaller axial octupole contribution g_3^0 ranging from 1.2 to 1.8% of (Table 3.1). Our results suggest that small departures from the GAD model have persisted over long timescales for the 0-100 ka and 0-5 Ma periods. From their GGF100k model (Global Geomagnetic Field for the 0-100 ka interval), Panovska et al. (2018b) revealed the presence of the zonal terms $G2 = 4.2\%$ and $G3 = 2.5\%$. For a statistical TAF model for the last 5 Myr, J08 suggests estimates of $G2 = 3.0\%$ and $G3 = 3.0\%$ from high-quality paleomagnetic data. From the PSV10 compilation, Cromwell et al. (2018) estimated axial quadrupole and octupole contributions of g_2^0= 3.0% of g_1^0 and g_3^0= 1.3% of g_1^0, respectively. The BB18.Z3 model (Bono et al., 2020) suggests values of $G2 = 2.9\%$ and $G3 = -1.3\%$ for the past 10 Myr. Thus, small non-GAD contributions seem to be a common feature of paleomagnetic field models.

3.1.5.5 Examining paleomagnetic inclinations relative to the GAD approximation

The question of the paleomagnetic field geometry found to be predominantly dipolar over the past million years has been debated (Johnson & McFadden, 2015; McElhinny, 2004). For the three time periods investigated in this study, our TAF models reveal low values of the $G2$ and $G3$ terms (Table 3.1). Following the previous TAF studies (e.g., Opdyke & Henry, 1969; Opdyke et al., 2015; Schneider & Kent, 1990), we also examine the latitudinal distribution of mean inclination data (applying the Vandamme (1994) cutoff) to test compliance with the expected GAD inclination (determined by the equation (3.5)), as shown in Figure 3.8.

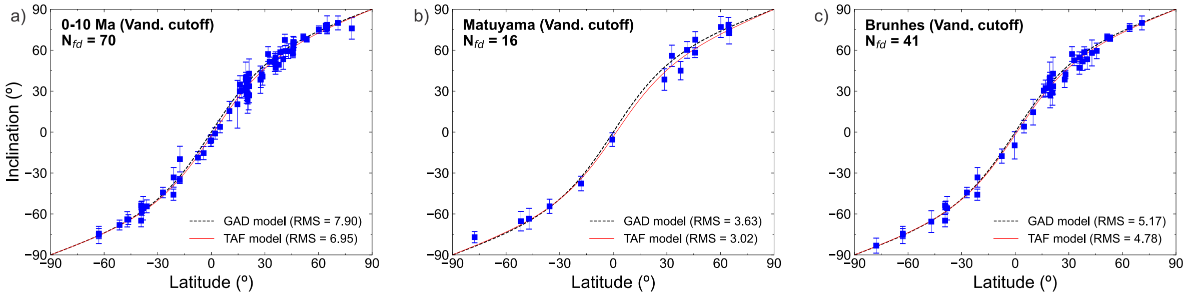

Figure 3.8 – Mean inclination as a function of latitude for (a) the 0-10 Ma interval, (b) Matuyama chron, and (c) Brunhes chron applying the Vandamme (1994) criterion. The uncertainties of the inclination data correspond to the 95% confidence cone (α_{95}) of the mean direction. Black curves represent the expected GAD inclination. Red curves are the inclination predicted for TAF models proposed in this study (see Table 3.1). Vand. = Vandamme (1994); RMS = root mean square.

Most of mean inclination data for the 0-10 Ma interval agree with the latitudinal variation curve from a GAD model (black dashed line in Figure 3.8a), and are not statistically different at the 95% confidence level relative to predicted GAD inclination. Similarly, Matuyama reverse and Brunhes normal polarity data (Figures 3.8b e 3.8c, respectively) show a close correspondence with the GAD inclination curve, considering the 95% uncertainties of the mean inclinations. Nevertheless, the Matuyama estimates at northern latitudes produce large deviations from the GAD prediction compared to the Brunhes chron.

For each age group, we calculate the weighted root mean square (RMS) deviation of the difference between the mean paleomagnetic inclination and the predicted GAD inclination. The weights correspond to the 95% uncertainties of the mean paleomagnetic direction. Our analyses show that the three temporal data sets are best-fit for the corresponding TAF models presented in this study (summarized in Table 3.1), with slightly lower RMS values than for GAD model. The inclination curves for TAF models (red line) are shown in Figure 3.8. These results suggest that the inclination estimates are compatible with the GAD field, however, the paleofield models with small $G2$ and $G3$ contributions provide a statistically acceptable fit to the observed inclination data. Furthermore, the non-dipole field components do not yield significant changes for the last 10 Myr.

3.1.5.6 Distinct PSV and TAF patterns: Brunhes normal and Matuyama reverse polarity data sets

Statistical analysis of PSV and TAF latitudinal behavior reveals differences between the Brunhes normal and Matuyama reverse polarity data, which partially supports the observations of J08. For PSV analysis, we examine Model G parameter estimates fitted to S_B data for both age groups, which differs from that presented by J08. Best-fit curves for Matuyama subsets yield higher S_B estimates at low latitudes compared to the Brunhes subsets, especially when a 45° cutoff angle is used to exclude outlier data (Figures 3.3 and 3.4). When compared to J08, our Matuyama estimates (using a fixed 45° cutoff) produce less latitudinal variation in the VGP dispersion curve (Figure 3.3c). However, the difference is not statistically significant with respect to Model G parameter b (Table 3.1 and Table S7). Differences between the two VGP dispersion curves are probably related to inclusion of new mid- to high-latitude (± 50–65°) records that were not included in J08 and that may have influenced the Model G fit. For the Brunhes chron (Figure 3.4c), our predicted S_B values for Model G are lower for J08, but Model G parameters in both studies are not statistically distinguishable at the 95% confidence level. The slight observed differences may be associated with the data sets distribution and size in both studies (Table 3.1 and Table S7).

According to some studies (Cromwell et al., 2018; Valet & Herrero-Bervera, 2011), high (low) S_B estimates for reverse (normal) polarity fields might be attributed to lower (higher) average paleointensity during the Matuyama (Brunhes) chron. Ahn and Yamamoto (2019) analyzed 0–5 Ma absolute paleointensity data from the PINT database (Biggin et al., 2009) and concluded that the Matuyama had a lower dipole field strength compared to the Brunhes period. Recent studies (Biggin et al., 2020; Meduri et al., 2021) have also pointed out an inverse relationship between the a parameter from Model G with the degree of dipole dominance, inferred from numerical geodynamo models. Here, the shape parameter a is higher for Matuyama data sets than for the Brunhes, whichever VGP cutoff is applied (Table 3.1). These findings suggest that the TAF was less dipolar during the Matuyama than the Brunhes chron. However, observed differences between Model G parameters for these two age groups are not statistically significant at the 95% confidence level.

Zonal TAF model fits for the Matuyama ΔI data result in higher quadrupole ($G2$ of 3.1–3.6%) and octupole ($G3$ of 2.0–2.9%) contributions compared to Brunhes estimates ($G2$ = 2.0–3.1% and $G3$ = 1.3–1.8%). The exception is the low value obtained for the $G2$ term by applying a fixed 45° cutoff (see Table 3.1). J08 reported estimates of $G2$ = 4% and $G3$ = 5% and $G2$ = 2% and $G3$ = 1% for the Matuyama and Brunhes chrons, respectively. The main differences in TAF estimates between the studies can be assigned to two factors: (a) incorporation of new data produced after J08 and (b) the formalism used for ΔI calculations (here ΔI estimates were calculated for each paleomagnetic study instead of latitude band averages, as adopted by J08). Furthermore, high estimates of non-dipole components detected for the Matuyama epoch could be linked to the lower dipolar paleofield dominance in this period than during the Brunhes chron.

Thermal and compositional heterogeneities at the CMB have been suggested as a possible explanation for differences between normal and reverse polarity fields, as debated in the literature (Johnson & McFadden, 2015). McElhinny and McFadden (1997) suggested that distinctions between these two polarity states, ascertained from the latitudinal behavior of 0–5 Ma VGP dispersions, could rather be caused by incompletely removed viscous overprints for reverse polarity data (with higher dispersion compared to normal polarity data). However, considering the high-quality data assessed in this study, we assume that this effect is minimized. Thus, polarity asymmetries in the PSV and TAF models for Matuyama and Brunhes subsets appear to be an empirical feature of the paleomagnetic field, which corroborate earlier observations (e.g., Cromwell et al., 2018; Johnson et al., 2008).

3.1.6 Conclusions

1. An upgraded database of high-quality igneous paleodirections produced using rigorous selection criteria, provides robust PSV and TAF assessments for the Brunhes and Matuyama chrons over the 0–10 Ma period. The new data compilation contains 2,543 paleomagnetic sites covering the past 10 Myr, which improves the temporal and spatial distributions of paleodirectional data relative to the previous PSV10 database (Cromwell et al., 2018).

2. VGP dispersion patterns from the 0–10 Ma data set, and from Matuyama and Brunhes subsets, are well-fitted by an adapted Model G (McFadden et al., 1988) that differs slightly from the dispersions predicted by the GGP models BCE19 (Brandt et al., 2020) and BB18 and BB18.Z3 (Bono et al., 2020). It is noteworthy that the BCE19 model and BB18-family models were designed to fit, respectively, paleodirectional and VGP dispersion estimates in the PSV10 compilation.

3. The VGP dispersion curve fitted for new 0–10 Ma data sets using Model G produces lower latitudinal dependence of S_B than the PSV10 data set. Analyses of the S_B data as a function of latitude suggest that differences in the shape of Model G curves are associated

with data selection and calculation methods for PSV estimates. Our results differ by including more stringent quality criteria (with $N \geq 10$, $n \geq 5$), and assess latitudinal PSV variation by locality using the Deenen et al. (2011) criterion rather than mean S_B values by latitude bands.

4. New zonal TAF model for the 0–10 Ma interval indicate the presence of small non-dipole field contributions, with an axial quadrupole component $G2$ = 3.2–3.7% and a smaller axial octupole component $G3$ = 1.2–1.8%.

5. Assessments of the latitudinal PSV behavior do not provide clear evidence of a north-south hemispheric asymmetry in VGP dispersion for 0–10 Ma data sets. Brunhes chron data have differences between hemispheres that are characterized by a stronger latitudinal S_B dependence in the southern relative to the northern hemisphere, especially when the Vandamme (1994) cutoff is used. This finding suggest that equatorial asymmetry of geomagnetic secular variation has persisted over the last 780 ka.

6. Statistical simulations from the COV-OBS model for the 1965 epoch indicate that the reduction or combined effect of non-zonal harmonic terms (1,1), (2,1), (3,1), and (4,1) to zero implies significant modifications in the shape of the equivalent VGP dispersion curve. Furthermore, investigations of the historical evolution of dispersion estimates for the northern and southern hemispheres indicate an equatorial asymmetry of VGP scatter that gradually increases with time, which can be associated with dipole field decay and increased non-dipole field contributions.

7. We report differences between Brunhes normal and Matuyama reverse polarity data in both PSV and the TAF analysis. The Matuyama subset produces higher S_B patterns at low latitudes than the Brunhes chron. In terms of non-GAD TAF structure, zonal quadrupole and octupole contributions are larger for the Matuyama chron (with $G2$ = 3.1–3.6% and $G3$ = 2.0–2.9%) compared to the Brunhes ($G2$ = 2.0–3.1% and $G3$ = 1.3–1.8%), which support observations of lower and higher average paleointensities for the respective periods.

8. Finally, additional high-quality data are essential to enhance temporal and geographic sampling of the 0–10 Ma database (especially data coverage older than 1 Ma and new

southern hemisphere records), and to better understand long-period geomagnetic field asymmetries.

Acknowledgments

The authors acknowledge the comments and suggestions of A. Roberts and an anonymous reviewer, and the editorial work of J. Feinberg. This work was supported by grants from the Conselho Nacional de Desenvolvimento Científico e Tecnológico (CNPq, #165161/2018-3, #425728/2018-8, #312737/2020-3). A. J. Biggin and Y. A. Engbers acknowledge support from The Leverhulme Trust (RLA-2016-080), and R. K. Bono acknowledges support from The Leverhulme Trust (ECF-2020-617).

4. PALEOSECULAR VARIATION IN THE EQUATORIAL SOUTH AMERICAN REGION

This chapter presents a scientific article published in *Physics of the Earth and Planetary Interiors* journal. Supplementary material is provided in the online version of the article below and Appendix E.

Wellington P. de Oliveira, Gelvam A. Hartmann, Jairo F. Savian, Giovanny Nova, Mauricio Parra, Andrew J. Biggin, Ricardo I. F. Trindade. Paleosecular variation record from Pleistocene-Holocene lava flows in southern Colombia (2022). *Physics of the Earth and Planetary Interiors*, *332*, 106926. https://doi.org/10.1016/j.pepi.2022.106926

4.1 Paleosecular variation record from Pleistocene-Holocene lava flows in southern Colombia

Abstract

Improvements in the spatial and temporal coverage of paleomagnetic data are essential to better evaluate paleofield behaviour over the past 10 Myr, especially due to data scarcity at low latitudes in the South American region. Here, we provide new Pleistocene-Holocene (0-2 Ma age interval) paleodirectional data from three volcanic systems (Doña Juana Volcanic Complex, Galeras Volcanic Complex and Morasurco Volcano) in southwestern Colombia between latitudes 1.2° and 1.4°N. A total of 38 paleodirectional sites were studied using progressive alternating field and thermal demagnetization treatments. After excluding transitional data, we obtain thirty site-mean directions for analysis of paleosecular variation (PSV) and the time-averaged field (TAF) in the study area. The mean direction (Dec = 351.2°, Inc = -3.4°, α_{95} = 6.2°, k = 20.0) and the paleomagnetic pole (Plat = 80.7°N, Plon = 173.1°E, A_{95} = 5.2°, K = 29.1) of these sites are not statistically compatible with the expected geocentric axial dipole (GAD) field direction and geographic north pole, respectively. Virtual geomagnetic pole dispersion (S_B) for our filtered dataset ($S_{B(2Ma)} = 15.2_{12.0}^{17.6^\circ}$) and the Brunhes chron ($S_{B(Bru)} = 16.0_{11.6}^{19.1^\circ}$) are consistent at the 95% confidence level with South American studies at equatorial latitudes and recent PSV models for the 0-10 Ma and Brunhes intervals. Likewise, the corresponding inclination anomaly (ΔI) for two age groups $\Delta I_{2Ma} = -5.9_{-12.1}^{0.3^\circ}$ and $\Delta I_{Bru} = -5.3_{-13.7}^{3.1^\circ}$ suggests large deviations relative to the GAD model, in accordance with

predictions from zonal TAF models. The high VGP dispersion could be linked to strong longitudinal variability of the magnetic field position over South America. This feature reflects the presence of significant non-dipole field components in this region that have been detected in geomagnetic field models for the most recent centuries and millennia, probably associated with the presence of the South Atlantic Magnetic Anomaly in the South American region.

Keywords: Paleosecular Variation, Time-Averaged Field, Virtual Geomagnetic Pole Dispersion, Inclination Anomaly, Southwest Colombia, Magnetic Equator.

4.1.1 Introduction

Earth's magnetic field has a dominantly internal origin and varies both in direction and intensity over a wide range of timescales. Investigations into paleosecular variation (PSV), which is manifest as long-period (10^5-10^6 years) geomagnetic variations (Johnson & McFadden, 2015), provide valuable information about geomagnetic field evolution and constraint numerical geodynamo simulations (Biggin et al., 2020; Coe & Glatzmaier, 2006; Davies & Constable, 2014; Lhuillier et al., 2013; Sprain et al., 2019). When PSV is averaged over a long interval, the time-averaged field (TAF) can be represented to first approximation by a geocentric axial dipole (GAD; Merrill & McFadden, 2003). This assumption is central to paleomagnetism with applications for plate tectonic reconstructions (Tauxe, 2003).

Geological records from volcanic rocks are considered highly appropriate for determining the statistical properties of paleofield behaviour over the past few million years. These materials offer instantaneous readings of the paleomagnetic field in contrast to the smoothed recording in sedimentary rocks (Hulot et al., 2010). Over the past 14 years, global compilations of high-quality paleomagnetic data (from lava flows and thin dykes) have been produced for the last 5 Myr (Johnson et al., 2008; Opdyke et al., 2015) and 10 Myr (Cromwell et al., 2018) to constrain PSV and TAF models. de Oliveira et al. (2021) presented an updated 0-10 Ma database that improves the geographic and temporal coverage of paleodirectional data compared to previous compilations.

A statistic commonly employed to quantify PSV is the angular dispersion of virtual geomagnetic poles (VGPs) for a certain location. Several PSV models (e.g., Bono et al., 2020; Brandt et al., 2020; Constable & Parker, 1988; Tauxe & Kent, 2004) have been developed to describe the latitudinal dependence of PSV based on spherical harmonic analyses fitted to VGP dispersion data. Model G (McFadden et al., 1988) assumes that overall dispersion can be described by separating two independent families. These are primary and secondary families, respectively, associated with asymmetrical (e.g., axial dipole) and symmetrical (e.g., axial quadrupole) harmonic terms about the equator. This model has been employed widely in evaluations of PSV behaviour over Phanerozoic timescales (e.g., Biggin et al., 2008b; de Oliveira et al., 2018; Doubrovine et al., 2019; Franco et al., 2019; Handford et al., 2021; Veikkolainen & Pesonen, 2014) and provides important insights into geomagnetic field stability. For the 0-10 Ma period, strong latitudinal variation of the VGP dispersion curve has been reported in two studies (Cromwell et al., 2018; de Oliveira et al., 2021), although small differences were observed in the Model G curves mainly due to the methods used to calculate the VGP dispersion. The data selection of de Oliveira et al. (2021) includes a minimum of 10 paleomagnetic sites per selected study and at least 5 samples per site, which differs from a previous compilation (Cromwell et al., 2018).

Insights can also be gained into paleomagnetic field morphology from PSV studies. Statistical analysis of the latitudinal pattern of inclination anomaly data spanning the last 10 Myr enables TAF models (Bono et al., 2020; de Oliveira et al., 2021) to suggest the existence of axial quadrupole and octupole contributions less than 5% of the axial dipole term. The presence of small non-GAD terms appears similar to geomagnetic field models for the 0-5 Ma (Johnson et al., 2008; McElhinny et al., 1996) and 0-100 ka intervals (Panovska et al., 2018b). However, the detailed structure of average paleomagnetic field reconstructions is limited by the non-uniform spatial and temporal distributions of paleodirectional data. In particular, South America contributes only 10% of the current 0-10 Ma database (de Oliveira et al., 2021). There are also few PSV studies at low latitudes (e.g., Leonhardt et al., 2003; Opdyke et al., 2006; Sánchez-Duque et al., 2016), which is a region with negative inclination anomalies (> -2°) associated with a persistent zonal quadrupole component. Therefore, acquisition of new paleomagnetic records is essential to better assess the latitudinal TAF structure and long-term geomagnetic variations.

In this study, we present high-quality paleodirectional data from Pleistocene-Holocene lava flows from the southwestern region of Colombia's Northern Volcanic Zone (NVZ) at latitudes of 1.2°-1.4°N. Additionally, we provide reliable estimates of VGP dispersion and inclination anomaly from a careful selection of site-level data. These results are compared with low latitude paleomagnetic data to assess the validity of recent PSV and TAF models for the 0-10 Ma interval.

4.1.2 Geologic setting

The present morphology of Colombia's NVZ originated from subduction and collision of Pacific-related plates, including the Farallon, Nazca, and Caribbean plates beneath or against the South American plate, respectively (Montes et al., 2019; Taboada et al., 2000; Wagner et al., 2017). These interactions triggered uplift of the Northern Andes (extending from Colombia to the Ecuador), which in Colombia is divided into three mountain ranges, the Western, Central and Eastern Cordilleras (Figure 4.1a). One of the main geological features is the Romeral Fault System (RFS), which delimits oceanic crustal basement of the Western Cordillera from continental basement of the intermontane Cauca Valley to the east in the Central Cordillera. The eastern side of the RFS consists of medium-grade metamorphic Triassic-Jurassic rocks (Spikings et al., 2015), a Triassic sedimentary succession (Cediel et al., 1981; Mojica, 1980) and Jurassic intrusive bodies (e.g., Ibague Batholith, Sombrerillo Batholith, Mariquita Stock) (Bustamante et al., 2016; Cochrane et al., 2014; Rodríguez et al., 2018), and volcano-sedimentary sequences (Bayona, 1994; Bayona et al., 2020; Mojica & Prinz-Grimm, 2000). To the west, the NVZ is composed of Cretaceous low-grade metamorphic belts and oceanic mafic rocks (Quebradagrande and Arquia Complexes) related to the Caribbean Large Igneous Province (Kerr et al., 1996; Pindell & Kennan, 2009; Villagómez et al., 2011), and including Cenozoic granodioritic plutons (Jaramillo et al., 2017; Zapata et al., 2019).

Over the NVZ basement, a series of volcanoes was built along the Central Cordillera as a result of magmatic and tectonic activity from the western continental margin of Colombia since the Miocene (Monsalve-Bustamante, 2020; Ramos, 2009). The present study focuses on three stratovolcanoes located in the southwest Colombian Andes (1.2-1.4°N, 76.9-77.4°W; Figure 4.1a): the Doña Juana Volcanic Complex (DJVC), Morasurco Volcano, and Galeras Volcanic Complex (GVC). These stratovolcanoes are mainly composed of dacite and andesite lava flows with calc-alkaline affinity interlayered with pyroclastic deposits, associated with effusive and explosive events that occurred over the last 2.5 Myr (Monsalve-Bustamante, 2020). A general description of the geologic units of each volcano is given below.

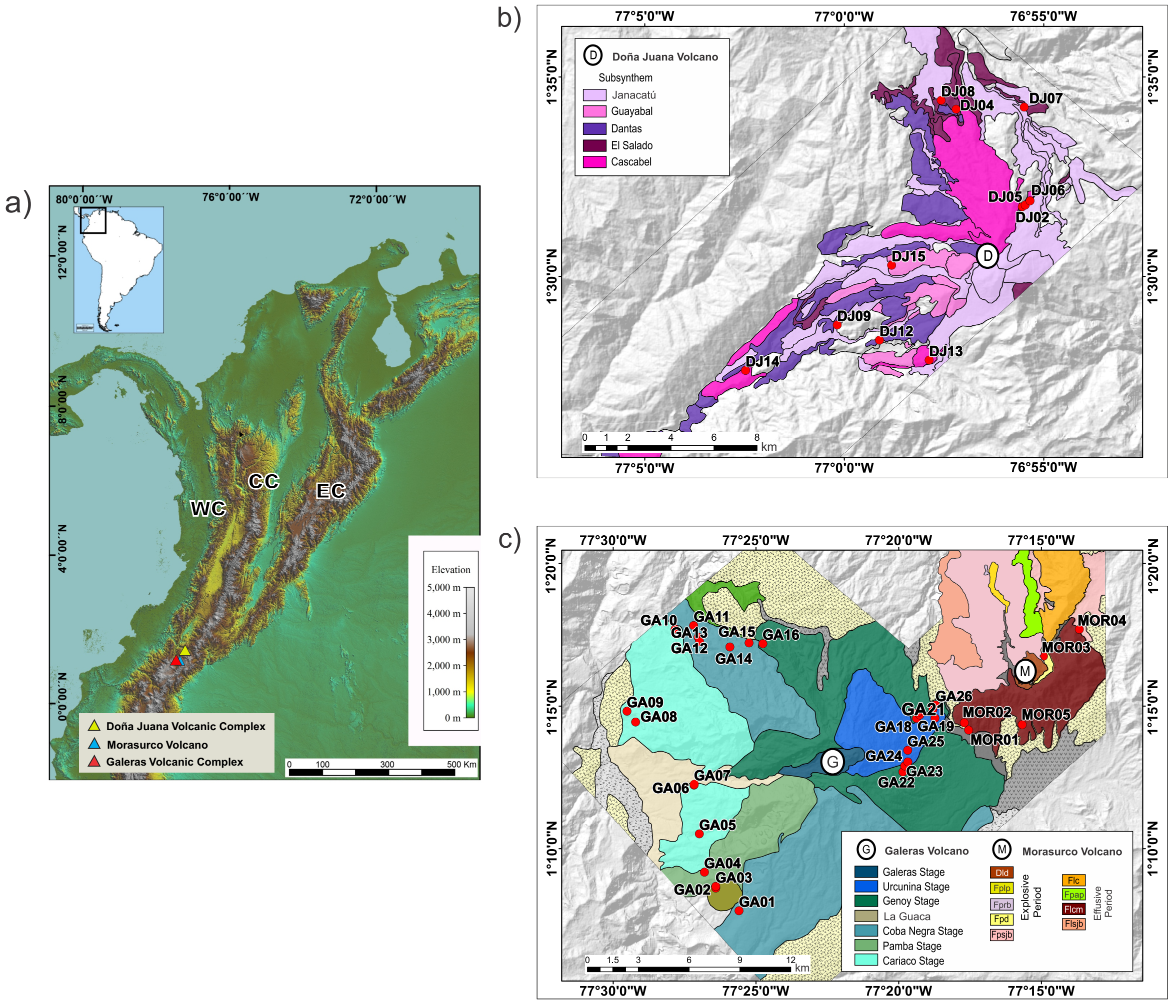

Figure 4.1 – (a) Topographic map of Colombia (WC: Western Cordillera; CC: Central Cordillera; EC: Eastern Cordillera) with the location of the three studied volcanic systems. Geologic maps of (b) Doña Juana Volcanic Complex, and (c) Morasurco Volcano and Galeras Volcanic Complex. Red circles indicate paleomagnetic site locations. Modified from Pardo et al. (2019), Trujillo et al. (2010), and Calvache et al. (1997).

The DJVC contains several types of volcanic deposits such as pyroclastic flows, lava flows and ash beds with ages ranging from 1125.4 ± 4.4 ka to the present-day, supported by $^{40}Ar/^{39}Ar$ and ^{14}C datings (Pardo et al., 2019). These authors defined five unconformity-bounded lithostratigraphic units, referred to as subsynthems, based on structural angular unconformities and include lithosomes (defined for eruptive centers) in the volcanic area (Figure 4.1b) as follows. (1) The Cascabel Subsynthem corresponds to the oldest volcanic deposits (between 1125.4 ± 4.4 ka and 1097 ± 39 ka) that overlap the Cretaceous metamorphic basement. It comprises dacitic and andesite lava flows of the Santa Helena Lithosome, and includes ignimbrites, lahar deposits and porphyritic dacites from the Animas Lithosome. (2)

The El Salado Subsynthem, which consists of lava dome, welded ignimbrite, lahar and lapilli tuff deposits of the Animas Lithosome emplaced from 1097 ka to 878 ka. (3) The Dantas Subsynthem is composed of massive ash-flow deposits and andesitic to dacitic lava flows related to the Ancestral Doña Juana Lithosome, with ages ranging between 878 ± 2.8 ka and 312 ± 28.8 ka. (4) The Guayabal Subsynthem (from 230.8 ± 13.3 ka to 76.8 ± 18 ka) comprises ignimbrites and dacitic lava flows from the Old Doña Juana Lithosome, massive tuffs from the Animas Lithosome and debris-avalanche deposits from the Montoso Lithosome. (5) The Janacatú Subsynthem represents the youngest volcanic deposits, consisting of block-ash flows and lahars from the Young Doña Juana Lithosome, pyroclastic deposits and ignimbrites from the Animas Lithosome, and lahar and hyperconcentrated flow deposits from the Totoral Lithosome. Its period of volcanic activity is dated between 4400 ± 30 yrs BP and 1936 AD.

The Morasurco Volcano is considered inactive and is located to the southwest of the DJVC (Figure 4.1c) with volcanic deposits dated to 1.6-2.2 Ma based on zircon fission-track and K/Ar methods (Trujillo et al., 2010). The authors recognized five lava flow units and four pyroclastic flows associated with two eruptive phases. The first phase corresponds to an effusive event with a large volume of basaltic andesite lava flows distributed around the volcanic center and include the San Juan Bajo lava flow (Flsjb), undifferentiated Cerro Morasurco lava flow (Flcm), Alto de Piedras lava flow (Flap) and Loma La Cocha lava flow (Flc). A subsequent event is restricted to explosive activity, characterized by deformation of the volcanic edifice, which is partially destroyed and comprises pyroclastic deposits named the San Juan Bajo pyroclastic flow (Fpsjb), Daza pyroclastic flow (Fpd), Río Bermúdez pyroclastic flow (Fprb), Quebrada Las Palmas pyroclastic flow (Fplp) and Daza Lava Dome (Dld).

The Galeras Volcano (Figure 4.1c) is regarded as the most active volcano in Colombia (Calvache & Trujillo, 2016), and can be divided stratigraphically into six Late Pleistocene-Holocene geologic stages (Calvache et al., 1997). The oldest volcanic materials belong to the Cariaco stage, which is composed of lava or dome collapse flows, andesite lavas and ash and blocks of pyroclastic flow deposits dated at 1.1 ± 0.1 Ma (K-Ar; Cepeda, 1985). The subsequent products of explosive eruption of the Pamba stage (1.1-0.793 Ma) consist of partially welded block and ash flow deposits. This episode is succeeded by the Coba Negra stage, which consists of andesitic to basaltic and occasionally dacitic lava flows deposited over 793-288 ka ($^{40}Ar/^{39}Ar$). La Guaca (166 ± 34 ka; $^{40}Ar/^{39}Ar$) is designated as a monogenetic cinder cone on the southwestern part of the GVC. Its deposits are mainly composed of olivine-bearing basaltic andesites. Explosive eruptions followed during the Genoy stage that produced pyroclastic deposits with ages between 159 ± 21 ka ($^{40}Ar/^{39}Ar$) and 41 ± 1.5 ka (^{14}C). The next episode occurred during the Urcunina stage, characterized by andesite lava flows with pyroclastic flows in the age range from 41 ± 1.5 to 12.8 ± 0.3 ka (^{14}C). The youngest stage, termed Galeras, is situated in the center of the GVC. The volcanic products consist of pyroclastic flows, pyroclastic falls, mud and debris flows with ^{14}C ages covering the last 4500 years.

4.1.3 Sampling

A total of 42 paleomagnetic sites were sampled in southern Colombia during June 2019 (Figures 4.1 and 4.2) at altitudes between 1404 and 3289 m.a.s.l. (meters above sea level). Eleven sites were sampled in the DJVC and twenty-six and five sites were sampled from the Galeras and Morasurco volcanoes, respectively. All volcanic sites correspond to individual Pleistocene to Holocene lava flows (predominantly andesites) from different geological formations within the study area (Calvache et al., 1997; Pardo et al., 2019; Trujillo et al., 2010). Most of the paleomagnetic targets were accessed by paved roads and tracks around the three stratovolcanoes, but long hikes were made to access some lava outcrops. All sampling sites appeared unaltered. Site coordinates were obtained with a portable global positioning system device. An average of 9 core samples 2.5 cm in diameter and ~10 cm in length were collected at each site with a handheld gasoline-powered drill. Cores were oriented with a magnetic compass. It was not possible to obtain sun compass measurements due to cloud cover. It is worth noting that the natural remanent magnetization (NRM) intensities (Table S1) of the samples are low (<1 A/m) in order not to affect the magnetic compass needle.

4.1.4 Methods

4.1.4.1 Paleodirectional experiments

All paleomagnetic experiments were carried out in the Paleomagnetism Laboratory at the University of São Paulo (USPMag). For paleodirection measurements, oriented samples were sliced into 1.2 cm-long specimens and were subjected to stepwise thermal demagnetization (THD) and alternating-field demagnetization (AFD) procedures in a magnetically shielded room. THD was performed using an ASC Scientific Model TD48 oven.

Figure 4.2 – Fieldwork images of the paleomagnetic sites sampled. (a) Site DJ08 (Doña Juana Volcano), (b) site MOR04 (Morasurco Volcano) with core sample drill holes (below), and (c) sites GA17 and GA21 (Galeras Volcano).

Magnetic measurements and AFD were made using a 2G Enterprises cryogenic magnetometer equipped with a RAPID (Rock and Paleomagnetism Instrument Development) system. At least five specimens from each site (577 specimens in total) were subjected to AFD (393 specimens) in 18 steps up to 100 mT or using THD treatment (184 specimens) in 15 steps from room temperature to 600 °C. From measurements of pilot specimens (two specimens per site), AFD was employed in preference to THD because the latter yielded noisy data or magnetizations decreased rapidly during the first demagnetization steps for most pilot specimens.

4.1.4.2 Data analysis procedures

Characteristic remanent magnetization (ChRM) directions from individual specimens were determined using principal component analysis (Kirschvink, 1980). Data from at least six consecutive demagnetization steps represented in Zijderveld diagrams (Zijderveld, 1967) were used for ChRM estimation, as long as directions trended toward to the origin of the Zijderveld diagram and have a maximum angular deviation (MAD) $\leq 5°$. Site-mean directions were calculated using an approximate uncertainty propagation for specimen ChRM directions (Table S1) proposed by Heslop and Roberts (2020), which is applied to Fisher (R. A. Fisher, 1953) distributed data. Similar to the criterion used by de Oliveira et al. (2021), we considered at least five specimens per site ($n \geq 5$) with precision parameter (Banerjee et al., 2005) values of $k \geq 50$. Furthermore, the paleomagnetic results were evaluated applying the Vandamme (1994) criterion, which allows identification of excursional sites and outlier data that could be possibly related to the self-reversed thermoremanent magnetizations (TRMs), as reported in andesite rocks from the northern Colombian Andes (Haag et al., 1990; F. Heller et al., 1986). We do not use a fixed 45° cutoff for VGP data because it could lead to overestimation (underestimation) of VGP scatter for low and high latitudes (de Oliveira et al., 2021; Franco et al., 2019).

4.1.4.3 Magnetic mineralogy measurements

Rock magnetic experiments were performed on one sample per site (from 21 representative sites) to examine thermal stability during heating-cooling cycles in magnetic susceptibility measurements, and to determine the magnetic carriers and their magnetic domain states. Thermomagnetic susceptibility $\chi(T)$ curves were measured for crushed samples with a KLY4 Kappabridge susceptibility meter coupled to a CS-3 furnace (AGICO). Heating cycles were measured from 30 °C to 700 °C (at 12 °C/min) in air with subsequent cooling to 40 °C. The Curie temperatures (T_c) of all samples were determined from the second derivative approach (Tauxe, 2003), which have been used also for $\chi(T)$ curves (e.g., Aldana et al., 2011; Gautam et al., 2004; Salminen & Pesonen, 2007). From a single small rock fragment per site, hysteresis loops, isothermal remanent magnetization (IRM) acquisition curves, and first-order reversal curves (FORCs) were measured using a Princeton Measurements vibrating sample magnetometer (VSM) MicroMag 3900, with its maximum applied fields at room temperature. The hysteresis parameters, saturation magnetization (M_s), saturation remanence magnetization (M_{rs}), coercive force (H_c) and coercivity of remanence (H_{cr}) were used to investigate the domain structures of magnetic minerals. Plotting these parameters on a Day diagram (Day et al., 1977) is unsuitable for identifying multiple magnetic components (A. P. Roberts et al., 2018), so FORC diagrams (A. P. Roberts et al., 2000) allow better assessment of mineralogical composition and magnetic domain states in mixed magnetic particle systems (A. P. Roberts et al., 2014; Zhao et al., 2017). FORC measurements were made with an averaging time of 100 ms; 200 FORCs were measured. All FORC data were processed using the FORCinel software (Harrison & Feinberg, 2008) with a smoothing factor of 5.

4.1.5 Results

4.1.5.1 Rock Magnetism

The selected samples have variable thermomagnetic curves (Figure 4.3a-c; Figure E.1) with up to two magnetic transition temperatures inferred using the maximum in the second derivatives for the heating curves. About 52% of samples have a single ferrimagnetic phase with high transition temperatures of 516-594 °C (Figures 4.3b), which suggest the presence of Ti-poor titanomagnetite, pure magnetite or maghemite (Dunlop & Özdemir, 1997; Evans & Heller, 2003). Other samples contain two magnetic phases with Curie temperatures between 189 and 603 °C (see Table E.1), which indicate the presence of titanomagnetite with different Ti contents (Evans & Heller, 2003; Lattard et al., 2006). In particular, samples DJ07 and MOR02 (Figures 4.3a and c) have, respectively, a secondary transition temperature at 421 °C and 497 °C (associated with a hump shaped behaviour in the heating curves), which could be attributed to the presence of oxidized titanomagnetite or titanomaghemite (Dunlop & Özdemir, 1997). In general, the heating-cooling curves are irreversible with higher magnetic susceptibility during the heating cycle than during cooling. Non-reversible behaviour indicates alteration of magnetic minerals during measurement.

Hysteresis loops are narrow (Figure 4.3d-f and Figure E.2) with low coercivity $H_c <$ 20 mT (Table E.1) and a small paramagnetic mineral fraction. IRM curves saturate in fields from 0.15 to 0.4 T (Figure 4.3g), which suggests a major contribution from low-coercivity minerals.

These results are typical of magnetite, titanomagnetite, and partially oxidized magnetite and titanomagnetite (Dunlop & Özdemir, 1997). Day plot is provided in Figure E.3.

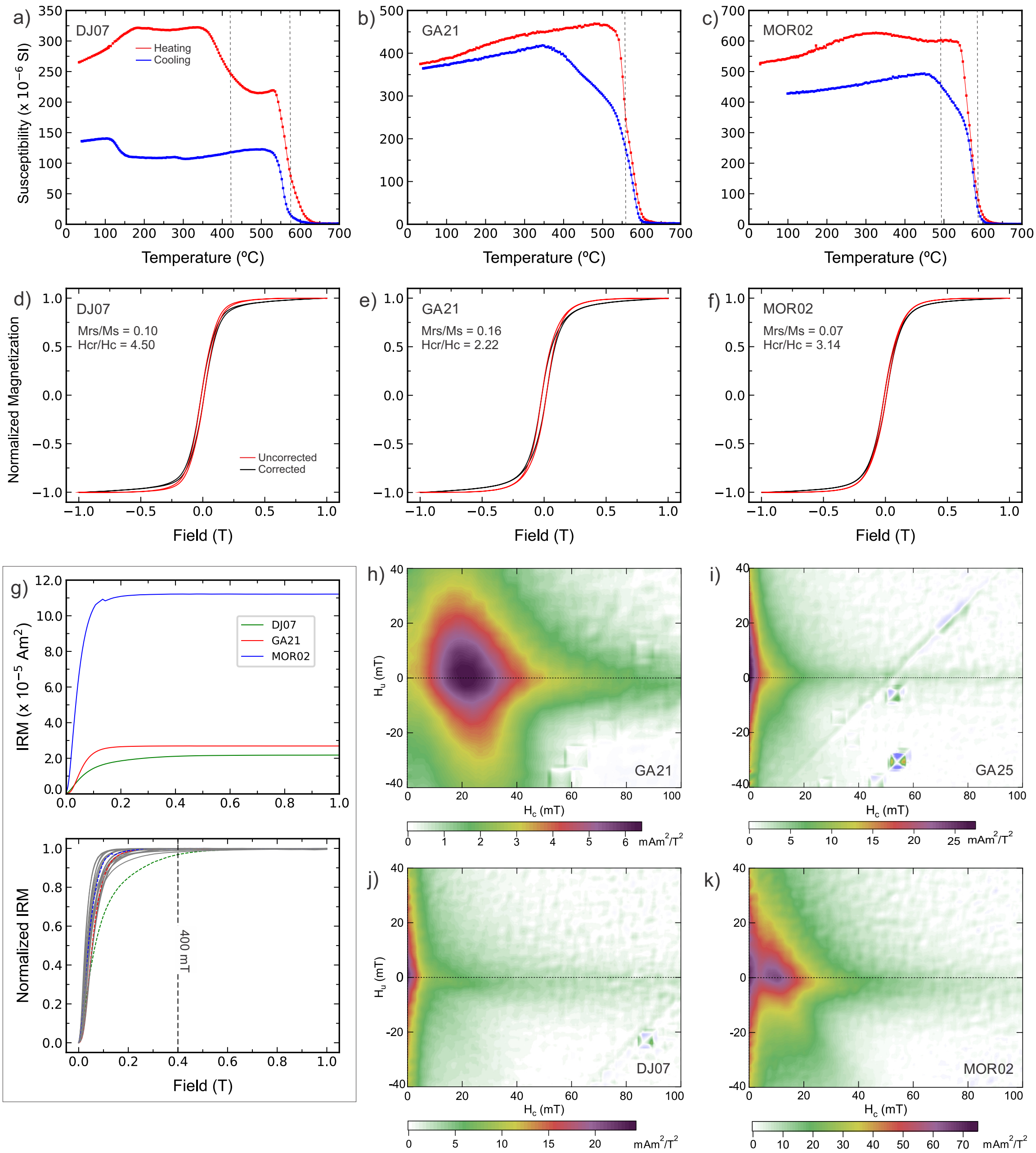

Figure 4.3 – Rock magnetic results for representative samples. (a-c) Thermomagnetic curves with heating (red curve) and cooling (blue curve) cycles. Dashed lines indicate the magnetic transition temperatures. (d-f) Normalized hysteresis loops, where red curves are not corrected for high field slopes. (g) IRM acquisition curves for 3 sites (top) and normalized IRM results for 21 sites (bottom). (h-k) FORC diagrams with magnetic domain structures for (h) vortex, (i-j) multidomain (MD), and (k) a mixture of vortex state and MD grains. IRM = isothermal remanent magnetization; FORC = first-order reversal curve.

From FORC diagrams, we identify two magnetic domain patterns (Figure 4.3h-k). The first reveals the existence of vortex state particles (Egli, 2021; Lascu et al., 2018; A. P. Roberts et al., 2017), which are characterized by moderate elongation over the vertical (H_u) axis and H_c values below 60 mT, with strong vertical spreading due to vortex nucleation (Figure 4.3h). Another FORC configuration indicates the presence of multidomain (MD) grains with a large spread of outer contours along the H_u axis and a H_c peak below 10 mT (Figure 4.3i-j). Some samples have two contributions with a mixture of vortex and MD particles, as shown in Figure 4.3k. FORC diagrams for other paleomagnetic sites are presented in Figure E.4.

4.1.5.2 Paleodirection

ChRM components were determined for 38 paleomagnetic sites using both AFD and THD. Only four sites (DJ09, DJ12, DJ14, and GA06) failed to produce acceptable results because of highly scattered data (see Figure E.5). Examples of representative demagnetization diagrams (Zijderveld plots) are shown in Figure 4.4. In general, NRM directions are well grouped, with ChRM directions defined by the best-fit line for data that converge to the origin of the plots after removal of viscous components with AFD >5 mT (Figures 4.4a and c) or >200°C (Figures 4.4b and d). AFD and THD yield similar results for specimens measured at the same site (e.g., Figure 4.4e-f).

Our dataset comprises 36 site-mean directions (summarized in Table 4.1) that satisfy the selection criterion described in section 4.1.4.2. For further TAF and PSV analysis, we discarded 6 out of 36 sites that are considered to record transitional directions by applying the Vandamme (1994) criterion (Figure 4.5a). Among these, 21 sites have normal polarity and 9 have reversed polarity. The normal and reversed polarity directions pass a bootstrap reversals test (Tauxe, 2010) within the 95% confidence region (Figure E.6), which allows calculation of the mean direction by combining these two groups of sites. Furthermore, our dataset ($N = 30$ sites) passes the quantile-quantile (Q-Q) test (N. I. Fisher et al., 1987) at the 95% confidence level, with statistical parameters $M_u = 1.190$ and $M_e = 0.462$ below critical values M_u'=1.207 and M_e'=1.094, respectively (Tauxe, 2010)(Figure E.7). This fact supports the hypothesis that declination and inclination data are distributed uniformly and exponentially, respectively. After converting reversed polarity data to normal polarity, the overall mean direction for N=30 sites is declination (D) = 351.2°, inclination (I) = -3.4°, and 95% confidence cone (α_{95}) = 6.2°, which

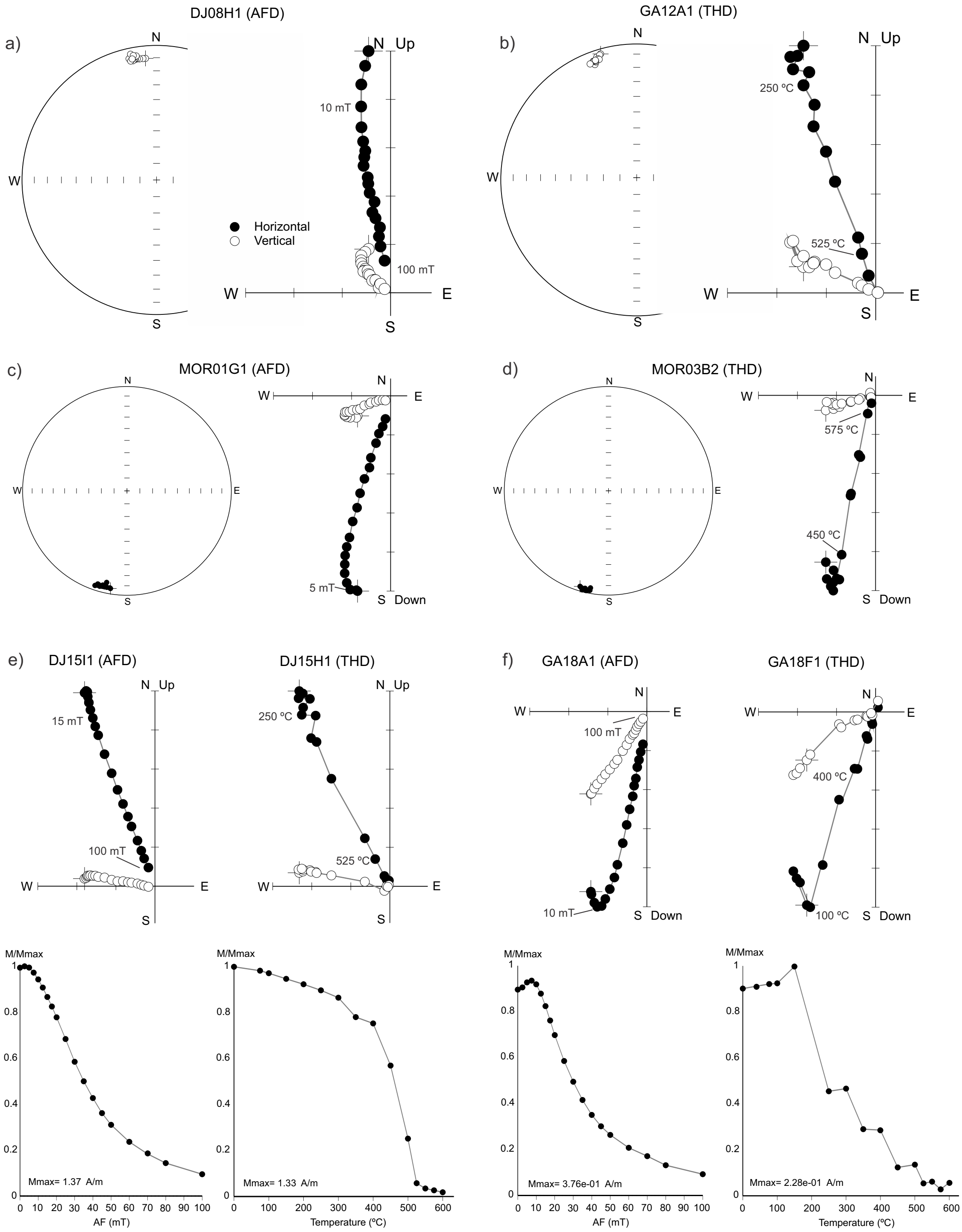

Figure 4.4 – Examples of demagnetization diagrams. Zijderveld diagrams and stereographic projections of NRM components obtained during (a and c) alternating field demagnetization (AFD) and (b and d) thermal demagnetization (THD). (e-f) Orthogonal projections of sister specimens using two demagnetization methods with demagnetization curves (below). Filled (open) circles correspond to vector components in the horizontal (vertical) plane for Zijderveld projections and upper (lower) hemisphere for stereographic projections. NRM = natural remanent magnetization.

Table 4.1 – Summary of paleodirectional results.

Site	Altitude (m)	Slat (°N)	Slon (°E)	Slat* (°N)	Slon* (°E)	n/N	Demag	Dec (°)	Inc (°)	k	α_{95} (°)	Vlat (°N)	Vlon (°N)	A_{95} (°)	Pol	Age (Ma)	Ref
DJ02	3101	1.529	283.074	1.470	283.129	7/16	AF	222.5	54.6	114.9	6.1	-36.0	240.4	4.3	T	1.125-1.112	1
DJ04	2348	1.570	283.047	1.518	283.096	9/11	AF + Th	189.6	-16.7	333.1	3.0	-78.2	156.3	1.8	R	1.097-0.878	1
DJ05	3120	1.530	283.076	1.471	283.131	9/14	AF + Th	148.3	-7.2	95.4	5.6	-58.2	17.6	4.2	R	1.125-1.112	1
DJ06	3027	1.532	283.078	1.473	283.133	7/12	AF	119.0	-8.3	44.2	10.0	-29.0	17.1	4.8	T	1.125-1.112	1
DJ07	2557	1.571	283.075	1.519	283.124	10/16	Th	355.8	-15.3	153.7	4.1	79.8	126.8	3.2	N	1.097-0.878	1
DJ08	2541	1.574	283.040	1.522	283.089	10/11	AF	347.7	-6.3	185.4	3.8	76.9	172.2	2.2	N	1.097-0878	1
DJ09	2287	1.478	282.997	1.484	283.003	0/5	AF	-	-	-	-	-	-	-	-	0.00321-000303	1
DJ12	2482	1.479	283.015	1.467	283.034	0/5	AF	-	-	-	-	-	-	-	-	0.312 ± 0.029	1
DJ13	2809	1.465	283.035	1.407	283.089	7/11	AF + Th	358.3	-6.1	52.0	9.2	85.2	123.8	8.3	N	1.097 ± 0.039	1
DJ14	1404	1.461	282.959	1.401	283.014	0/5	AF	-	-	-	-	-	-	-	-	~1.125	1
DJ15	2757	1.505	283.020	1.507	283.029	11/16	AF + Th	344.8	-1.9	92.7	5.0	74.6	183.9	4.6	N	0.0804 ± 0.0019	1
GA01	2405	1.131	282.574	1.098	282.609	13/14	AF + Th	344.8	7.2	76.2	5.0	74.6	202.4	4.1	N	0.793-0560	2
GA02	2230	1.144	282.561	1.141	282.574	12/16	AF + Th	2.0	2.2	139.2	3.9	88.0	13.9	3.1	N	0.166 ± 0.034	2
GA03	2238	1.145	282.561	1.142	282.574	13/16	AF + Th	356.2	-8.4	319.2	2.4	83.4	137.8	1.9	N	0.166 ± 0.034	2
GA04	2047	1.153	282.554	1.104	282.601	7/15	AF	326.1	47.1	50.6	9.3	47.3	235.9	7.0	T	0.793-1.1	2
GA05	1785	1.175	282.551	1.117	282.605	11/16	AF	220.9	-23.0	190.9	3.5	-48.0	175.8	2.6	T	1.1 ± 0.1	2
GA06	1672	1.204	282.547	1.146	282.601	0/7	Th	-	-	-	-	-	-	-	-	1.1 ± 0.1	2
GA07	1678	1.204	282.547	1.146	282.601	12/16	Th	151.2	71.9	71.9	5.3	-27.2	299.6	5.4	T	1.1 ± 0.1	2
GA08	1727	1.241	282.513	1.184	282.567	6/12	AF + Th	219.3	11.4	53.1	10.2	-50.1	203.1	7.9	T	1.1 ± 0.1	2
GA09	1675	1.247	282.508	1.190	282.562	11/14	AF + Th	210.0	81.1	47.4	7.1	-13.1	273.7	11.4	T	1.1 ± 0.1	2
GA10	1769	1.295	282.536	1.237	282.590	5/14	AF + Th	349.1	5.2	52.3	12.0	79.1	199.9	9.2	N	1.1 ± 0.1	2
GA11	1872	1.297	282.547	1.264	282.582	13/16	AF + Th	339.6	-10.0	104.8	4.2	68.7	175.2	2.1	N	0-793-0.560	2
GA12	1930	1.290	282.550	1.257	282.585	12/15	Th	339.0	-5.2	261.2	2.8	68.7	182.1	1.0	N	0-793-0.560	2
GA13	1972	1.288	282.550	1.255	282.585	7/12	AF + Th	5.4	20.0	72.1	7.8	79.5	312.0	5.4	N	0-793-0.560	2
GA14	2209	1.284	282.568	1.251	282.603	6/11	AF + Th	345.4	-7.6	108.1	7.1	74.6	173.3	5.8	N	0-793-0.560	2
GA15	2317	1.287	282.579	1.254	282.614	11/14	AF + Th	7.3	-12.0	195.1	3.4	79.7	58.1	2.2	N	0-793-0.560	2
GA16	2246	1.286	285.587	1.287	282.597	12/14	AF + Th	8.8	5.8	80.8	5.1	81.1	1.9	3.1	N	0.159-0.031	2
GA17	2647	1.243	282.678	1.244	282.688	11/12	AF + Th	183.0	20.8	155.1	3.9	-77.6	268.6	3.1	R	0.159-0.031	2
GA18	2639	1.245	282.679	1.246	282.689	14/14	AF + Th	191.9	18.1	100.2	4.2	-74.1	234.6	3.0	R	0.159-0.031	2
GA19	2640	1.246	282.678	1.247	282.688	14/16	AF + Th	169.2	-10.6	122.5	3.7	-78.5	33.8	2.2	R	0.159-0.031	2
GA20	2585	1.248	282.687	1.254	282.693	6/12	AF + Th	320.8	-1.1	163.0	5.8	50.8	190.3	2.8	N	0.012 ± 0.0015	2
GA21	2608	1.243	282.688	1.249	282.694	10/15	AF + Th	15.2	-2.1	60.3	6.6	74.6	21.3	5.0	N	0.012 ± 0.0015	2

Table 4.1. (continued)

Site	Altitude (m)	Slat (°N)	Slon (°E)	Slat* (°N)	Slon* (°E)	n/N	Desmag	Dec (°)	Inc (°)	k	α_{95} (°)	Vlat (°N)	Vlon (°N)	A_{95} (°)	Pol	Age (Ma)	Ref
GA22	3282	1.211	282.669	1.212	282.679	11/14	AF + Th	354.9	-19.7	82.2	5.3	77.5	126.6	2.8	N	0.159-0.031	2
GA23	3250	1.215	282.670	1.216	282.680	8/16	AF + Th	211.7	-17.3	71.1	7.1	-57.6	178.0	4.2	T	0.159-0.031	2
GA24	3211	1.217	282.672	1.223	282.678	12/20	AF + Th	334.7	-3.0	243.2	2.9	64.5	186.6	2.1	N	0.012 ± 0.0015	2
GA25	3132	1.224	282.672	1.230	282.678	10/14	AF + Th	330.5	-8.1	127.7	4.5	60.0	182.3	3.2	N	0.012 ± 0.0015	2
GA26	2472	1.251	282.688	1.252	282.698	13/15	AF + Th	340.8	1.1	88.0	4.6	70.8	191.0	2.8	N	0.159-0.031	2
MOR01	2547	1.236	282.708	1.139	282.791	8/13	AF	182.8	-8.1	73.0	7.0	-86.0	145.2	5.5	R	1.95-1.60	3
MOR02	2636	1.240	282.705	1.143	282.788	10/15	AF	161.6	43.6	66.6	6.3	-58.0	314.7	6.2	R	1.95-1.60	3
MOR03	2847	1.279	282.751	1.182	282.834	18/24	AF + Th	178.1	3.5	124.2	3.2	-86.5	315.9	2.5	R	1.95-1.60	3
MOR04	2749	1.295	282.772	1.183	282.866	9/19	AF	169.8	-2.5	50.1	7.8	-79.9	13.3	4.5	R	2.015 ± 0.268	3
MOR05	2808	1.239	282.739	1.128	282.833	9/14	AF	342.2	5.9	72.1	6.5	72.1	199.0	5.0	N	2.015 ± 0.268	3

Note. Site is the site name (DJ = Doña Juana Volcano; MOR = Morasurco Volcano; GA = Galeras Volcano); Slat and Slon are the latitude and longitude of the paleomagnetic site; Slat* and Slon* correspond to the site paleolatitude and paleolongitude determined using the NNR-MORVEL56 plate motion model (Argus et al., 2011); n is the number of specimens used to calculate site-mean directions (see Table S1); N is the total number of specimens processed for each site; Demag refers to the demagnetization method used: thermal (Th) or alternating field (AF) demagnetization; Dec and Inc are mean site declination and inclination, respectively; k is the parameter precision of directions approximated (Banerjee et al., 2005); α_{95} is the 95% confidence cone around the site-mean direction; Vlat and Vlon are the latitude and longitude of the virtual geomagnetic poles (VGPs) calculated from site paleolocations; A_{95} is the 95% confidence cone around the site-mean VGP. Pol is the geomagnetic polarity: normal (N), reversed (R), and transitional (T) directions; age represents the age interval assigned to each site based on geochronological studies; Ref denotes Reference ID: 1. Pardo et al. (2019); 2. Calvache et al. (1997); 3. Trujillo et al. (2010).

includes uncertainty propagation (Heslop & Roberts, 2020). This result is statistically distinguishable at the 95% confidence level with the predicted direction for a GAD field (D_{GAD} = 0°, I_{GAD} = 2.54°) at the mean latitude (1.27 °N) of the sampling region (Table 4.2 and Figure 4.5a).

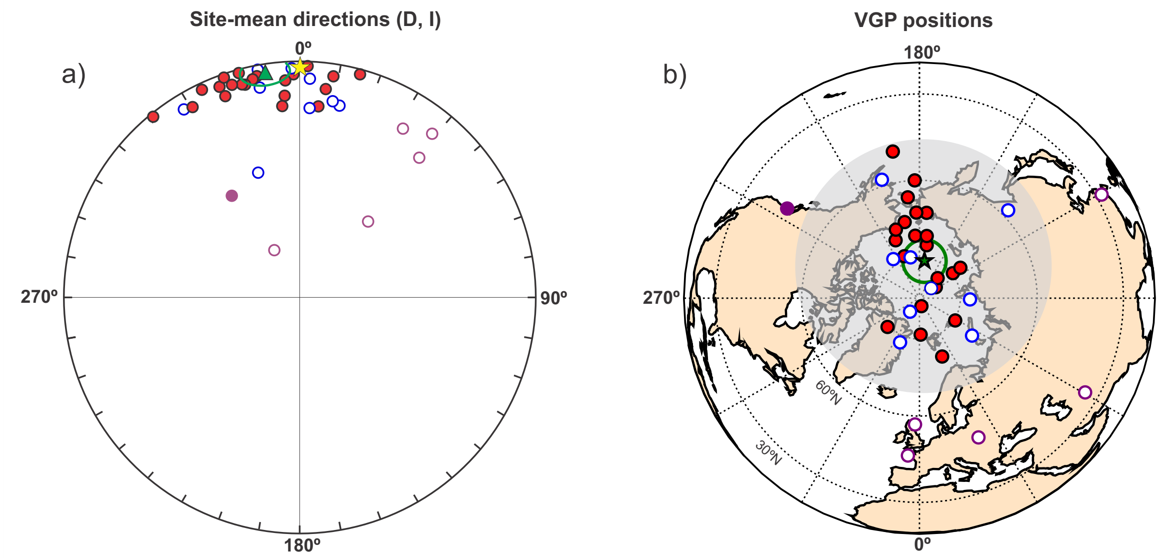

Figure 4.5 – Equal area projection of site-mean directions for the filtered dataset (N = 30 sites). (a) Filled red (open blue) circles represent normal (antipodes of reversed) polarity directions. Green triangle represents the mean direction with its 95% confidence circle (green circle). The yellow star is the expected GAD direction. Purple circles indicate transitional data based on the Vandamme (1994) criterion and were not used for PSV and TAF analysis. (b) Polar stereographic map of VGP positions. Closed (open) circles correspond to normal (reversed) polarity site VGPs projected onto the Northern Hemisphere. The green star indicates the paleopole position with its 95% confidence circle (green circle). Data for transitional sites (purple circles) that were removed after applying the Vandamme (1994) cutoff (32.6°) are outside the transparent grey circle. GAD = geocentric axial dipole; VGP = virtual geomagnetic pole.

VGPs were calculated from the paleolocations and mean directions for all sites (Table 4.1). Site paleolocations were determined using the NNR-MORVEL 56 plate motion model (Argus et al., 2011) to correct for plate tectonic movements. The paleomagnetic pole was calculated from the filtered dataset by averaging the site-level VGPs, considering the antipodes of the reversed polarity sites and VGP uncertainties. Our mean paleomagnetic pole (latitude = 80.7°N, longitude = 173.1°E, A_{95} = 5.2°) does not coincide at the 95% confidence interval with Earth's spin axis (Table 4.2). The VGP positions and the paleopole are shown in the polar projection map in Figure 4.5b.

Table 4.2 – Statistical results of the mean paleodirection for the two age groups.

Age (Ma)	Slat (°N)	Slon (°E)	N	D (°)	I (°)	k	α_{95} (°)	ΔI (°)	Plat (°N)	Plon (°E)	K	A_{95} (°)	S_B (°)	S_{Bl} (°)	S_B^u (°)
0-2.02	1.27	282.76	30	351.2	-3.4	20.0	6.2	-5.9	80.7	173.1	29.1	5.2	15.2	12.0	17.6
Brunhes	1.24	282.65	16	349.3	-2.8	22.2	8.4	-5.3	79.0	178.8	27.4	7.5	16.0	11.6	19.1

Note. Age is age interval of site groups; Slat and Slon are the mean site latitude and longitude; N is the number of sites; D and I are mean declination and inclination; k and α_{95} indicates the parameter precision approximated (Banerjee et al., 2005) and 95% confidence cone about the mean direction; ΔI is inclination anomaly estimate; Plat and Plon are the latitude and longitude of the mean VGP; K and A_{95} indicate the parameter precisiona pproximated (Banerjee et al., 2005) and 95% confidence cone about the mean VGP; S_B is the between-site VGP dispersion; S_{Bl} and S_B^u are the lower and upper 95% confidence limits of S_B.

4.1.6 Discussion

4.1.6.1 Magnetic polarity of the sampled sites

Based on geochronological studies in the studied area (e.g., Calvache et al., 1997; Pardo et al., 2019; Trujillo et al., 2010), the entire dataset (including excursional sites) covers an age interval of 0-2 Ma, and spans the Brunhes (0-0.78 Ma) and Matuyama (0.78-2.58 Ma) chrons. Information about ages with references for the studied paleomagnetic sites are presented in Table 4.1. Considering the age range assigned to each site (and age uncertainties), the magnetic polarity of the paleodirectional sites is approximately consistent with the expected polarity of the geomagnetic polarity time scale 2020 (GPTS2020; Ogg, 2020), as shown in Figure 4.6. Four sites (GA17, GA18, GA19, and GA23) for the 159-31 ka age interval record reversed polarity (maybe induced by a self-reversed TRM) within the Brunhes normal chron. These sites probably record one of several young short-lived reversed polarity events (Laj & Channell, 2015), such as the Mono Lake (33 ka), Laschamp (41 ka), or Blake (120 ka) excursions. Moreover, our dataset spans at least six paleomagnetic reversals, which represents a period long enough (~2 Ma) to record and average paleosecular variation.

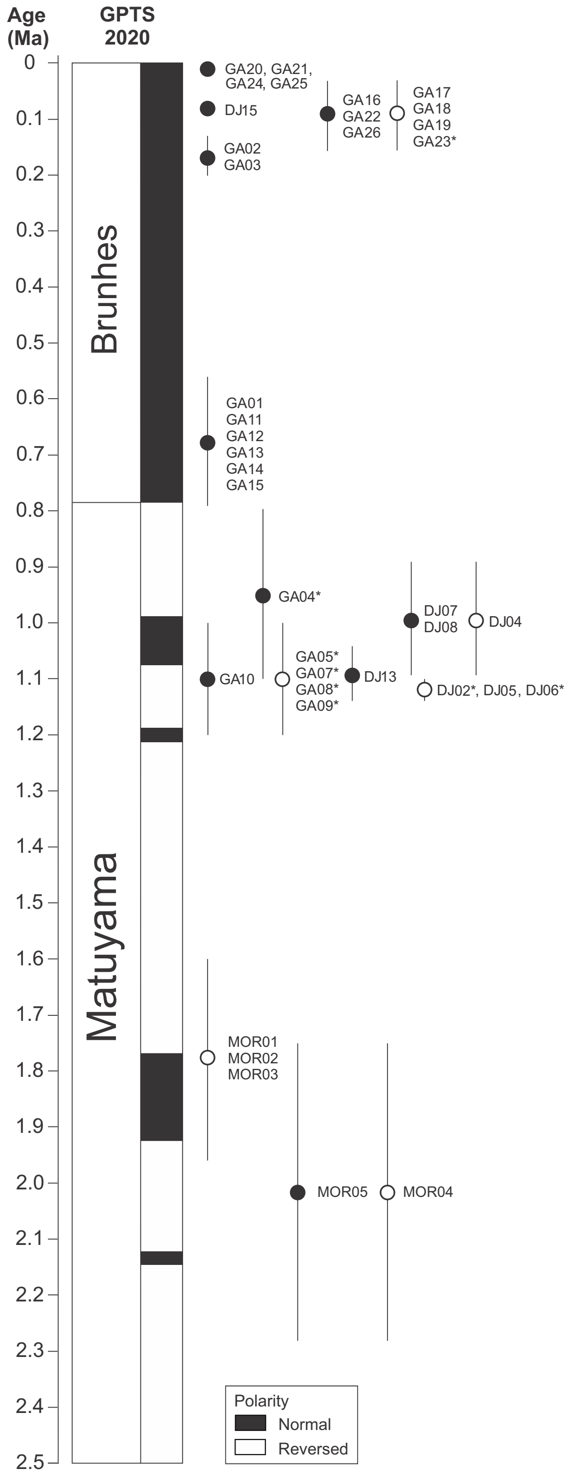

Figure 4.6 – Magnetic polarity of the paleomagnetic sites from this study compared to the geomagnetic polarity time scale 2020 (GPTS2020) of Ogg (2020). Black (white) circles denote normal (reversed) polarity. The age range attributed to the studied sites is represented by a vertical line supported by geochronological studies (see Table 4.1). *Transitional sites identified using the Vandamme (1994) criterion.

4.1.6.2 VGP dispersion estimates

To evaluate geomagnetic paleosecular variation in the study region, the angular dispersion of VGP distributions relative to the mean paleopole was calculated as the between-site dispersion (S_B) that removes random errors associated with within-site VGP dispersion (S_w), expressed by (Biggin et al., 2008b):

$$S_B = \sqrt{\frac{1}{N-1}\sum_{i=1}^{N}\left(\Delta_i^2 - \frac{S_{wi}^2}{n_i}\right)}, \tag{4.1}$$

where N is the total number of sites, and Δ_i corresponds to the angular distance between the ith VGP and the paleomagnetic pole. The within-site dispersion is given by:

$$S_{wi} = \frac{81}{\sqrt{K_i}}, \tag{4.2}$$

where K_i is the Fisher precision parameter for each VGP determined from direction space (k_i) and the site paleolatitude (λ_i), following Cox (1970):

$$K_i = \frac{8k_i}{5 + 18\sin^2\lambda_i + 9\sin^4\lambda_i}. \tag{4.3}$$

From the filtered dataset, we calculated the dispersion S_B and the 95% bootstrap confidence limits (Efron & Tibshirani, 1993) for the 0-2 Ma age interval and Brunhes normal polarity data (Table 4.2). The Matuyama reversed chron was not considered here due to the small data quantity (N = 6 sites), which is unlikely to produce an adequate PSV estimate (Biggin et al., 2008b; Johnson et al., 2008). The VGP dispersion estimated $S_{B(2Ma)} = 15.2_{12.0}^{17.6^\circ}$ (with lower (S_{Bl}) and upper (S_B^u) 95% confidence limits) for the 0-2 Ma period is statistically compatible to the Brunhes chron data with $S_{B(Bru)} = 16.0_{11.6}^{19.1^\circ}$ (16 sites). These estimates are compared to the latitudinal distribution of global S_B data (grey circles), along with PSV models (Model G of McFadden et al. (1988)) proposed by de Oliveira et al. (2021) for the 0-10 Ma and Brunhes intervals (Figures 4.7a and b, respectively). We use the PSV models based on the upgraded 0-10 Ma database with the Vandamme (1994) criterion applied (de Oliveira et al., 2021). As shown in Figure 4.7a-b, $S_{B(2Ma)}$ and $S_{B(Bru)}$ estimates presented here (red squares) have higher values relative to the 0-10 Ma (7 studies) and Brunhes (4 studies) data within the -10° to 10° latitudinal range. However, these estimates are not significantly different at the 95% confidence intervals from the results of most other PSV studies (see Table 4.3). Additionally, our results coincide with VGP dispersion values predicted by Model G ($S_B = 12.4_{10.9}^{13.7^\circ}$ for 0-10 Ma period and $S_B = 11.2_{9.5}^{13.0^\circ}$ for Brunhes interval) within the 95% uncertainty limits (brown dashed curve).

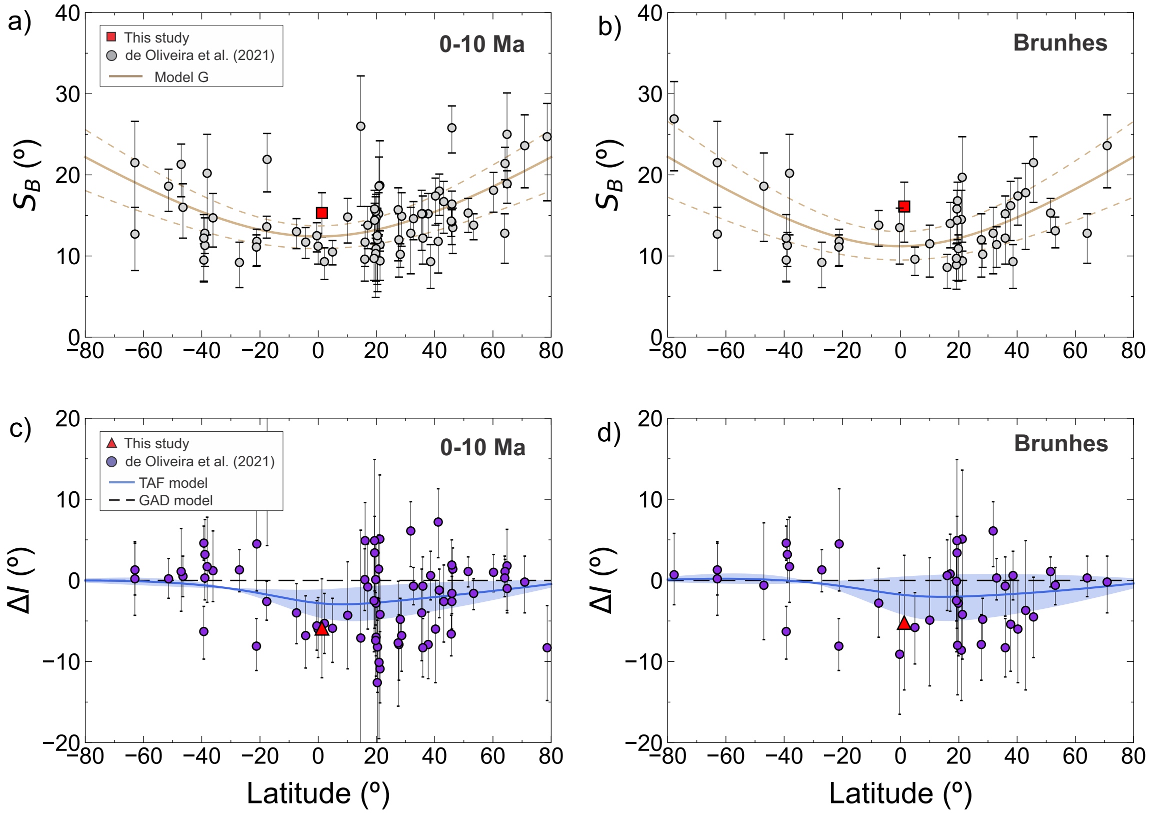

Figure 4.7 – VGP angular dispersion (S_B) as a function of latitude from this study for the 0-2 Ma period and Brunhes chron with their 95% bootstrap confidence limits in (a) and (b), respectively, compared to global S_B data (grey circles) for the 0-10 Ma and the Brunhes intervals (de Oliveira et al., 2021). Brown lines correspond to Model G curves (McFadden et al., 1988) associated with 95% confidence intervals (brown dashed lines). (c-d) Comparison between inclination anomaly (ΔI) estimates from this study (red triangles) with ΔI data compilations for the last 10 Myr and Brunhes chron (purple circles) in (c) and (d), respectively. Blue curves represent the TAF models (de Oliveira et al., 2021), where blue-shaded areas denote the 95% confidence region. VGP = virtual geomagnetic pole; TAF = time-averaged field.

The high VGP dispersion documented here for the study area may be linked to the enhanced longitudinal variability of the magnetic equator in the Atlantic sector (30° to 90°W). In this region, a higher level of PSV activity has been detected compared to the Pacific sector from present-day, centennial (Panovska & Constable, 2017), and millennial scale geomagnetic field models (Constable et al., 2016; Panovska et al., 2019) and in numerical geodynamo models (Aubert et al., 2013; Terra-Nova et al., 2019). The strongest magnetic equator fluctuations in the Atlantic region could be caused by the South Atlantic Anomaly (SAA), which is a zone of weak field intensity located between southern Africa and South America (e.g., Hartmann & Pacca, 2009), large westward declination, and complex spatial inclination behavior (Rother et al., 2021). Some studies (e.g., Engbers et al., 2020; Tarduno et al., 2015) suggest the longevity of this feature over million-year timescales. It seems possible that the high VGP scatter found in Southern Colombia is due to paleomagnetic field direction changes near the magnetic equator. There is only other one dataset for latitude 0.5°S (Opdyke et al., 2006) with $S_B = 12.5_{10.5}^{14.5^{\circ}}$ from the 0-10 Ma database (Table 4.3). Therefore, further investigations are needed in the South American equatorial region to address paleomagnetic data scarcity in this area.

Table 4.3 – Selected paleomagnetic studies from -10° to 10° latitude.

Age (Ma)	Slat (°N)	Slon (°E)	Location	N	D (°)	I (°)	α_{95}	S_B (°)	S_{Bl} (°)	S_B^u (°)	ΔI (°)	ΔI_{lo} (°)	ΔI^{up} (°)	Ref
0-10 Ma interval														
0.005-2.11	10.12	275.48	Costa Rica	29	1.0	15.4	7.1	14.8	11.6	17.1	-4.3	-10.9	2.3	1
0-2.65	4.90	284.64	Colombia	42	3.9	3.8	4.3	10.5	8.9	11.9	-5.9	-10.1	-2.2	2
3.53-4.84	2.13	35.77	Kenya	31	1.1	-1.0	4.2	9.3	7.1	11.0	-5.3	-9.0	-1.6	3
0.5-5.5	-0.04	6.23	Sao Tome	38	358.0	-6.1	4.3	11.2	9.0	12.8	-6.0	-9.5	-2.1	4
0.0176-2.71	-0.48	281.76	Ecuador	45	0.6	-6.6	4.0	12.5	10.5	14.1	-5.6	-8.6	-2.5	5
2.55-10.0	-4.32	327.74	Brazil	36	358.9	-15.4	4.8	11.7	9.7	13.5	-6.8	-10.8	-1.9	6
0-6.7	-7.46	111.94	Indonesia	44	359.9	-18.7	4.4	13.0	10.9	14.6	-4.0	-7.8	-0.4	7
Brunhes chron														
0.01-0.50	10.00	275.81	Costa Rica	12	355.9	14.6	9.4	11.5	7.4	13.8	-4.9	-13.0	2.8	1
0-0.50	4.91	284.64	Colombia	29	4.1	4.0	4.6	9.6	7.6	11.1	-5.8	-10.3	-1.5	2
0.02-0.45	-0.31	281.79	Ecuador	11	356.4	-9.7	10.0	13.5	9.0	15.9	-9.1	-16.5	-1.5	5
0-0.55	-7.52	112.44	Indonesia	36	0.2	-17.6	5.2	13.8	11.2	15.6	-2.8	-7.0	1.5	7

Note. Abbreviations for columns Age to ΔI are as in Table 4.2. ΔI_{lo} and ΔI^{up} are the lower and upper 95% confidence limits of the inclination anomaly. References: 1. Cromwell et al. (2013b); 2. Sánchez-Duque et al. (2016); 3. Opdyke et al. (2010); 4. Opdyke et al. (2015); 5. Opdyke et al. (2006); 6. Leonhardt et al. (2003); 7. Elmaleh et al. (2004).

4.1.6.3 Time-averaged inclination anomalies

A statistical approach usually employed to describe directional deviations from a GAD field refers to the inclination anomaly (ΔI), which is defined as the difference between observed inclination (I_{OBS}) and the GAD inclination according to the Equation (2.20).

Using Equation (2.20), an inclination anomaly for two age groups (0-2 Ma and Brunhes chron datasets) was calculated from the mean inclination (R. A. Fisher, 1953) minus the expected GAD inclination (I_{GAD}). The latter is determined as a function of the mean latitude (λ) for site groups, by using the Equation (3.5).

Accordingly, inclination anomaly estimates are $\Delta I_{2Ma} = -5.9_{-12.1}^{0.3^{\circ}}$ for the 0-2.0 Ma interval and $\Delta I_{Bru} = -5.3_{-13.7}^{3.1^{\circ}}$ for the Brunhes normal polarity chron. These values are statistically indistinguishable from one other and from the GAD field model ($\Delta I = 0°$) within 95% confidence limits (Table 4.2). For comparative purposes, the corresponding estimates are shown in Figures 4.7c and d, together with global ΔI data as a function of latitude (excluding site-level directions using the Vandamme (1994) cutoff method) with respect to zonal TAF model of de Oliveira et al. (2021) over the 0-10 Ma and Brunhes chron periods. These models indicate the presence of minor non-dipole field components that are defined by axial quadrupole contributions of 3.2% and 2.0% (for the 0-10 Ma and Brunhes intervals, respectively) relative to the axial dipole term, with smaller axial octupole contributions of about 1.2%. As can be seen in Figure 4.7c-d, our inclination anomaly data (red triangles) are statistically compatible with paleomagnetic studies located along the -10° to 10° latitude band (Table 4.3) and predictions of TAF models within 95% confidence regions (blue shaded areas). Thus, the negative inclination anomalies observed at equatorial latitudes (including ours) are consistent with zonal TAF models described by low axial quadrupole and octupole components that persist over time.

4.1.7 Conclusions

We present new paleomagnetic records for Late Pleistocene-Holocene volcanic rocks from southern Colombia. Rock magnetic measurements suggest that magnetite and low-Ti titanomagnetite are the main magnetic carriers with Curie temperatures between 516 and 580 °C. However, thermomagnetic curves also reveal the presence of two magnetic phases and suggest titanomaghemite grains with transitional temperatures between 334 and 433 °C. Magnetic domain structures are compatible with vortex state and multidomain grains.

After applying laboratory procedures and data selection criteria, we obtain high-quality paleodirectional results from 30 sites for the 0-2 Ma age interval for statistical PSV and TAF analyses. The mean direction (Dec = 351.2°, Inc = -3.4°, α_{95} = 6.2°, k = 20.0) for these sites does not coincide at the 95% confidence level with directions expected for a GAD field. Similarly, the mean paleomagnetic pole (Plat = 80.7°N, Plon = 173.1°E, A_{95} = 5.2°, K = 29.1) is statistically different from Earth's spin axis. The VGP dispersion for the 0-2 Ma interval ($S_{B(2Ma)} = 15.2_{12.0}^{17.6^{\circ}}$) and Brunhes chron normal polarity data ($S_{B(Bru)} = 16.0_{11.6}^{19.1^{\circ}}$) are statistically compatible within 95% confidence limits with studies at low latitudes and with the predictions of revised PSV models (Model G) for the 0-10 Ma and Brunhes intervals. The high observed VGP scatter in southern Colombia may be associated with anomalous paleodirectional variability over the equatorial Atlantic region influenced by the South Atlantic Magnetic Anomaly that appears to persist on timescales from centuries to millions of years.

Further study is needed to test this hypothesis. Inclination anomalies for each age group ($\Delta I_{2Ma} = -5.9^{0.3^{\circ}}_{-12.1}$ for the 0-2.0 Ma period and $\Delta I_{Bru} = -5.3^{3.1^{\circ}}_{-13.7}$ for the Brunhes chron) support large negative inclination anomalies observed in global compilations and TAF models with low zonal quadrupole (~3%) and octupole (~1%) contributions superimposed on the axial dipole component. Therefore, our new paleomagnetic results from southern Colombia expand the 0-10 Ma database at equatorial latitudes, with the potential to be used for further investigations of paleomagnetic field structure.

Acknowledgments

The authors thank Cor Langereis and Andrew Roberts for reviews and suggestions, and the editorial work of Dominique Jault. This work was supported by grants from the Conselho Nacional de Desenvolvimento Científico e Tecnológico (CNPq, #165161/2018-3, #425728/2018-8, #312737/2020-3), and was (partially) performed at the USPMag laboratory at the Instituto de Astronomia, Geofísica e Ciências Atmosféricas (IAG) at Universidade de São Paulo (USP) funded by CAPES/FAPESP/CNPq.

5. CONCLUDING REMARKS

This thesis presents an updated volcanic database over the past 10 million years from selected paleomagnetic studies applying stringent quality criteria that supersedes previous compilations in the spatial and temporal coverage of paleodirectional data (Chapter 3). The database was used in the development of new PSV and TAF models for the 0-10 Ma interval and the Matuyama and Brunhes chrons. For each time interval, three VGP cutoff approaches were applied. Statistical PSV analysis from the 0-10 Ma data reveals a lower latitudinal dependence of VGP dispersion curve adapted to Model G, which differs from the PSV10 dataset due to the incorporation of new data and analytical approaches employed in this work. In this period, zonal TAF models indicate the presence of zonal non-dipole contributions with axial quadrupole term, $g_2^0 \approx 3.2\%$ of the axial dipole term (g_1^0) and a small axial octupole contribution ($g_3^0 \approx 1.2\%$ of g_1^0). The dominant term g_2^0 is a persistent feature that has been observed in geomagnetic field models for the 0-5 Ma and 0-100 ka intervals.

Assessments of latitudinal behavior in both PSV and the TAF reveal differences between the Matuyama and Brunhes chrons. The Matuyama data show a higher VGP dispersion at low latitudes, with higher a parameter for Model G when compared to Brunhes chron. Regarding TAF models, the contributions of zonal quadrupole and octupole terms to the Matuyama chron are higher than the Brunhes, in particular for ΔI data filtered with the Vandamme criterion, consistent with observations of a lower average dipole moment during this period. These findings provide additional evidence for an anticorrelation between equatorial VGP dispersion and axial dipole dominance, as suggested by recent predictions of numerical geodynamo simulations. Moreover, S_B patterns in interhemispheric coverage indicate an apparent equatorial PSV asymmetry for the Brunhes chron, with a stronger latitudinal variation of S_B in the southern hemisphere than the northern hemisphere. This study suggests that north-south asymmetries of the geomagnetic field, that has been detected in modern, centennial and millennial scale field models, has persisted for the past 780 ka. Further analysis of the historical evolution of VGP dispersions using the COV.OBS field model (covering epochs 1840-2015), as measured by interhemispheric variance, point out that hemispheric asymmetry of dispersions increases gradually with time, attributed to the decline of the geomagnetic dipole and increased non-dipole field contributions.

Another relevant contribution mentioned in this thesis is the new paleodirectional data obtained from lava flow samples collected in three stratovolcanoes (Doña Juana, Galeras, and Morasurco volcanoes) younger than 2 Ma, situated in southwestern Colombia (Chapter 4). Furthermore, fragments of these samples allowed a detailed study of magnetic mineralogy, which indicate the predominance of low coercivity minerals typical of magnetite and low-Ti titanomagnetite. Successful paleodirectional results from 38 sites were determined using modern laboratory methods (thermal and alternating field demagnetization procedures) and that satisfy the strict selection criteria used here. These new results extent the paleomagnetic database over the last 10 Myr, in particular for the poorly populated region of equatorial South America. After removing outlier data by applying the Vandamme criterion, 30 high-quality directional sites were used for statistical analysis of paleomagmetic field. PSV estimates for the 0-2 Ma and Brunhes datasets show a higher VGP dispersion (>15°) in southern Colombia, but these are not statistically distinguishable from paleomagnetic studies at low latitudes. The high VGP scatter may be related to large longitudinal fluctuations of the magnetic equator over equatorial Atlantic and South America, and the influence of the South Atlantic Magnetic Anomaly that persists over different timescales. Further work is required to confirm this hypothesis due to paucity of paleodirectional data at low latitudes. The reliable ΔI estimates for two age groups reveal high negative values (>-5°) with large deviations from a GAD model. These high estimates are consistent with the new TAF models presented here, which support the presence of non-GAD field structures.

All investigations accomplished in this thesis have provided important insights into the long-term geomagnetic variations and constraints on numerical geodynamo models. Despite the results and new improvements on PSV and TAF knowledges, as well as the new data from Equatorial region, there is a clear need to improve the spatial and temporal data coverage. The acquisition of new paleomagnetic data will be essential to expand and upgrade the 0-10 Ma database, and improve the knowledge of long-period geomagnetic field variability. In particular, to understand the geometry and longevity of the main geomagnetic field feature, the South Atlantic Magnetic Anomaly over million of years timescales.

REFERENCES

Ahn, H. S., & Yamamoto, Y. (2019). Paleomagnetic study of basaltic rocks from Baengnyeong Island, Korea: Efficiency of the Tsunakawa–Shaw paleointensity determination on non-SD-bearing materials and implication for the early Pliocene geomagnetic field intensity. *Earth, Planets and Space*, *71*(1), 1–20.

Aldana, M., Costanzo-Álvarez, V., Gómez, L., González, C., Díaz, M., Silva, P., & Rada, M. (2011). Identification of magnetic minerals related to hydrocarbon authigenesis in Venezuelan oil fields using an alternative decomposition of isothermal remanence curves. *Studia Geophysica et Geodaetica*, *55*(2), 343–358.

Alva-Valdivia, L. M. (2005). Comprehensive paleomagnetic study of a succession of Holocene olivine-basalt flow: Xitle Volcano (Mexico) revisited. *Earth, Planets and Space*, *57*(9), 839–853.

Amit, H., Choblet, G., Olson, P., Monteux, J., Deschamps, F., Langlais, B., & Tobie, G. (2015). Towards more realistic core-mantle boundary heat flux patterns: A source of diversity in planetary dynamos. *Progress in Earth and Planetary Science*, *2*(1), 1–26.

Amit, H., Terra-Nova, F., Lézin, M., & Trindade, R. I. (2021). Non-monotonic growth and motion of the South Atlantic Anomaly. *Earth, Planets and Space*, *73*(1), 1–10.

Argus, D. F., Gordon, R. G., & DeMets, C. (2011). Geologically current motion of 56 plates relative to the no-net-rotation reference frame. *Geochemistry, Geophysics, Geosystems*, *12*(11).

Aster, R. C., Borchers, B., & Thurber, C. H. (2012). *Parameter estimation and inverse problems*. Elsevier.

Aubert, J., Finlay, C. C., & Fournier, A. (2013). Bottom-up control of geomagnetic secular variation by the Earth's inner core. *Nature*, *502*(7470), 219–223.

Aubert, J., Tarduno, J. A., & Johnson, C. L. (2010). Observations and models of the long-term evolution of Earth's magnetic field. *Space Science Reviews*, *155*(1-4), 337–370.

Baag, C.-G., & Helsley, C. E. (1974). Geomagnetic Secular Variation Model E. *Journal of Geophysical Research*, *79*(32), 4918–4922.

Banerjee, A., Dhillon, I. S., Ghosh, J., Sra, S., & Ridgeway, G. (2005). Clustering on the unit hypersphere using von mises-fisher distributions. *Journal of Machine Learning Research*, *6*(9).

Baraldo, A., Rapalini, A. E., Böhnel, H., & Mena, M. (2003). Paleomagnetic study of Deception Island, South Shetland Islands, Antarctica. *Geophysical Journal International*, *153*(2), 333–343.

Bayona, G. (1994). La Formación Saldaña: Producto de la actividad de estratovolcanes continentales en un dominio de retroarco. *Estudios geológicos del valle superior del Magdalena*.

Bayona, G., Bustamante, C., Nova, G., & Salazar Franco, A. M. (2020). Jurassic evolution of the northwestern corner of Gondwana: Present knowledge and future challenges in studying Colombian Jurassic rocks.

Behar, N., Shaar, R., Tauxe, L., Asefaw, H., Ebert, Y., Heimann, A., Koppers, A. A. P., & Ron, H. (2019). Paleomagnetism and paleosecular variations from the Plio-Pleistocene Golan Heights volcanic plateau, Israel. *Geochemistry, Geophysics, Geosystems*, *20*(9), 4319–4335.

Biggin, A. J., Bono, R. K., Meduri, D. G., Sprain, C. J., Davies, C. J., Holme, R., & Doubrovine, P. V. (2020). Quantitative estimates of average geomagnetic axial dipole dominance in deep geological time. *Nature Communications*, *11*(1), 1–9.

Biggin, A. J., Steinberger, B., Aubert, J., Suttie, N., Holme, R., Torsvik, T. H., van der Meer, D. G., & Van Hinsbergen, D. J. J. (2012). Possible links between long-term geomagnetic variations and whole-mantle convection processes. *Nature Geoscience*, *5*(8), 526–533.

Biggin, A. J., Strik, G. H. M. A., & Langereis, C. G. (2009). The intensity of the geomagnetic field in the late-Archaean: New measurements and an analysis of the updated IAGA palaeointensity database. *Earth, Planets and Space*, *61*(1), 9–22.

Biggin, A. J., Strik, G. H. M. A., & Langereis, C. G. (2008a). Evidence for a very-long-term trend in geomagnetic secular variation. *Nature Geoscience*, *1*(6), 395–398.

Biggin, A. J., van Hinsbergen, D. J. J., Langereis, C. G., Straathof, G. B., & Deenen, M. H. L. (2008b). Geomagnetic secular variation in the Cretaceous Normal Superchron and in the Jurassic. *Physics of the Earth and Planetary Interiors*, *169*(1-4), 3–19.

Biggin, A. J., Piispa, E. J., Pesonen, L. J., Holme, R., Paterson, G. A., Veikkolainen, T., & Tauxe, L. (2015). Palaeomagnetic field intensity variations suggest Mesoproterozoic inner-core nucleation. *Nature*, *526*(7572), 245–248.

Bono, R. K., Biggin, A. J., Holme, R., Davies, C. J., Meduri, D. G., & Bestard, J. (2020). Covariant giant Gaussian process models with improved reproduction of Palaeosecular variation. *Geochemistry, Geophysics, Geosystems*, *21*(8).

Brandt, D., Constable, C. G., & Ernesto, M. (2020). Giant Gaussian process models of geomagnetic palaeosecular variation: A directional outlook. *Geophysical Journal International*, *222*(3), 1526–1541.

Brown, L. L., Singer, B. S., & Gorring, M. L. (2004). Paleomagnetism and ^{40}Ar/^{39}Ar chronology of lavas from Meseta del lago Buenos Aires, Patagonia. *Geochemistry, Geophysics, Geosystems*, *5*(1).

Brown, M. C., Holme, R., & Bargery, A. (2007). Exploring the influence of the non-dipole field on magnetic records for field reversals and excursions. *Geophysical Journal International*, *168*(2), 541–550.

Brown, M. C., Singer, B. S., Knudsen, M. F., Jicha, B. R., Finnes, E., & Feinberg, J. M. (2009). No evidence for Brunhes age excursions, Santo Antão, Cape Verde. *Earth and Planetary Science Letters*, *287*(1-2), 100–115.

Buffett, B. A. (2000). Earth's core and the geodynamo. *Science*, *288*(5473), 2007–2012.

Buffett, B. A. (2015). Dipole fluctuations and the duration of geomagnetic polarity transitions. *Geophysical Research Letters*, *42*(18), 7444–7451.

Bustamante, C., Archanjo, C. J., Cardona, A., & Vervoort, J. D. (2016). Late Jurassic to Early Cretaceous plutonism in the Colombian Andes: A record of long-term arc maturity. *Bulletin*, *128*(11-12), 1762–1779.

Butler, R. F. (1998). Paleomagnetism: Magnetic domains to geologic terranes. *Electronic edition*, *23*.

Calvache, M. L., Cortéz, G. P., & Williams, S. N. (1997). Stratigraphy and chronology of the Galeras volcanic complex, Colombia. *Journal of Volcanology and Geothermal Research*, *77*(1-4), 5–19.

Calvache, M. L., & Trujillo, J. F. D. (2016). Geomorphological Features of the Galeras Volcanic Complex. In *Landscapes and Landforms of Colombia* (pp. 193–202). Springer.

Calvo-Rathert, M., Goguitchaichvili, A., & Vegas-Tubia, N. (2009). A paleointensity study on middle Miocene to Pliocene volcanic rocks from south-eastern Spain. *Earth, Planets and Space*, *61*(1), 61–69.

Calvo-Rathert, M., Goguitchaichvili, A., Bógalo, M.-F., Vegas-Tubía, N., Carrancho, Á., & Sologashvili, J. (2011). A paleomagnetic and paleointensity study on Pleistocene and Pliocene basaltic flows from the Djavakheti Highland (Southern Georgia, Caucasus). *Physics of the Earth and Planetary Interiors*, *187*(3-4), 212–224.

Camps, P., Henry, B., Prevot, M., & Faynot, L. (2001). Geomagnetic paleosecular variation recorded in Plio-Pleistocene volcanic rocks from Possession Island (Crozet Archipelago, southern Indian Ocean). *Journal of Geophysical Research: Solid Earth*, *106*(B2), 1961–1971.

Campuzano, S. A., Gómez-Paccard, M., Pavón-Carrasco, F. J., & Osete, M. L. (2019). Emergence and evolution of the South Atlantic Anomaly revealed by the new paleomagnetic reconstruction SHAWQ2k. *Earth and Planetary Science Letters*, *512*, 17–26.

Carlut, J., Quidelleur, X., Courtillot, V., & Boudon, G. (2000). Paleomagnetic directions and K/Ar dating of 0 to 1 Ma lava flows from La Guadeloupe Island (French West Indies): Implications for time-averaged field models. *Journal of Geophysical Research: Solid Earth*, *105*(B1), 835–849.

Carlut, J., & Courtillot, V. (1998). How complex is the time-averaged geomagnetic field over the past 5 Myr? *Geophysical Journal International*, *134*(2), 527–544.

Cediel, F., Mojica, J., & Macía, C. (1981). Las formaciones Luisa, Payandé y Saldaña sus columnas estratigráficas características. *Geología Norandina*, *3*, 11–19.

Ceja, M. R., Goguitchaichvili, A., Calvo-Rathert, M., Morales-Contreras, J., Alva-Valdivia, L., Elguera, J. R., Fucugauchi, J. U., & Granados, H. D. (2006). Paleomagnetism of the

Pleistocene Tequila Volcanic Field (western Mexico). *Earth, Planets and Space*, *58*(10), 1349–1358.

Cepeda, H. (1985). Anotaciones acerca de la geología del volcán Galeras (Colombia). *Memorias del VI Congreso Latinoamericano de geología*, *1*.

Channell, J. E. T., Xuan, C., & Hodell, D. A. (2009). Stacking paleointensity and oxygen isotope data for the last 1.5 Myr (PISO-1500). *Earth and Planetary Science Letters*, *283*(1-4), 14–23.

Chauvin, A., Gillot, P.-Y., & Bonhommet, N. (1991). Paleointensity of the Earth's magnetic field recorded by two late Quaternary volcanic sequences at the island of La Réunion (Indian Ocean). *Journal of Geophysical Research: Solid Earth*, *96*(B2), 1981–2006.

Christensen, U. R., & Olson, P. (2003). Secular variation in numerical geodynamo models with lateral variations of boundary heat flow. *Physics of the Earth and Planetary Interiors*, *138*(1), 39–54.

Christensen, U. R. (2011). Geodynamo models: Tools for understanding properties of Earth's magnetic field. *Physics of the Earth and Planetary Interiors*, *187*(3-4), 157–169.

Clement, B. M. (1991). Geographical distribution of transitional VGPs: Evidence for non-zonal equatorial symmetry during the Matuyama–Brunhes geomagnetic reversal. *Earth and Planetary Science Letters*, *104*(1), 48–58.

Cochrane, R., Spikings, R., Gerdes, A., Ulianov, A., Mora, A., Villagómez, D., Putlitz, B., & Chiaradia, M. (2014). Permo-Triassic anatexis, continental rifting and the disassembly of western Pangaea. *Lithos*, *190*, 383–402.

Coe, R. S., & Glatzmaier, G. A. (2006). Symmetry and stability of the geomagnetic field. *Geophysical Research Letters*, *33*(21).

Coe, R. S., Zhao, X., Lyons, J. J., Pluhar, C. J., & Mankinen, E. A. (2000). Revisiting the 1964 collection of Nunivak lava flows. *Eos, Transactions American Geophysical Union*, *81*(48).

Constable, C. G., & Parker, R. L. (1988). Statistics of the geomagnetic secular variation for the past 5 My. *Journal of Geophysical Research: Solid Earth*, *93*(B10), 11569–11581.

Constable, C. G., & Johnson, C. L. (1999). Anisotropic paleosecular variation models: Implications for geomagnetic field observables. *Physics of the Earth and Planetary Interiors*, *115*(1), 35–51.

Constable, C. G., Korte, M., & Panovska, S. (2016). Persistent high paleosecular variation activity in southern hemisphere for at least 10 000 years. *Earth and Planetary Science Letters*, *453*, 78–86.

Conte-Fasano, G., Urrutia-Fucugauchi, J., Goguitchaichvili, A., & Morales-Contreras, J. (2006). Low-latitude paleosecular variation and the time-averaged field during the late Pliocene and Quaternary—Paleomagnetic study of the Michoacan-Guanajuato volcanic field, Central Mexico. *Earth, Planets and Space*, *58*(10), 1359–1371.

Cormier, V. F., Bergman, M. I., & Olson, P. L. (2022). *Earth's Core*. Academic Press.

Costin, S. O., & Buffett, B. A. (2004). Preferred reversal paths caused by a heterogeneous conducting layer at the base of the mantle. *Journal of Geophysical Research: Solid Earth*, *109*(B6).

Cox, A. (1962). Analysis of present geomagnetic field for comparison with paleomagnetic results. *Journal of Geomagnetism and Geoelectricity*, *13*(3-4), 101–112.

Cox, A. (1970). Latitude dependence of the angular dispersion of the geomagnetic field. *Geophysical Journal International*, *20*(3), 253–269.

Cox, A. (1975). The frequency of geomagnetic reversals and the symmetry of the nondipole field. *Reviews of Geophysics*, *13*(3), 35–51.

Creer, K. M. (1962). The dispersion of the geomagnetic field due to secular variation and its determination for remote times from paleomagnetic data. *Journal of Geophysical Research*, *67*(9), 3461–3476.

Creer, K. M., Irving, E., & Nairn, A. E. M. (1959). Palaeomagnetism of the Great Whin sill. *Geophysical Journal International*, *2*(4), 306–323.

Cromwell, G., Constable, C. G., Staudigel, H., Tauxe, L., & Gans, P. (2013b). Revised and updated paleomagnetic results from Costa Rica. *Geochemistry, Geophysics, Geosystems*, *14*(9), 3379–3388.

Cromwell, G., Johnson, C. L., Tauxe, L., Constable, C. G., & Jarboe, N. A. (2018). PSV10: A global data set for 0–10 Ma time-averaged field and paleosecular variation studies. *Geochemistry, Geophysics, Geosystems*, *19*(5), 1533–1558.

Cromwell, G., Tauxe, L., Staudigel, H., Constable, C. G., Koppers, A. A. P., & Pedersen, R.-B. (2013a). In search of long-term hemispheric asymmetry in the geomagnetic field: Results from high northern latitudes. *Geochemistry, Geophysics, Geosystems*, *14*(8), 3234–3249.

Cromwell, G., Tauxe, L., & Halldórsson, S. (2015). New paleointensity results from rapidly cooled icelandic lavas: Implications for Arctic geomagnetic field strength. *Journal of Geophysical Research: Solid Earth*, *120*(5), 2913–2934.

Davies, C. J., & Constable, C. G. (2014). Insights from geodynamo simulations into long-term geomagnetic field behaviour. *Earth and Planetary Science Letters*, *404*, 238–249.

Davies, C. J., & Constable, C. G. (2020). Rapid geomagnetic changes inferred from Earth observations and numerical simulations. *Nature Communications*, *11*(1), 1–10.

Davies, C. J., Gubbins, D., Willis, A. P., & Jimack, P. K. (2008). Time-averaged paleomagnetic field and secular variation: Predictions from dynamo solutions based on lower mantle seismic tomography. *Physics of the Earth and Planetary Interiors*, *169*(1-4), 194–203.

Day, R., Fuller, M., & Schmidt, V. A. (1977). Hysteresis properties of titanomagnetites: Grain-size and compositional dependence. *Physics of the Earth and Planetary Interiors*, *13*(4), 260–267.

De Koker, N., Steinle-Neumann, G., & Vlček, V. (2012). Electrical resistivity and thermal conductivity of liquid Fe alloys at high P and T, and heat flux in Earth's core. *Proceedings of the National Academy of Sciences*, *109*(11), 4070–4073.

Deb, K., & Kalyanmoy, D. (2001). *Multi-objective optimization using evolutionary algorithms.* John Wiley & Sons.

Deenen, M. H. L., Langereis, C. G., van Hinsbergen, D. J. J., & Biggin, A. J. (2011). Geomagnetic secular variation and the statistics of palaeomagnetic directions. *Geophysical Journal International*, *186*(2), 509–520.

de Oliveira, W. P., Hartmann, G. A., Savian, J. F., Nova, G., Parra, M., Biggin, A. J., & Trindade, R. I. F. (2022). Paleosecular variation record from Pleistocene-Holocene lava flows in southern Colombia. *Physics of the Earth and Planetary Interiors*, *332*.

de Oliveira, W. P., Hartmann, G. A., Terra-Nova, F., Brandt, D., Biggin, A. J., Engbers, Y. A., Bono, R. K., Savian, J. F., Franco, D. R., Trindade, R. I. F., & Moncinhatto, T. R. (2021). Paleosecular variation and the time-averaged geomagnetic field since 10 Ma. *Geochemistry, Geophysics, Geosystems*, *22*(10).

de Oliveira, W. P., Franco, D. R., Brandt, D., Ernesto, M., da Ponte Neto, C. F., Zhao, X., de Freitas, F. B. V., & Martins, R. S. (2018). Behavior of the paleosecular variation during the Permian-Carboniferous Reversed Superchron and comparisons to the low reversal frequency intervals since Precambrian times. *Geochemistry, Geophysics, Geosystems*, *19*(4), 1035–1048.

Di Chiara, A., Speranza, F., Porreca, M., Pimentel, A., D'Ajello Caracciolo, F., & Pacheco, J. (2014). Constraining chronology and time-space evolution of Holocene volcanic activity on the Capelo Peninsula (Faial Island, Azores): The paleomagnetic contribution. *Bulletin*, *126*(9-10), 1164–1180.

Dormy, E., & Le Mouël, J.-L. (2008). Geomagnetism and the dynamo: Where do we stand? *Comptes Rendus Physique*, *9*(7), 711–720.

Dormy, E., Valet, J.-P., & Courtillot, V. (2000). Numerical models of the geodynamo and observational constraints. *Geochemistry, Geophysics, Geosystems*, *1*(10).

Døssing, A., Muxworthy, A. R., Supakulopas, R., Riishuus, M. S., & Mac Niocaill, C. (2016). High northern geomagnetic field behavior and new constraints on the Gilsá event: Paleomagnetic and $^{40}Ar/^{39}Ar$ results of ~0.5–3.1 Ma basalts from Jökuldalur, Iceland. *Earth and Planetary Science Letters*, *456*, 98–111.

Døssing, A., Riishuus, M. S., Mac Niocaill, C., Muxworthy, A. R., & Maclennan, J. (2020). Late Miocene to late Pleistocene geomagnetic secular variation at high northern latitudes. *Geophysical Journal International*, *222*(1), 86–102.

Doubrovine, P. V., Veikkolainen, T., Pesonen, L. J., Piispa, E., Ots, S., Smirnov, A. V., Kulakov, E. V., & Biggin, A. J. (2019). Latitude dependence of geomagnetic paleosecular variation and its relation to the frequency of magnetic reversals: Observations from the Cretaceous and Jurassic. *Geochemistry, Geophysics, Geosystems*, *20*(3), 1240–1279.

Driscoll, P., & Olson, P. (2011). Superchron cycles driven by variable core heat flow. *Geophysical Research Letters*, *38*(9).

Dunlop, D. J., & Özdemir, Ö. (1997). *Rock magnetism: Fundamentals and frontiers*. Cambridge University press.

Efron, B., & Tibshirani, R. J. (1993). *An introduction to the bootstrap*. Chapman & Hall.

Egli, R. (2021). Magnetic characterization of geologic materials with first-order reversal curves. In *Magnetic measurement techniques for materials characterization* (pp. 455–604). Springer.

Elmaleh, A., Valet, J.-P., Quidelleur, X., Solihin, A., Bouquerel, H., Tesson, T., Mulyadi, E., Khokhlov, A., & Wirakusumah, A. D. (2004). Palaeosecular variation in Java and Bawean Islands (Indonesia) during the Brunhes chron. *Geophysical Journal International*, *157*(1), 441–454.

Engbers, Y. A., Biggin, A. J., & Bono, R. K. (2020). Elevated paleomagnetic dispersion at Saint Helena suggests long-lived anomalous behavior in the South Atlantic. *Proceedings of the National Academy of Sciences*, *117*(31), 18258–18263.

Engbers, Y. A., Grappone, J. M., Mark, D. F., & Biggin, A. J. (2022). Low paleointensities and Ar/Ar ages from Saint Helena provide evidence for recurring magnetic field weaknesses in the South Atlantic. *Journal of Geophysical Research: Solid Earth*, *127*(3).

Evans, M. E., & Heller, F. (2003). *Environmental magnetism: Principles and applications of enviromagnetics*. Elsevier.

Finlay, C. C., Kloss, C., Olsen, N., Hammer, M. D., Tøffner-Clausen, L., Grayver, A., & Kuvshinov, A. (2020). The CHAOS-7 geomagnetic field model and observed changes in the South Atlantic Anomaly. *Earth, Planets and Space*, *72*(1), 1–31.

Fisher, N. I., Lewis, T., & Embleton, B. J. J. (1987). *Statistical analysis of spherical data*. Cambridge university press.

Fisher, R. A. (1953). Dispersion on a sphere. *Proceedings of the Royal Society of London. Series A. Mathematical and Physical Sciences*, *217*(1130), 295–305.

Franco, D. R., de Oliveira, W. P., de Freitas, F. B. V., Takahashi, D., da Ponte Neto, C. F., & Peixoto, I. M. C. (2019). Paleomagnetic evidence for inverse correspondence between the relative contribution of the axial dipole field and CMB heat flux for the past 270 Myr. *Scientific Reports*, *9*(1), 1–8.

Garnero, E. J., & McNamara, A. K. (2008). Structure and dynamics of Earth's lower mantle. *Science*, *320*(5876), 626–628.

Gautam, P., Blaha, U., Appel, E., & Neupane, G. (2004). Environmental magnetic approach towards the quantification of pollution in Kathmandu urban area, Nepal. *Physics and Chemistry of the Earth, parts A/B/C*, *29*(13-14), 973–984.

Gillet, N., Barrois, O., & Finlay, C. C. (2015). Stochastic forecasting of the geomagnetic field from the COV-OBS.x1 geomagnetic field model, and candidate models for IGRF-12. *Earth, Planets and Space*, *67*(1), 1–14.

Glatzmaier, G. A. (2002). Geodynamo simulations–How realistic are they? *Annual Review of Earth and Planetary Sciences*, *30*(1), 237–257.

Glatzmaier, G. A., Coe, R. S., Hongre, L., & Roberts, P. H. (1999). The role of the Earth's mantle in controlling the frequency of geomagnetic reversals. *Nature*, *401*(6756), 885–890.

Glatzmaier, G. A., & Olson, P. (2005). Probing the geodynamo. *Scientific American*, *292*(4), 50–57.

Glatzmaier, G. A., & Roberts, P. H. (1995). A three-dimensional convective dynamo solution with rotating and finitely conducting inner core and mantle. *Physics of the Earth and Planetary Interiors*, *91*(1-3), 63–75.

Goguitchaichvili, A., Calvo, M., Sologashvili, D., Alva, L., & Urrutia, J. (2000). Palaeomagnetism of Georgian Plio-Quaternary volcanic provinces (Southern Caucasus): A pilot study. *Comptes Rendus de l'Académie des Sciences-Series IIA - Earth and Planetary Science*, *331*(11), 683–690.

Goguitchaichvili, A., González, J. A., Pluhar, C. J., Alva-Valdivia, L., Rosas Elguera, J., Ruiz-Martínez, V. C., Solé, J., Zhao, X., Coe, R. S., & Caballero, C. (2011). A comprehensive rock-magnetic, paleomagnetic, paleointensity and geochronologic study along the western Trans-Mexican Volcanic Belt: Geodynamic and geomagnetic implications. *Geofísica Internacional*, *50*(2), 227–254.

Goguitchaichvili, A., Petronille, M., Henry, B., Valdivia, L. A., Morales, J., & Urrutia-Fucugauchi, J. (2007). Paleomagnetism of the Eastern Alkaline Province (Mexico): Contribution to the time-averaged field global database and geomagnetic instability time scale. *Earth, Planets and Space*, *59*(7), 775–783.

Goguitchaichvili, A., Valdivia, L. M. A., Elguera, J. R., Fucugauchi, J. U., Cervantes, M. A., & Morales, J. (2002). Paleosecular variation record of geomagnetic full vector during late Miocene, from the Nayarit area, Mexico. *Physics of the Earth and Planetary Interiors*, *134*(1-2), 71–88.

Gonzalez, S., Sherwood, G., Böhnel, H., & Schnepp, E. (1997). Palaeosecular variation in Central Mexico over the last 30000 years: The record from lavas. *Geophysical Journal International*, *130*(1), 201–219.

Gubbins, D., & Kelly, P. (1993). Persistent patterns in the geomagnetic field over the past 2.5 Myr. *Nature*, *365*(6449), 829–832.

Guyodo, Y., Richter, C., & Valet, J.-P. (1999). Paleointensity record from Pleistocene sediments (1.4–0 Ma) off the California Margin. *Journal of Geophysical Research: Solid Earth*, *104*(B10), 22953–22964.

Haag, M., Heller, F., Allenspach, R., & Roche, K. (1990). Self-reversal of natural remanent magnetization in andesitic pumice. *Physics of the Earth and Planetary Interiors*, *65*(1-2), 104–108.

Haldan, M. M., Langereis, C. G., Biggin, A. J., Dekkers, M. J., & Evans, M. E. (2009). A comparison of detailed equatorial red bed records of secular variation during the Permo-Carboniferous Reversed Superchron. *Geophysical Journal International*, *177*(3), 834–848.

Handford, B. T., Biggin, A. J., Haldan, M. M., & Langereis, C. G. (2021). Analyzing Triassic and Permian Geomagnetic Paleosecular Variation and the Implications for Ancient Field Morphology. *Geochemistry, Geophysics, Geosystems*, *22*(11), 1–22.

Harrison, R. J., & Feinberg, J. M. (2008). FORCinel: An improved algorithm for calculating first-order reversal curve distributions using locally weighted regression smoothing. *Geochemistry, Geophysics, Geosystems*, *9*(5).

Hartmann, G. A., & Pacca, I. G. (2009). Time evolution of the South Atlantic magnetic anomaly. *Anais da Academia Brasileira de Ciências*, *81*, 243–255.

Hatakeyama, T., & Kono, M. (2002). Geomagnetic field model for the last 5 My: Time-averaged field and secular variation. *Physics of the Earth and Planetary Interiors*, *133*(1-4), 181–215.

Heller, F., Carracedo, J. C., & Solert, V. (1986). Reversed magnetization in pyroclastics from the 1985 eruption of Nevado del Ruiz, Colombia. *Nature*, *324*(6094), 241–242.

Heller, R., Merrill, R. T., & McFadden, P. L. (2002). The variation of intensity of Earth's magnetic field with time. *Physics of the Earth and Planetary Interiors*, *131*(3-4), 237–249.

Herrero-Bervera, E., & Valet, J.-P. (2002). Paleomagnetic secular variation of the Honolulu Volcanic Series (33–700 ka), O'ahu (Hawaii). *Physics of the Earth and Planetary Interiors*, *133*(1-4), 83–97.

Herrero-Bervera, E., & Valet, J.-P. (2007). Holocene paleosecular variation from dated lava flows on Maui (Hawaii). *Physics of the Earth and Planetary Interiors*, *161*(3-4), 267–280.

Heslop, D., & Roberts, A. P. (2020). Uncertainty propagation in hierarchical paleomagnetic reconstructions. *Journal of Geophysical Research: Solid Earth*, *125*(6).

Hulot, G., Sabaka, T. K., Olsen, N., & Fournier, A. (2015). The present and future geomagnetic field, In G. Schubert (Ed.), *Treatise on Geophysics* (2nd ed., pp. 385–414). Elsevier.

Hulot, G., Finlay, C. C., Constable, C. G., Olsen, N., & Mandea, M. (2010). The Magnetic Field of Planet Earth. *Space Science Reviews*, *152*(1), 159–222.

Hulot, G., & Gallet, Y. (1996). On the interpretation of virtual geomagnetic pole (VGP) scatter curves. *Physics of the Earth and Planetary Interiors*, *95*(1-2), 37–53.

Irving, E. (1964). *Paleomagnetism and Its Application to Geological and Geophysical Problems*. New York: Wiley.

Irving, E., & Ward, M. A. (1964). A statistical model of the geomagnetic field. *Pure and Applied Geophysics*, *57*(1), 47–52.

Jackson, A., & Murray, A. (1997). Past attractions: Historical magnetic observations. *Astronomy & Geophysics*, *38*(6), 10–15.

Jaramillo, J. S., Cardona, A., León, S., Valencia, V., & Vinasco, C. (2017). Geochemistry and geochronology from Cretaceous magmatic and sedimentary rocks at 6º 35'N, western flank of the Central cordillera (Colombian Andes): Magmatic record of arc growth and collision. *Journal of South American Earth Sciences*, *76*, 460–481.

Johnson, C. L., & McFadden, P. L. (2015). The time-averaged field and paleosecular variation. In G. Schubert (Ed.), *Treatise on Geophysics* (2nd ed., pp. 385–414). Elsevier.

Johnson, C. L., & Constable, C. G. (1995). The time-averaged geomagnetic field as recorded by lava flows over the past 5 Myr. *Geophysical Journal International*, *122*(2), 489–519.

Johnson, C. L., & Constable, C. G. (1996). Palaeosecular variation recorded by lava flows over the past five million years. *Philosophical Transactions of the Royal Society of London. Series A: Mathematical, Physical and Engineering Sciences*, *354*(1704), 89–141.

Johnson, C. L., & Constable, C. G. (1997). The time-averaged geomagnetic field: Global and regional biases for 0–5 Ma. *Geophysical Journal International*, *131*(3), 643–666.

Johnson, C. L., Constable, C. G., Tauxe, L., Barendregt, R., Brown, L. L., Coe, R. S., Layer, P., Mejia, V., Opdyke, N. D., Singer, B. S., Staudigel, H., & Stone, D. B. (2008). Recent investigations of the 0–5 Ma geomagnetic field recorded by lava flows. *Geochemistry, Geophysics, Geosystems*, *9*(4).

Johnson, C. L., Wijbrans, J. R., Constable, C. G., Gee, J., Staudigel, H., Tauxe, L., Forjaz, V.-H., & Salgueiro, M. (1998). ^{40}Ar/^{39}Ar ages and paleomagnetism of Sao Miguel lavas, Azores. *Earth and Planetary Science Letters*, *160*(3-4), 637–649.

Kelly, P., & Gubbins, D. (1997). The geomagnetic field over the past 5 million years. *Geophysical Journal International*, *128*(2), 315–330.

Kent, D. V., & Schneider, D. A. (1995). Correlation of paleointensity variation records in the Brunhes/Matuyama polarity transition interval. *Earth and Planetary Science Letters*, *129*(1-4), 135–144.

Kent, D. V., Wang, H., & Rochette, P. (2010). Equatorial paleosecular variation of the geomagnetic field from 0 to 3 Ma lavas from the Galapagos Islands. *Physics of the Earth and Planetary Interiors*, *183*(3-4), 404–412.

Kerr, A. C., Tarney, J., Marriner, G. F., Nivia, A., Klaver, G. T., & Saunders, A. D. (1996). The geochemistry and tectonic setting of late Cretaceous Caribbean and Colombian volcanism. *Journal of South American Earth Sciences*, *9*(1-2), 111–120.

Kirschvink, J. L. (1980). The least-squares line and plane and the analysis of palaeomagnetic data. *Geophysical Journal International*, *62*(3), 699–718.

Kissel, C., Rodriguez-Gonzalez, A., Laj, C., Perez-Torrado, F., Carracedo, J. C., Wandres, C., & Guillou, H. (2015). Paleosecular variation of the Earth magnetic field at the Canary Islands over the last 15 ka. *Earth and Planetary Science Letters*, *412*, 52–60.

Kono, M., & Roberts, P. H. (2002). Recent geodynamo simulations and observations of the geomagnetic field. *Reviews of Geophysics*, *40*(4), 4–1.

Kono, M., & Tanaka, H. (1995). Mapping the Gauss coefficients to the pole and the models of paleosecular variation. *Journal of Geomagnetism and Geoelectricity*, *47*(1), 115–130.

Korte, M., & Mandea, M. (2019). Geomagnetism: From Alexander von Humboldt to current challenges. *Geochemistry, Geophysics, Geosystems*, *20*(8), 3801–3820.

Kutzner, C., & Christensen, U. R. (2004). Simulated geomagnetic reversals and preferred virtual geomagnetic pole paths. *Geophysical Journal International*, *157*(3), 1105–1118.

Labrosse, S. (2003). Thermal and magnetic evolution of the Earth's core. *Physics of the Earth and Planetary Interiors*, *140*(1-3), 127–143.

Laj, C., & Channell, J. E. T. (2015). Geomagnetic excursions. In G. Schubert (Ed.), *Treatise on Geophysics* (2nd ed., pp. 343–383). Elsevier.

Laj, C., Guillou, H., Szeremeta, N., & Coe, R. (1999). Geomagnetic paleosecular variation at Hawaii around 3 Ma from a sequence of 107 lava flows at Kaena Point (Oahu). *Earth and Planetary Science Letters*, *170*(4), 365–376.

Laj, C., Kissel, C., & Roberts, A. P. (2006). Geomagnetic field behavior during the Iceland Basin and Laschamp geomagnetic excursions: A simple transitional field geometry? *Geochemistry, Geophysics, Geosystems*, *7*(3).

Laj, C., Mazaud, A., Weeks, R., Fuller, M., & Herrero-Bervera, E. (1991). Geomagnetic reversal paths. *Nature*, *351*(6326), 447–447.

Laj, C., Raïs, A., Surmont, J., Gillot, P.-Y., Guillou, H., Kissel, C., & Zanella, E. (1997). Changes of the geomagnetic field vector obtained from lava sequences on the island of Vulcano (Aeolian Islands, Sicily). *Physics of the Earth and Planetary Interiors*, *99*(3-4), 161–177.

Landeau, M., Aubert, J., & Olson, P. (2017). The signature of inner-core nucleation on the geodynamo. *Earth and Planetary Science Letters*, *465*, 193–204.

Langel, R. A., Estes, R. H., Mead, G. D., Fabiano, E. B., & Lancaster, E. R. (1980). Initial geomagnetic field model from Magsat vector data. *Geophysical Research Letters*, *7*(10), 793–796.

Lascu, I., Einsle, J. F., Ball, M. R., & Harrison, R. J. (2018). The vortex state in geologic materials: A micromagnetic perspective. *Journal of Geophysical Research: Solid Earth*, *123*(9), 7285–7304.

Lattard, D., Engelmann, R., Kontny, A., & Sauerzapf, U. (2006). Curie temperatures of synthetic titanomagnetites in the Fe-Ti-o system: Effects of composition, crystal chemistry, and thermomagnetic methods. *Journal of Geophysical Research: Solid Earth*, *111*(B12).

Lawrence, K. P., Tauxe, L., Staudigel, H., Constable, C. G., Koppers, A., McIntosh, W., & Johnson, C. L. (2009). Paleomagnetic field properties at high southern latitude. *Geochemistry, Geophysics, Geosystems*, *10*(1).

Lee, S. (1983). A study of the time-averaged paleomagnetic field for the past 195 million years. *Ph. D. Thesis, Australian National University*.

Leonhardt, R., Matzka, J., & Menor, E. A. (2003). Absolute paleointensities and paleodirections of Miocene and Pliocene lavas from Fernando de Noronha, Brazil. *Physics of the Earth and Planetary Interiors*, *139*(3-4), 285–303.

Leonhardt, R., & Soffel, H. C. (2006). The growth, collapse and quiescence of Teno volcano, Tenerife: New constraints from paleomagnetic data. *International Journal of Earth Sciences*, *95*(6), 1053–1064.

Lerner, G. A., Cronin, S. J., Turner, G. M., & Rowe, M. C. (2019). Paleomagnetic determination of the age and properties of the 1780–1800 AD dome effusion/collapse episode of Mt. Taranaki, New Zealand. *Bulletin of Volcanology*, *81*(3), 1–20.

Lhuillier, F., & Gilder, S. A. (2013). Quantifying paleosecular variation: Insights from numerical dynamo simulations. *Earth and Planetary Science Letters*, *382*, 87–97.

Lhuillier, F., Hulot, G., & Gallet, Y. (2013). Statistical properties of reversals and chrons in numerical dynamos and implications for the geodynamo. *Physics of the Earth and Planetary Interiors*, *220*, 19–36.

Lhuillier, F., Shcherbakov, V. P., Gilder, S. A., & Hagstrum, J. T. (2017). Variability of the 0–3 Ma palaeomagnetic field observed from the Boring Volcanic Field of the Pacific Northwest. *Geophysical Journal International*, *211*(1), 69–79.

Litasov, K. D., & Shatskiy, A. F. (2016). Composition of the Earth's core: A review. *Russian Geology and Geophysics*, *57*(1), 22–46.

Love, J. J. (1998). Paleomagnetic volcanic data and geometric regularity of reversals and excursions. *Journal of Geophysical Research: Solid Earth*, *103*(B6), 12435–12452.

Lowes, F. J. (1974). Spatial power spectrum of the main geomagnetic field, and extrapolation to the core. *Geophysical Journal International*, *36*(3), 717–730.

Lowrie, W. (2007). *Fundamentals of Geophysics*. Cambridge University Press.

Mahgoub, A. N., Böhnel, H., Siebe, C., Salinas, S., & Guilbaud, M.-N. (2017). Paleomagnetically inferred ages of a cluster of Holocene monogenetic eruptions in the Tacámbaro-Puruarán area (Michoacán, México): Implications for volcanic hazards. *Journal of Volcanology and Geothermal Research*, *347*, 360–370.

Mahgoub, A. N., Juárez-Arriaga, E., Böhnel, H., Siebe, C., & Pavón-Carrasco, F. J. (2019). Late-Quaternary secular variation data from Mexican volcanoes. *Earth and Planetary Science Letters*, *519*, 28–39.

Mahgoub, A. N., Reyes-Guzmán, N., Böhnel, H., Siebe, C., Pereira, G., & Dorison, A. (2018). Paleomagnetic constraints on the ages of the Holocene Malpaís de Zacapu lava flow eruptions, Michoacán (Mexico): Implications for archeology and volcanic hazards. *The Holocene*, *28*(2), 229–245.

McElhinny, M. W., McFadden, P. L., & Merrill, R. T. (1996). The time-averaged paleomagnetic field 0–5 Ma. *Journal of Geophysical Research: Solid Earth*, *101*(B11), 25007–25027.

McElhinny, M. W., & Merrill, R. T. (1975). Geomagnetic secular variation over the past 5 My. *Reviews of Geophysics*, *13*(5), 687–708.

McElhinny, M. W. (2004). Geocentric axial dipole hypothesis: A least squares perspective. *Washington DC American Geophysical Union Geophysical Monograph Series*, *145*, 1–12.

McElhinny, M. W. (2007). Geocentric Axial Dipole Hypothesis. In D. Gubbins & E. Herrero-Bervera (Eds.), *Encyclopedia of Geomagnetism and Paleomagnetism* (pp. 281–287). Springer Netherlands.

McElhinny, M. W., & McFadden, P. L. (1997). Palaeosecular variation over the past 5 Myr based on a new generalized database. *Geophysical Journal International*, *131*(2), 240–252.

McElhinny, M. W., & McFadden, P. L. (2000). *Paleomagnetism: Continents and Oceans* (2nd ed.). Academic Press.

McFadden, P. L., & McElhinny, M. W. (1984). A physical model for palaeosecular variation. *Geophysical Journal International*, *78*(3), 809–830.

McFadden, P. L., Merrill, R. T., & McElhinny, M. W. (1988). Dipole/quadrupole family modeling of paleosecular variation. *Journal of Geophysical Research: Solid Earth*, *93*(B10), 11583–11588.

McFadden, P. L., Merrill, R. T., McElhinny, M. W., & Lee, S. (1991). Reversals of the Earth's magnetic field and temporal variations of the dynamo families. *Journal of Geophysical Research: Solid Earth*, *96*(B3), 3923–3933.

McFadden, P. L., Barton, C. E., & Merrill, R. T. (1993). Do virtual geomagnetic poles follow preferred paths during geomagnetic reversals? *Nature*, *361*(6410), 342–344.

McFadden, P. L., & Merrill, R. T. (2007). Geomagnetic field, asymmetries. In D. Gubbins & E. Herrero-Bervera (Eds.), *Encyclopedia of Geomagnetism and Paleomagnetism* (pp. 313–316). Springer Netherlands.

Meduri, D. G., Biggin, A. J., Davies, C. J., Bono, R. K., Sprain, C. J., & Wicht, J. (2021). Numerical dynamo simulations reproduce paleomagnetic field behavior. *Geophysical Research Letters*, *48*(5).

Mejia, V., Böhnel, H., Opdyke, N. D., Ortega-Rivera, M. A., Lee, J. K. W., & Aranda-Gomez, J. J. (2005). Paleosecular variation and time-averaged field recorded in late Pliocene–Holocene lava flows from Mexico. *Geochemistry, Geophysics, Geosystems*, *6*(7).

Mejia, V., Opdyke, N. D., Vilas, J. F., Singer, B. S., & Stoner, J. S. (2004). Plio-Pleistocene time-averaged field in southern Patagonia recorded in lava flows. *Geochemistry, Geophysics, Geosystems*, *5*(3).

Mejia, V., Barendregt, R. W., & Opdyke, N. D. (2002). Paleosecular variation of Brunhes age lava flows from British Columbia, Canada. *Geochemistry, Geophysics, Geosystems*, *3*(12), 1–14.

Merrill, R. T., & McFadden, P. L. (1994). Geomagnetic field stability: Reversal events and excursions. *Earth and Planetary Science Letters*, *121*(1-2), 57–69.

Merrill, R. T., McFadden, P. L., & McElhinny, M. W. (1990). Paleomagnetic tomography of the core-mantle boundary. *Physics of the Earth and Planetary Interiors*, *64*(1), 87–101.

Merrill, R. T., & McElhinny, M. W. (1977). Anomalies in the time-averaged paleomagnetic field and their implications for the lower mantle. *Reviews of Geophysics*, *15*(3), 309–323.

Merrill, R. T., McElhinny, M. W., & McFadden, P. L. (1998). *The Magnetic Field of the Earth: Paleomagnetism, the Core, and the Deep Mantle* (2nd). Academic Press.

Merrill, R. T., & McFadden, P. L. (2003). The geomagnetic axial dipole field assumption. *Physics of the Earth and Planetary Interiors*, *139*(3-4), 171–185.

Michalk, D. M., Böhnel, H. N., Nowaczyk, N. R., Aguírre-Diaz, G. J., López-Martínez, M., Ownby, S., & Negendank, J. F. W. (2013). Evidence for geomagnetic excursions recorded in Brunhes and Matuyama Chron lavas from the Trans-Mexican volcanic belt. *Journal of Geophysical Research: Solid Earth*, *118*(6), 2648–2669.

Miki, M., Inokuchi, H., Yamaguchi, S., Matsuda, J.-i., Nagao, K., Isezaki, N., & Yaskawa, K. (1998). Geomagnetic paleosecular variation in Easter Island, the southeast Pacific. *Physics of the Earth and Planetary Interiors*, *106*(1-2), 93–101.

Mitchell, R. J., Jaeger, D. J., Diehl, J. F., & Hammond, P. E. (1989). Palaeomagnetic results from the Indian Heaven volcanic field, south-central Washington. *Geophysical Journal International*, *97*(3), 381–390.

Mojica, J. (1980). Observaciones acerca del estado actual del conocimiento de la Formación Payandé (Triásico Superior), Valle Superior del río Magdalena, Colombia. *Geología Colombiana*, *11*, 67–88.

Mojica, J., & Prinz-Grimm, P. (2000). La fauna de amonitas del Triásico Tardío en el Miembro Chicalá (= parte baja de la Formación Saldaña) en Payandé, Tolima, Colombia. *Geología Colombiana*, *25*, 13–23.

Monsalve-Bustamante, M. L. (2020). The volcanic front in Colombia: Segmentation and recent and historical activity. *The Geology of Colombia*, *4*, 97–159.

Monster, M. W. L., Van Galen, J., Kuiper, K. F., Dekkers, M. J., & De Groot, L. V. (2018). A Late-Quaternary full-vector geomagnetic record from El Golfo section, El Hierro, Canary Islands. *Geophysical Journal International*, *215*(3), 1701–1717.

Montes, C., Rodriguez-Corcho, A. F., Bayona, G., Hoyos, N., Zapata, S., & Cardona, A. (2019). Continental margin response to multiple arc-continent collisions: The northern Andes-Caribbean margin. *Earth-Science Reviews*, *198*, 102903.

Ogg, J. G. (2020). Geomagnetic polarity time scale. In *Geologic time scale 2020* (pp. 159–192). Elsevier.

Oliva-Urcia, B., Gil-Peña, I., Maestro, A., López-Martínez, J., Galindo-Zaldívar, J., Soto, R., Gil-Imaz, A., Rey, J., & Pueyo, O. (2016). Paleomagnetism from Deception Island (South Shetlands archipelago, Antarctica), new insights into the interpretation of the volcanic evolution using a geomagnetic model. *International Journal of Earth Sciences*, *105*(5), 1353–1370.

Olson, P. (2015). Core dynamics: An Introduction and Overview. In G. Schubert (Ed.), *Treatise on Geophysics* (2nd ed., pp. 1–25). Elsevier.

Olson, P., & Christensen, U. R. (2002). The time-averaged magnetic field in numerical dynamos with non-uniform boundary heat flow. *Geophysical Journal International*, *151*(3), 809–823.

Olson, P., Coe, R. S., Driscoll, P. E., Glatzmaier, G. A., & Roberts, P. H. (2010). Geodynamo reversal frequency and heterogeneous core–mantle boundary heat flow. *Physics of the Earth and Planetary Interiors*, *180*(1-2), 66–79.

Olson, P., Hinnov, L. A., & Driscoll, P. E. (2014). Nonrandom geomagnetic reversal times and geodynamo evolution. *Earth and Planetary Science Letters*, *388*, 9–17.

Opdyke, N. D., & Henry, K. W. (1969). A test of the dipole hypothesis. *Earth and Planetary Science Letters*, *6*(2), 139–151.

Opdyke, N. D., Kent, D. V., Foster, D. A., & Huang, K. (2015). Paleomagnetism of Miocene volcanics on Sao Tome: Paleosecular variation at the equator and a comparison to its latitudinal dependence over the last 5 Myr. *Geochemistry, Geophysics, Geosystems*, *16*(11), 3870–3882.

Opdyke, N. D., & Channell, J. E. T. (1996). *Magnetic stratigraphy*. Academic press.

Opdyke, N. D., Hall, M., Mejia, V., Huang, K., & Foster, D. A. (2006). Time-averaged field at the equator: Results from Ecuador. *Geochemistry, Geophysics, Geosystems*, *7*(11).

Opdyke, N. D., Kent, D. V., Huang, K., Foster, D. A., & Patel, J. P. (2010). Equatorial paleomagnetic time-averaged field results from 0–5 Ma lavas from Kenya and the latitudinal variation of angular dispersion. *Geochemistry, Geophysics, Geosystems*, *11*(5).

Opdyke, N. D., & Musgrave, R. (2004). Paleomagnetic results from the Newer Volcanics of Victoria: Contribution to the time averaged field initiative. *Geochemistry, Geophysics, Geosystems*, *5*(3).

Panaiotu, C. G., Jicha, B. R., Singer, B. S., Ţugui, A., Seghedi, I., Panaiotu, A. G., & Necula, C. (2013). $^{40}Ar/^{39}Ar$ chronology and paleomagnetism of Quaternary basaltic lavas from the Perşani Mountains (East Carpathians). *Physics of the Earth and Planetary Interiors*, *221*, 1–14.

Panaiotu, C. G., Visan, M., Tugui, A., Seghedi, I., & Panaiotu, A. G. (2012). Palaeomagnetism of the South Harghita volcanic rocks of the East Carpathians: Implications for tectonic rotations and palaeosecular variation in the past 5 Ma. *Geophysical Journal International*, *189*(1), 369–382.

Panovska, S., & Constable, C. G. (2017). An activity index for geomagnetic paleosecular variation, excursions, and reversals. *Geochemistry, Geophysics, Geosystems*, *18*(4), 1366–1375.

Panovska, S., Constable, C. G., & Brown, M. C. (2018a). Global and regional assessments of paleosecular variation activity over the past 100 ka. *Geochemistry, Geophysics, Geosystems*, *19*(5), 1559–1580.

Panovska, S., Constable, C. G., & Korte, M. (2018b). Extending global continuous geomagnetic field reconstructions on timescales beyond human civilization. *Geochemistry, Geophysics, Geosystems*, *19*(12), 4757–4772.

Panovska, S., Korte, M., & Constable, C. G. (2019). One hundred thousand years of geomagnetic field evolution. *Reviews of Geophysics*, *57*(4), 1289–1337.

Pardo, N., Pulgarín, B., Betancourt, V., Lucchi, F., & Valencia, L. J. (2019). Facing geological mapping at low-latitude volcanoes: The Doña Juana Volcanic Complex study-case, SW-Colombia. *Journal of Volcanology and Geothermal Research*, *385*, 46–67.

Pavlov, V., & Gallet, Y. (2005). A third superchron during the Early Paleozoic. *Episodes-Newsmagazine of the International Union of Geological Sciences*, *28*(2), 78–84.

Peña, R. M., Goguitchaichvili, A., Guilbaud, M.-N., Martínez, V. C. R., Rathert, M. C., Siebe, C., Reyes, B. A., & Morales, J. (2014). Paleomagnetic secular variation study of Ar–Ar dated lavas flows from Tacambaro Area (Central Mexico): Possible evidence of Intra-Jaramillo geomagnetic excursion in volcanic rocks. *Physics of the Earth and Planetary Interiors*, *229*, 98–109.

Peña, R. M., Goguitchaichvili, A., Henry, B., Sánchez-Bettucci, L., Morales, J., Reyes, B. A., Soler-Arechalde, A. M., & Calvo-Rathert, M. (2011). Plio-Pleistocene paleomagnetic record from the Michoacan-Guanajuato monogenetic volcanic field (Western Mexico). *Studia Geophysica et Geodaetica*, *55*(2), 311–328.

Petronille, M., Goguitchaichvili, A., Henry, B., Alva-Valdivia, L. M., Rosas-Elguera, J., Urrutia-Fucugauchi, J., Rodriguez Cejá, M., & Calvo-Rathert, M. (2005). Paleomagnetism of Ar-Ar dated lava flows from the Ceboruco-San Pedro volcanic field (western Mexico): Evidence for the Matuyama-Brunhes transition precursor and a fully reversed geomagnetic event in the Brunhes chron. *Journal of Geophysical Research: Solid Earth*, *110*(B8).

Pindell, J. L., & Kennan, L. (2009). Tectonic evolution of the Gulf of Mexico, Caribbean and northern South America in the mantle reference frame: An update. *Geological Society, London, Special Publications*, *328*(1), 1–55.

Pinton, A., Giordano, G., Speranza, F., & Þórðarson, Þ. (2018). Paleomagnetism of Holocene lava flows from the Reykjanes peninsula and the Tungnaá lava sequence (Iceland): Implications for flow correlation and ages. *Bulletin of Volcanology*, *80*(1), 1–19.

Quidelleur, X., Carlut, J., Tchilinguirian, P., Germa, A., & Gillot, P.-Y. (2009). Paleomagnetic directions from mid-latitude sites in the southern hemisphere (Argentina): Contribution to time averaged field models. *Physics of the Earth and Planetary Interiors*, *172*(3-4), 199–209.

Quidelleur, X., & Courtillot, V. (1996). On low-degree spherical harmonic models of paleosecular variation. *Physics of the Earth and Planetary Interiors*, *95*(1-2), 55–77.

Quidelleur, X., Valet, J.-P., Courtillot, V., & Hulot, G. (1994). Long-term geometry of the geomagnetic field for the last five million years: An updated secular variation database. *Geophysical Research Letters*, *21*(15), 1639–1642.

Raïs, A., Laj, C., Surmont, J., Gillot, P.-Y., & Guillou, H. (1996). Geomagnetic field intensity between 70 000 and 130 000 years BP from a volcanic sequence on La Réunion Indian Ocean. *Earth and Planetary Science Letters*, *140*(1-4), 173–189.

Ramos, V. A. (2009). Anatomy and global context of the Andes: Main geologic features and the Andean orogenic cycle. *Backbone of the Americas: Shallow subduction, plateau uplift, and ridge and terrane collision*, *204*, 31–65.

Ricci, J., Carlut, J., & Valet, J.-P. (2018). Paleosecular variation recorded by Quaternary lava flows from Guadeloupe Island. *Scientific Reports*, *8*(1), 1–14.

Roberts, A. P. (2008). Geomagnetic excursions: Knowns and unknowns. *Geophysical Research Letters*, *35*(17).

Roberts, A. P., Almeida, T. P., Church, N. S., Harrison, R. J., Heslop, D., Li, Y., Li, J., Muxworthy, A. R., Williams, W., & Zhao, X. (2017). Resolving the origin of pseudo-single domain magnetic behavior. *Journal of Geophysical Research: Solid Earth*, *122*(12), 9534–9558.

Roberts, A. P., Heslop, D., Zhao, X., & Pike, C. R. (2014). Understanding fine magnetic particle systems through use of first-order reversal curve diagrams. *Reviews of Geophysics*, *52*(4), 557–602.

Roberts, A. P., Pike, C. R., & Verosub, K. L. (2000). First-order reversal curve diagrams: A new tool for characterizing the magnetic properties of natural samples. *Journal of Geophysical Research: Solid Earth*, *105*(B12), 28461–28475.

Roberts, A. P., Tauxe, L., Heslop, D., Zhao, X., & Jiang, Z. (2018). A critical appraisal of the “Day” diagram. *Journal of Geophysical Research: Solid Earth*, *123*(4), 2618–2644.

Roberts, P. H., & Stix, M. (1972). α-effect dynamos, by the Bullard-Gellman formalism. *Astron. Astrophys*, *18*, 453–466.

Roberts, P. H., & King, E. M. (2013). On the genesis of the Earth's magnetism. *Reports on Progress in Physics*, *76*(9), 096801.

Rodríguez, G., Arango, M. I., Zapata, G., & Bermúdez, J. G. (2018). Petrotectonic characteristics, geochemistry, and U-Pb geochronology of Jurassic plutons in the Upper Magdalena Valley-Colombia: Implications on the evolution of magmatic arcs in the NW Andes. *Journal of South American Earth Sciences*, *81*, 10–30.

Rodríguez-Trejo, A., Alva-Valdivia, L. M., & Vidal-Solano, J. R. (2019). Paleomagnetism and rock magnetic properties of Late Pleistocene volcanism from El Pinacate Volcanic Field, northwest Mexico. *Journal of South American Earth Sciences*, *96*, 102368.

Roperch, P., Chauvin, A., Lara, L. E., & Moreno, H. (2015). Secular variation of the Earth's magnetic field and application to paleomagnetic dating of historical lava flows in Chile. *Physics of the Earth and Planetary Interiors*, *242*, 65–78.

Rother, M., Korte, M., Morschhauser, A., Vervelidou, F., Matzka, J., & Stolle, C. (2021). The Mag.num core field model as a parent for IGRF-13, and the recent evolution of the South Atlantic Anomaly. *Earth, Planets and Space*, *73*(1), 1–17.

Ruiz-Martínez, V. C., Urrutia-Fucugauchi, J., & Osete, M. L. (2010). Palaeomagnetism of the Western and Central sectors of the Trans-Mexican volcanic belt–implications for tectonic rotations and palaeosecular variation in the past 11 Ma. *Geophysical Journal International*, *180*(2), 577–595.

Salminen, J., & Pesonen, L. J. (2007). Paleomagnetic and rock magnetic study of the Mesoproterozoic sill, Valaam island, Russian Karelia. *Precambrian Research*, *159*(3-4), 212–230.

Sánchez-Duque, A., Mejia, V., Opdyke, N. D., Huang, K., & Rosales-Rivera, A. (2016). Plio-Pleistocene paleomagnetic secular variation and time-averaged field: Ruiz-Tolima volcanic chain, Colombia. *Geochemistry, Geophysics, Geosystems*, *17*(2), 538–549.

Schneider, D. A., & Kent, D. V. (1990). The time-averaged paleomagnetic field. *Reviews of Geophysics*, *28*(1), 71–96.

Selkin, P. A., & Tauxe, L. (2000). Long-term variations in palaeointensity. *Philosophical Transactions of the Royal Society of London. Series A: Mathematical, Physical and Engineering Sciences*, *358*(1768), 1065–1088.

Shah, J., Koppers, A. A., Leitner, M., Leonhardt, R., Muxworthy, A. R., Heunemann, C., Bachtadse, V., Ashley, J. A., & Matzka, J. (2016). Palaeomagnetic evidence for the persistence or recurrence of geomagnetic main field anomalies in the South Atlantic. *Earth and Planetary Science Letters*, *441*, 113–124.

Smirnov, A. V., Tarduno, J. A., & Evans, D. A. D. (2011). Evolving core conditions ca. 2 billion years ago detected by paleosecular variation. *Physics of the Earth and Planetary Interiors*, *187*(3-4), 225–231.

Spikings, R., Cochrane, R., Villagomez, D., Van der Lelij, R., Vallejo, C., Winkler, W., & Beate, B. (2015). The geological history of northwestern South America: From Pangaea to the early collision of the Caribbean Large Igneous Province (290–75 Ma). *Gondwana Research*, *27*(1), 95–139.

Sprain, C. J., Biggin, A. J., Davies, C. J., Bono, R. K., & Meduri, D. G. (2019). An assessment of long duration geodynamo simulations using new paleomagnetic modeling criteria (QPM). *Earth and Planetary Science Letters*, *526*, 115758.

Sreenivasan, B. (2010). Modelling the geodynamo: Progress and challenges. *Current Science*, 1739–1750.

Stone, D. B., & Layer, P. W. (2006). Paleosecular variation and GAD studies of 0–2 Ma flow sequences from the Aleutian Islands, Alaska. *Geochemistry, Geophysics, Geosystems*, *7*(4).

Taboada, A., Rivera, L. A., Fuenzalida, A., Cisternas, A., Philip, H., Bijwaard, H., Olaya, J., & Rivera, C. (2000). Geodynamics of the northern Andes: Subductions and intracontinental deformation (Colombia). *Tectonics*, *19*(5), 787–813.

Tanaka, H., Kamizaki, R., & Yamamoto, Y. (2007). Palaeomagnetism of the Older Ontake Volcano, Japan: Contributions to the palaeosecular variation for 750–400 ka, the lower half of the Brunhes Chron. *Geophysical Journal International*, *169*(1), 81–90.

Tanaka, H., Kawamura, K., Nagao, K., & Houghton, B. F. (1997). K-Ar ages and paleosecular variation of direction and intensity from Quaternary lava sequences in the Ruapehu Volcano, New Zealand. *Journal of Geomagnetism and Geoelectricity*, *49*(4), 587–599.

Tanaka, H., & Kobayashi, T. (2003). Paleomagnetism of the late Quaternary Ontake Volcano, Japan: Directions, intensities, and excursions. *Earth, Planets and Space*, *55*(4), 189–202.

Tanaka, H., Komuro, N., & Turner, G. M. (2009). Palaeosecular variation for 0.1-21 ka from the Okataina Volcanic Centre, New Zealand. *Earth, Planets and Space*, *61*(1), 213–225.

Tanty, C., Carlut, J., Valet, J.-P., & Germa, A. (2015). Palaeosecular variation recorded by 9 ka to 2.5-Ma-old lavas from Martinique Island: New evidence for the La Palma aborted reversal ~617 ka ago. *Geophysical Journal International*, *200*(2), 917–934.

Tarduno, J. A., Watkeys, M. K., Huffman, T. N., Cottrell, R. D., Blackman, E. G., Wendt, A., Scribner, C. A., & Wagner, C. L. (2015). Antiquity of the South Atlantic Anomaly and evidence for top-down control on the geodynamo. *Nature Communications*, *6*(1), 1–6.

Tauxe, L., Shaar, R., Jonestrask, L., Swanson-Hysell, N. L., Minnett, R., Koppers, A. A. P., Constable, C. G., Jarboe, N., Gaastra, K., & Fairchild, L. (2016). Pmagpy: Software package for paleomagnetic data analysis and a bridge to the Magnetics Information Consortium (MagIC) Database. *Geochemistry, Geophysics, Geosystems*, *17*(6), 2450–2463.

Tauxe, L. (2003). *Paleomagnetic principles and practice* (Vol. 17). Springer Science & Business Media.

Tauxe, L. (2010). *Essentials of paleomagnetism*. University of California Press.

Tauxe, L., Constable, C., Johnson, C. L., Koppers, A. A. P., Miller, W. R., & Staudigel, H. (2003). Paleomagnetism of the southwestern USA recorded by 0–5 Ma igneous rocks. *Geochemistry, Geophysics, Geosystems*, *4*(4).

Tauxe, L., & Kent, D. V. (2004). A simplified statistical model for the geomagnetic field and the detection of shallow bias in paleomagnetic inclinations: Was the ancient magnetic field dipolar? In *Timescales of the paleomagnetic field* (pp. 101–115). American Geophysical Union.

Tauxe, L., Luskin, C., Selkin, P., Gans, P., & Calvert, A. (2004). Paleomagnetic results from the Snake River Plain: Contribution to the time-averaged field global database. *Geochemistry, Geophysics, Geosystems*, *5*(8).

Tauxe, L., Staudigel, H., & Wijbrans, J. R. (2000). Paleomagnetism and $^{40}Ar/^{39}Ar$ ages from La Palma in the Canary Islands. *Geochemistry, Geophysics, Geosystems*, *1*(9).

Terra-Nova, F., Amit, H., & Choblet, G. (2019). Preferred locations of weak surface field in numerical dynamos with heterogeneous core–mantle boundary heat flux: Consequences for the South Atlantic Anomaly. *Geophysical Journal International*, *217*(2), 1179–1199.

Terra-Nova, F., Amit, H., Hartmann, G. A., Trindade, R. I. F., & Pinheiro, K. J. (2017). Relating the South Atlantic Anomaly and geomagnetic flux patches. *Physics of the Earth and Planetary Interiors*, *266*, 39–53.

Trujillo, J. F. D., Villegas, G. E. T., Molina, A. C., & Velazco, M. C. (2010). Geology, Geochronology and Geochemitry of Morasurco Volcano, Pasto, Colombia. *Boletín de Ciencias de la Tierra*, (27), 25–36.

Udagawa, S., Kitagawa, H., Gudmundsson, A., Hiroi, O., Koyaguchi, T., Tanaka, H., Kristjansson, L., & Kono, M. (1999). Age and magnetism of lavas in Jökuldalur area, Eastern Iceland: Gilsá event revisited. *Physics of the Earth and Planetary Interiors*, *115*(2), 147–171.

Valet, J.-P., & Fournier, A. (2016). Deciphering records of geomagnetic reversals. *Reviews of Geophysics*, *54*(2), 410–446.

Valet, J.-P., & Herrero-Bervera, E. (2011). Time-averaged and mean axial dipole field. In *The Earth's magnetic interior* (pp. 131–137). Springer Science & Business Media.

Valet, J.-P., Meynadier, L., & Guyodo, Y. (2005). Geomagnetic dipole strength and reversal rate over the past two million years. *Nature*, *435*(7043), 802–805.

Vandamme, D. (1994). A new method to determine paleosecular variation. *Physics of the Earth and Planetary Interiors*, *85*(1-2), 131–142.

Veikkolainen, T., & Pesonen, L. J. (2014). Palaeosecular variation, field reversals and the stability of the geodynamo in the Precambrian. *Geophysical Journal International*, *199*(3), 1515–1526.

Villagómez, D., Spikings, R., Magna, T., Kammer, A., Winkler, W., & Beltrán, A. (2011). Geochronology, geochemistry and tectonic evolution of the Western and Central cordilleras of Colombia. *Lithos*, *125*(3-4), 875–896.

Vişan, M., Panaiotu, C. G., Necula, C., & Dumitru, A. (2016). Palaeomagnetism of the Upper Miocene-Lower Pliocene lavas from the East Carpathians: Contribution to the paleosecular variation of geomagnetic field. *Scientific Reports*, *6*(1), 1–7.

Wagner, L. S., Jaramillo, J. S., Ramírez-Hoyos, L. F., Monsalve, G., Cardona, A., & Becker, T. W. (2017). Transient slab flattening beneath Colombia. *Geophysical Research Letters*, *44*(13), 6616–6623.

Winch, D. (2007). Harmonics, spherical. In D. Gubbins & E. Herrero-Bervera (Eds.), *Encyclopedia of Geomagnetism and Paleomagnetism* (pp. 377–394). Springer Netherlands.

Yamamoto, Y., Shimura, K., Tsunakawa, H., Kogiso, T., Uto, K., Barsczus, H. G., Oda, H., Yamazaki, T., & Kikawa, E. (2002). Geomagnetic paleosecular variation for the past 5 Ma in the Society Islands, French Polynesia. *Earth, Planets and Space*, *54*(7), 797–802.

Yamamoto, Y., Tsunakawa, H., Shaw, J., & Kono, M. (2007). Paleomagnetism of the Datong monogenetic volcanoes in China: Paleodirection and paleointensity during the middle to early Brunhes Chron. *Earth, Planets and Space*, *59*(7), 727–746.

Zapata, S., Cardona, A., Jaramillo, J. S., Patiño, A., Valencia, V., León, S., Mejía, D., Pardo-Trujillo, A., & Castañeda, J. P. (2019). Cretaceous extensional and compressional tectonics in the Northwestern Andes, prior to the collision with the Caribbean oceanic plateau. *Gondwana Research*, *66*, 207–226.

Zhang, N., & Zhong, S. (2011). Heat fluxes at the Earth's surface and core–mantle boundary since Pangea formation and their implications for the geomagnetic superchrons. *Earth and Planetary Science Letters*, *306*(3-4), 205–216.

Zhao, X., Roberts, A. P., Heslop, D., Paterson, G. A., Li, Y., & Li, J. (2017). Magnetic domain state diagnosis using hysteresis reversal curves. *Journal of Geophysical Research: Solid Earth*, *122*(7), 4767–4789.

Ziegler, L. B., Constable, C. G., Johnson, C. L., & Tauxe, L. (2011). PADM2M: A penalized maximum likelihood model of the 0–2 Ma palaeomagnetic axial dipole moment. *Geophysical Journal International*, *184*(3), 1069–1089.

Zijderveld, J. D. A. (1967). AC demagnetization of rocks: Analysis of results. In *Methods in paleomagnetism*. Amsterdam: Elsevier.

A. Mathematical description for spherical harmonics

A.1 Scalar potential of the geomagnetic field

The spherical harmonic description for the geomagnetic field was proposed by Gauss in 1893, using two Maxwell equations of electromagnetism:

$$\nabla \times \mathbf{H} = \mathbf{J} + \frac{\partial \mathbf{D}}{\partial t} \qquad \text{(Ampere's law)} \tag{A.1}$$

and,

$$\nabla . \mathbf{B} = 0 \qquad \text{(Gauss's law for magnetism)}, \tag{A.2}$$

where **H** is the magnetic field vector, **B** is the magnetic induction vector, **J** is the electric current density vector, and **D** corresponds to the electric displacement current density. The region of the Earth's surface ~50km can be considered as an electric vacuum zone. In this region, it is assumed that there are no electric currents, thereby **J = 0** and $\partial \mathbf{D}/\partial t = 0$. Under this condition $\nabla \times \mathbf{H} = 0$, which indicates that **H** is conservative and defined as the negative gradient of the scalar potential function V, given by:

$$\mathbf{H} = -\nabla V. \tag{A.3}$$

Above the Earth's surface $\mathbf{B} = \mu_0 \mathbf{H}$, where μ_0 $(= 4\pi \times 10^{-7})$ is the magnetic permeability. Using Equation (A.2) $\nabla . \mathbf{H} = 0$ and applying in Equation (A.3), the potential V satisfy Laplace's equation:

$$\nabla^2 V = 0. \tag{A.4}$$

Using spherical coordinates (r, θ, ϕ), where r is the distance between a given point and the Earth's center, θ is the colatitude and ϕ is the longitude, the Equation (A.4) is expressed by:

$$\nabla^2 V = \frac{1}{r^2}\frac{\partial}{\partial r}\left(r^2 \frac{\partial V}{\partial r}\right) + \frac{1}{r^2 \sin\theta}\frac{\partial}{\partial \theta}\left(\sin\theta \frac{\partial V}{\partial \theta}\right) + \frac{1}{r^2 \sin^2\theta}\frac{\partial^2 V}{\partial \phi^2} = 0. \tag{A.5}$$

The Equation (A.5) can be solved by the method of separation of variables, considering V as:

$$V(r,\theta,\phi) = U(r)P(\theta)Q(\phi). \tag{A.6}$$

The general solution this equation (for more details see Winch, 2007) is given by:

$$V(r,\theta,\phi) = \sum_{l=1}^{\infty}\sum_{m=0}^{l}\left(A_{lm}r^{l} + \frac{B_{lm}}{r^{l+1}}\right)Y_{l}^{m}(\theta,\phi), \tag{A.7}$$

where A_{lm} and B_{lm} are constants and the $Y_l^m(\theta,\phi)$ are surface harmonics (commonly referred to as spherical harmonics) of degree l and order m, expressed by:

$$Y_{l}^{m}(\theta,\phi) = \left[\frac{(2l+1)(l-m)!}{4\pi(l+m)!}\right]^{\frac{1}{2}} P_{l,m}(\cos\theta)e^{im\phi}. \tag{A.8}$$

The $P_{l,m}(\cos\theta)$ term represents the associated Legendre polynomials and are determined by recursion formula:

$$P_{l,m}(\cos\theta) = P_{l,m}(u) = \frac{1}{2^{l}l!}(1-u^{2})^{\frac{m}{2}}\frac{d^{l+m}}{du^{l+m}}(u^{2}-1)^{l}. \tag{A.9}$$

It is conventional to use the partially normalized Schmidt functions $P_{l,m}$ related to the associated Legendre polynomials, given by:

$$P_{l}^{m}(\theta) = \begin{cases} P_{l,m}(\theta) & \text{for} \quad m = 0 \\ \left[\dfrac{2(l-m)!}{(l+m)!}\right]^{\frac{1}{2}} P_{l,m}(\theta) & \text{for} \quad m > 0. \end{cases} \tag{A.10}$$

The harmonic terms $P_{l,m}(\theta)$ define the field geometry (on the surface of a sphere) by the intersection of latitudinal zones and longitudinal sectors. In the case of $m = 0$, the surface harmonics are called *zonal harmonics* with variations only in the latitudinal coordinate. When $m = l$ the harmonic surfaces are designated as *sectoral harmonics* with variations only in the longitudinal direction. The *tesseral harmonics* are associated with values of $0 < m < l$ and exhibit variations in both latitudinal and longitudinal coordinates.

Spherical harmonic analysis enables the separation of external and internal sources of the geomagnetic field from a reference point. The geomagnetic field of internal origin is represented by B_{lm} coefficients. In this condition, there are no external sources and the radial component of the field $(-\partial V/\partial r)$ must disappear at infinity without the presence of positive powers of r in V. On the other hand, a field of external origin is described by the A_{lm} coefficients. Thus, there are no internal sources, $-\partial V/\partial r$ must be infinite and consequently no negative powers of r can occur in V.

Considering only the magnetic scalar potential of internal sources, the Equation (A.7) can be rewritten as:

$$V_{int}(r,\theta,\phi,t) = \frac{a}{\mu_0}\sum_{l=1}^{\infty}\sum_{m=0}^{l}\left(\frac{a}{r}\right)^{l+1}(g_l^m(t)\cos m\phi + h_l^m(t)\sin m\phi)P_l^m(\cos\theta). \tag{A.11}$$

The terms g_l^m and h_l^m are known as Gauss coefficients calculated for a given period or instant of time, and a represents the Earth's radius (~6371 km). Spherical harmonics coefficients with degree $l = 1$ correspond to a dipole field, for instance, the g_1^0 term is referred to as axial geocentric dipole, while g_1^1 and h_1^1 terms represent the dipole components in the equatorial plane. The Gauss coefficients that have $l \geq 2$ represent the non-dipole field contributions. Thus, the coefficients with values of $l = 2$ and $l = 3$ are associated with the quadrupole and octopole components, respectively.

Gauss coefficients can be determined from direct measurements of magnetic observatories and satellites, or indirectly inferred through directional data and field intensity in archaeological and geological materials. Geomagnetic field models that use inversion methods allow the calculation of a set of coefficients that best represent the measurements performed on the Earth's surface. Based on these measurements, the geomagnetic field components (X, Y and Z) in spherical coordinates are determined as:

$$X = \frac{1}{r}\frac{\partial V}{\partial\theta}; \quad Y = -\frac{1}{r\sin\theta}\frac{\partial V}{\partial\phi}; \quad Z = \frac{\partial V}{\partial r}. \tag{A.12}$$

These three vector components expanded in spherical harmonics are expressed by:

$$X = \sum_{l=1}^{\infty}\sum_{m=0}^{l}\left(\frac{a}{r}\right)^{l+2}(g_l^m(t)\cos m\phi + h_l^m(t)\sin m\phi)\frac{d}{d\theta}P_l^m(\cos\theta) \tag{A.13}$$

$$Y = \frac{1}{\sin\theta}\sum_{l=1}^{\infty}\sum_{m=0}^{l} m\left(\frac{a}{r}\right)^{l+2}(g_l^m(t)\sin m\phi - h_l^m(t)\cos m\phi)P_l^m(\cos\theta) \tag{A.14}$$

$$Z = \sum_{l=1}^{\infty}\sum_{m=0}^{l} -(l+1)\left(\frac{a}{r}\right)^{l+2}(g_l^m(t)\cos m\phi + h_l^m(t)\sin m\phi)P_l^m(\cos\theta) \tag{A.15}$$

A.2 Dipole Equation

This section presents the basic equations to obtain the dipole formula described by a geocentric axial dipole field (Figure A.1) using spherical coordinates (r, θ, ϕ) and considering p the magnetic colatitude defined as $\pi - \theta$.

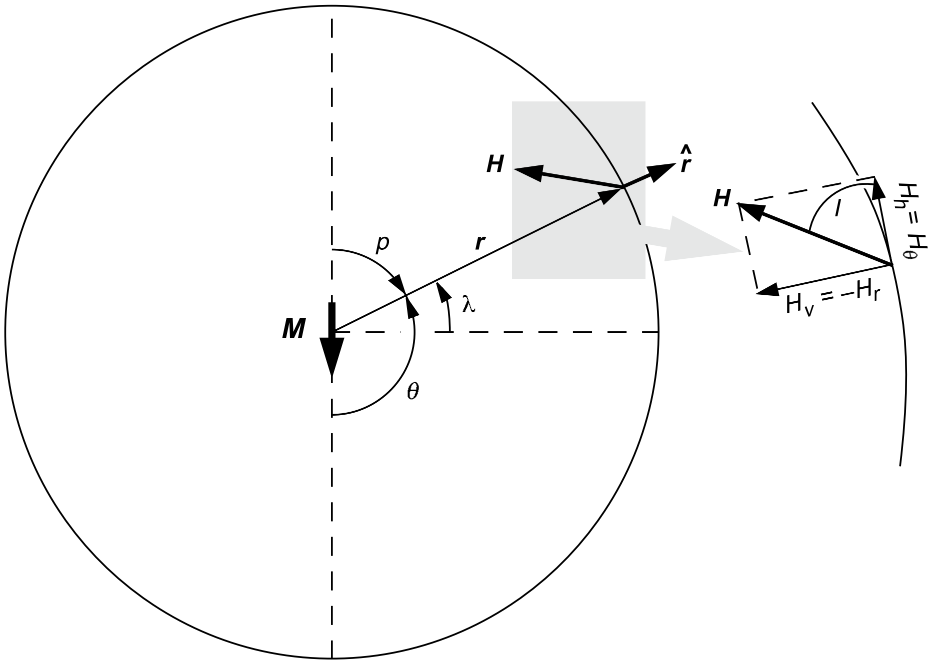

Figure A.1 – Representation of the geocentric axial dipole. The magnetic dipole moment **M** is represented by the large arrow. The parameters θ, p, λ, r are the polar angle, magnetic colatitude, geographic latitude and radial distance from the magnetic dipole, respectively. **H** is the magnetic field yielded by the dipole, $\hat{\mathbf{r}}$ is the unit vector in radial direction r. The gray shaded area shows the vector **H** that can be divided into vertical ($H_v = -H_r$) and horizontal ($H_h = H_\theta$) components. From Butler (1998).

Initially, the scalar potential of a magnetic dipole is defined as:

$$V = \frac{\mathbf{M}.\hat{\mathbf{r}}}{r^2} = \frac{M\cos\theta}{r^2}. \tag{A.16}$$

This equation is used to calculate the magnetic field **H**, as the gradient of the magnetic scalar potential:

$$\mathbf{H} = -\nabla V = -\left(\frac{\partial}{\partial r}\hat{\mathbf{r}} + \frac{1}{r}\frac{\partial}{\partial\theta}\hat{\theta}\right)\left(\frac{M\cos\theta}{r^2}\right). \tag{A.17}$$

The solution of partial derivatives is given by:

$$\mathbf{H} = -\frac{\partial}{\partial r}\left(\frac{M\cos\theta}{r^2}\right)\hat{\mathbf{r}} - \frac{1}{r}\frac{\partial}{\partial\theta}\left(\frac{M\cos\theta}{r^2}\right)\hat{\theta} \tag{A.18}$$

$$\mathbf{H} = \frac{2M\cos\theta}{r^3}\hat{\mathbf{r}} + \frac{M\sin\theta}{r^3}\hat{\theta} = H_r\hat{\mathbf{r}} + H_\theta\hat{\theta}. \tag{A.19}$$

The horizontal component of the field (H_h) is obtained by:

$$H_h = H_\theta = \frac{M\sin\theta}{r^3} = \frac{M\sin(\pi-\theta)}{r^3} = \frac{M\sin p}{r^3}. \tag{A.20}$$

Substituting

$$p = \frac{\pi}{2} - \lambda, \tag{A.21}$$

in Equation (A.20) deals to

$$H_h = \frac{M\cos\lambda}{r^3}, \tag{A.22}$$

where λ is the geographic latitude.

From Equation (A.19), the vertical component of the field (H_v) is:

$$H_v = -H_r = -\frac{2M\cos\theta}{r^3} = \frac{2M\cos p}{r^3}. \tag{A.23}$$

This equation can be rewritten in terms of geographic latitude as:

$$H_v = \frac{2M\sin\lambda}{r^3}. \tag{A.24}$$

The inclination (I) is defined as:

$$\tan I = \frac{H_v}{H_h} = \left(\frac{2M\cos p}{r^3}\right)\left(\frac{r^3}{M\sin p}\right) = 2\cot p. \tag{A.25}$$

Using Equation (A.21), the inclination as function of geographic latitude is expressed by:

$$tanI = 2tan\lambda. \tag{A.26}$$

This equation is known as the *dipole equation*.

A.3 Inclination Anomaly Model

Considering only the harmonic zonal terms ($m = 0$) of the magnetic potential V, Equation (A.11) is rewritten as follows:

$$V = \frac{a}{\mu_0}\sum_{l=1}^{\infty}\left(\frac{a}{r}\right)^{l+1} g_l^0 P_l^0(\cos\theta). \tag{A.27}$$

Using the above equation, the X and Z components of the magnetic field are determined as:

$$X = -\frac{1}{r}\frac{\partial V}{\partial \theta} = -\frac{1}{\mu_0}\sum_l \left(\frac{a}{r}\right)^{l+2} g_l^0 \frac{d}{d\theta}P_l^0(\cos\theta) \tag{A.28}$$

$$Z = -\frac{\partial V}{\partial r} = -\frac{1}{\mu_0}\sum_l -(l+1)\left(\frac{a}{r}\right)^{l+2} g_l^0 P_l^0(\cos\theta), \tag{A.29}$$

For $r = a$ (at the Earth's surface), the Equations (A.28) and (A.29) follow as:

$$X = -\frac{1}{\mu_0}\sum_l g_l^0 \frac{d}{d\theta}P_l^0(\cos\theta) \tag{A.30}$$

$$Z = \frac{1}{\mu_0}\sum_l (l+1) g_l^0 P_l^0(\cos\theta). \tag{A.31}$$

The field model for the observed inclination anomaly (I_{OBS}) is given by:

$$\tan I_{OBS} = \frac{Z}{X} = \frac{\sum_l (l+1) g_l^0 P_l^0(\cos\theta)}{\sum_l -g_l^0 \frac{d}{d\theta}P_l^0(\cos\theta)}. \tag{A.32}$$

The Equation (2.22) comes from the substitution of the explicit functions for $l = 1$ to 3 defined by the equations:

$P_1^0 = \cos\theta$;

$P_2^0 = \frac{1}{2}(3\cos^2\theta - 1)$;

$P_3^0 = \frac{1}{2}(5\cos^3\theta - 3\cos\theta)$

which are the Legendre polynomials for zonal terms.

B. Fisher statistics

A statistical method commonly used for paleomagnetic data analysis was developed by R. A. Fisher (1953), also known as the *Fisher distribution*, which is analogous to a normal distribution (or Gaussian distribution). Paleomagnetic directions are regarded as unit vectors, and the ends of these vectors are represented as points on the surface of a sphere of unit radius. Fisher suggested a probability density function $P_{dA}(\theta)$, which corresponds the probability of finding a direction within a area unit, dA, at an angular distance θ relative to the true mean direction. This function is given by:

$$P_{dA}(\theta) = \frac{\kappa}{4\pi \sinh(\kappa)} exp(\kappa \cos\theta), \tag{B.1}$$

where θ is the angle from the mean direction (= 0 for true mean direction). The parameter κ is referred to as *precision parameter* and describes the concentration of a population of directional data about the mean direction. If $\kappa = 0$ the directions are uniformly distributed over the sphere. For high κ values, the directions are more concentrated around the true mean. Examples of Fisher distribution functions are shown in Figure B.1a for κ = 5, 10, and 50.

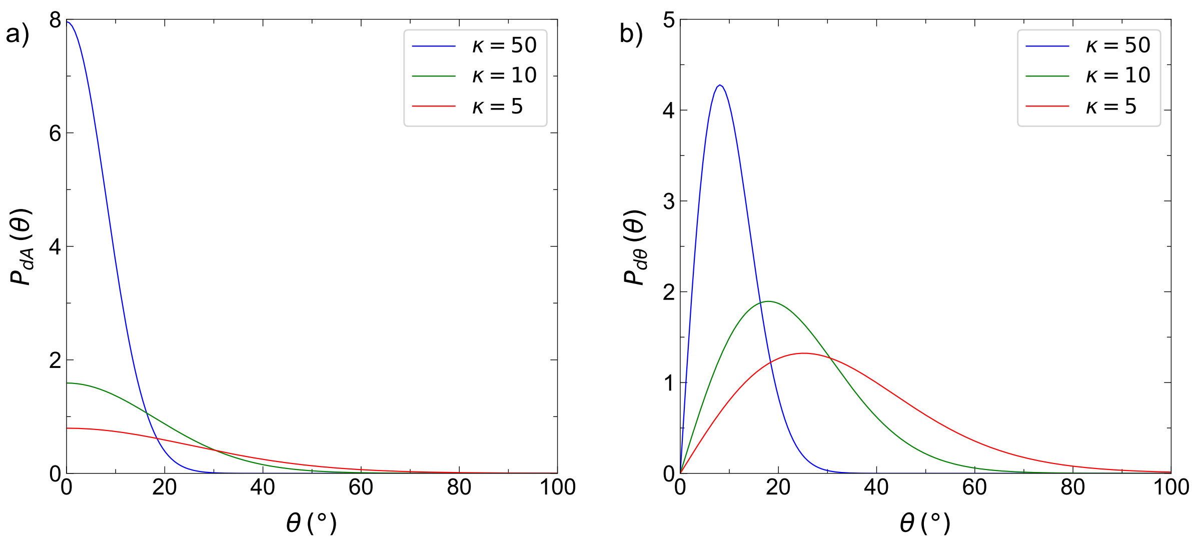

Figure B.1 – The Fisher distribution functions for κ = 5, 10, and 50. (a) $P_{dA}(\theta)$ is the probability of a direction falling within a unit area dA at an angle θ relative to the true mean. (b) $P_{d\theta}(\theta)$ is the probability of finding a direction within an angular width $d\theta$ between θ and $\theta + d\theta$ from the true mean. Modified from Butler (1998).

Assuming that the directions are azimuthally symmetric about the true mean direction, the Equation (B.1) can be rewrite as the probability $P_{d\theta}$ of a direction falls in a angular width $d\theta$ between angles θ and $\theta + d\theta$ from the true mean, expressed by:

$$P_{d\theta}(\theta) = \frac{\kappa}{2\sinh(\kappa)} exp(\kappa\cos\theta)\sin\theta d\theta. \tag{B.2}$$

This probability density function (for $\kappa = 5, 10$, and 50) is displayed in Figure B.1b. it is noticeable the influence of the sinusoidal term in the form of $P_{d\theta}$ functions.

Fisher statistic assumes that the mean direction of a set of directions is the best estimate of the true mean direction. To calculate the mean direction from a set of N unit vectors, first the individual directions (D_i, I_i) are converted to Cartesian coordinates (x_i, y_i, z_i):

$$\begin{aligned} &\text{North component:} && x_i = \cos I_i \cos D_i \\ &\text{East component:} && y_i = \cos I_i \sin D_i \\ &\text{Down component:} && z_i = \sin I_i. \end{aligned} \tag{B.3}$$

The mean directions these coordinates (X, Y and Z) are given by:

$$X = \frac{1}{R}\sum_{i=1}^{N} x_i, \qquad Y = \frac{1}{R}\sum_{i=1}^{N} y_i, \qquad Z = \frac{1}{R}\sum_{i=1}^{N} z_i, \tag{B.4}$$

where R is the length of the resultant vector expressed by:

$$R^2 = \left(\sum_{i=1}^{N} x_i\right)^2 + \left(\sum_{i=1}^{N} y_i\right)^2 + \left(\sum_{i=1}^{N} z_i\right)^2. \tag{B.5}$$

The value of R is always less than or equal to N. From Equations (B.4) and (B.5), the mean declination and inclination (D_m and I_m) can be determined by the following equations:

$$D_m = \tan^{-1}\left(\frac{Y}{X}\right) \tag{B.6}$$

and

$$I_m = \sin^{-1}(Z). \tag{B.7}$$

Using Fisher's statistic, the paleomagnetic pole can be calculated from a collection of N VGPs. Initially, the VGP locations (λ_{Vi}, ϕ_{Vi}) are converted into Cartesian polar coordinates, analogous to the equation system (B.3), as follows:

$$
\begin{aligned}
x_i' &= \cos\lambda_{Vi}\cos\phi_{Vi} \\
y_i' &= \cos\lambda_{Vi}\sin\phi_{Vi} \\
z_i' &= \sin\lambda_{Vi}.
\end{aligned} \tag{B.8}
$$

The sum vectors of these coordinates are given by:

$$
X_V = \frac{1}{R'}\sum_{i=1}^{N} x_i', \qquad Y_V = \frac{1}{R'}\sum_{i=1}^{N} y_i', \qquad Z_V = \frac{1}{R'}\sum_{i=1}^{N} z_i'. \tag{B.9}
$$

where R' is the length of the resultant vector of VGPs, and is defined as:

$$
R^{2'} = \left(\sum_{i=1}^{N} x_i{}'\right)^2 + \left(\sum_{i=1}^{N} y_i{}'\right)^2 + \left(\sum_{i=1}^{N} z_i{}'\right)^2. \tag{B.10}
$$

From equations (B.8) to (B.10), the mean pole latitude and longitude (λ_P and ϕ_P) are determined as:

$$
\lambda_P = \tan^{-1}\frac{Z_V}{\sqrt{X_V{}^2 + Y_V{}^2}} \tag{B.11}
$$

$$
\phi_P = \begin{cases}
\tan^{-1}\left(\dfrac{Y_V}{X_V}\right), & \text{if} \quad X_V \geq 0 \text{ and } Y_V \geq 0 \\
180^\circ - \tan^{-1}\left(\dfrac{Y_V}{X_V}\right), & \text{if} \quad X_V < 0 \text{ and } Y_V > 0 \\
180^\circ + \tan^{-1}\left(\dfrac{Y_V}{X_V}\right), & \text{if} \quad X_V > 0 \text{ and } Y_V < 0.
\end{cases} \tag{B.12}
$$

As mentioned previously, the measure of concentration from a set of N directional observations is given by the precision parameter, κ. In paleomagnetism, the directions are represented for a finite population. Thus, κ estimate can be determined approximately by:

$$
\kappa \approx k = \frac{N-1}{N-R}. \tag{B.13}
$$

From Equation (B.13), the k value increases as R approaches N for a tightly grouped distribution of direction about the mean direction.

Fisher showed that for $\kappa > 3$ the true mean direction of N unit vectors will have a probability level (1-P) of lying within a circular cone of semi-angle $\alpha_{(1-P)}$ about the resultant vector R, given by:

$$\alpha_{(1-P)} = cos^{-1}\left\{1 - \frac{N-R}{R}\left[\left(\frac{1}{P}\right)^{\frac{1}{N-1}} - 1\right]\right\}. \tag{B.14}$$

In paleomagnetic studies, P=0.05 is often used to determine the semi-angle of the 95% confidence cone about the mean direction, α_{95} (for the 95% confidence circle about the mean VGP, denotes as A_{95}). This parameter define the confidence limits of the mean direction at the 95% probability level. For k higher than 25, α_{95} is given approximately by (Tauxe, 2010):

$$\alpha_{95} \approx \frac{140°}{\sqrt{kN}}. \tag{B.15}$$

It is worth highlighting that the mean direction, Fisher concentration parameter, and 95% confidence cone are calculated assuming that the observed data are associated with random sampling from a set of directions following the Fisher distribution (Butler, 1998).

C. Vandamme method

To obtain stable polarity data, outlier VGPs marked by large deviations relative to the paleomagnetic pole (higher than 45°) are generally excluded in PSV studies. These anomalous VGP data can be associated with geomagnetic excursions, polarity transitions or measurement errors (Johnson & McFadden, 2015). Vandamme (1994) proposed a method that allows to obtain the optimum cutoff angle from the mean pole (or geographic north pole) to remove outlier data. This study was based on synthetic VGP data simulations, considering two contributions: (1) a Fisherian distribution characteristic of paleosecular variation, and (2) a uniform distribution reflecting transitional data. The cutoff angle (A) is defined as a function of VGP angular dispersion (S), given by:

$$A(^\circ) = 1.8S(^\circ) + 5(^\circ) \tag{C.1}$$

An iterative method is used according to the value obtained from A for a given dataset. If there are VGP data with values greater than that estimated by Equation (C.1), these data are removed and S is recalculated and the process is repeated until there are no data with higher cutoff values from Equation (C.1). https://doi.org/10.1016/j.pepi.2022.106926

D. Updated database for the 0-10 Ma interval

Table D.1 – Selected paleomagnetic studies for the 0-10 Ma interval.

Nr	Slat (°N)	Slon (°E)	Location	Age interval (Ma)	N	DC	Reference
1	78.61	10.92	Spitsbergen, Norway	0.5-9.15	14	5	Cromwell et al. (2013a)
2	70.92	351.20	Jan Mayen, Norway	0-0.461	23	5	Cromwell et al. (2013a)
3	64.87	344.90	Iceland	0.595-3.13	45	5	Døssing et al. (2016)
4	64.83	344.72	Iceland	0.78-1.82	17	4	Udagawa et al. (1999)
5	64.15	345.64	Iceland	0.33-7.00	111	5	Døssing et al. (2020)
6	64.03	340.08	Iceland	0-0.008	23	4	Pinton et al. (2018)
7	60.20	193.53	Alaska, USA	0.965	55	4	Coe et al. (2000)
8	53.42	190.09	Alaska, USA	0.075-2.06	75	4	Stone and Layer (2006)
9	51.51	237.65	Canada	0.0023-0.76	50	4	Mejia et al. (2002)
10	46.21	238.48	United States	0.0082-3.25	20	4	Mitchell et al. (1989)
11	45.90	24.25	East Carpathians	5.0	80	5	Vişan et al. (2016)
12	45.90	25.03	Romania	0.4-4.42	67	5	Panaiotu et al. (2012)
13	45.87	25.11	Romania	0.68-1.14	20	5	Panaiotu et al. (2013)
14	45.68	237.88	United States	0.059-3.25	65	5	Lhuillier et al. (2017)
15	43.13	246.54	United States	0.052-5.75	21	5	Tauxe et al. (2004)
16	41.57	43.52	Georgia	0.31-2.18	37	4	Goguitchaichvili et al. (2000)
17	41.20	43.55	Georgia	2.00-2.73	16	5	Calvo-Rathert et al. (2011)
18	40.27	113.59	China	0.525	16	5	Yamamoto et al. (2007)
19	38.60	331.20	Azores, Portugual	0.0019-0.0078	12	5	Di Chiara et al. (2014)
20	38.36	14.96	Italy	0.1-0.135	14	4	Laj et al. (1997)
21	37.75	334.54	Azores, Portugual	0.00034-0.88	31	5	Johnson et al. (1998)
22	36.94	357.23	Spain	2.61-8.2	10	4	Calvo-Rathert et al. (2009)
23	35.93	137.28	Japan	0.393-0.73	20	5	Tanaka et al. (2007)
24	35.92	137.46	Japan	0.021-0.084	35	5	Tanaka and Kobayashi (2003)
25	35.54	248.47	United States	0.00093-2.5	18	5	Tauxe et al. (2003)
26	32.69	35.42	Israel	0.10-4.7	45	5	Behar et al. (2019)
27	31.78	246.53	Mexico	0.00038-0.19	13	5	Rodríguez-Trejo et al. (2019)
28	28.66	341.96	Canary Islands	0.39-1.79	18	5	Tauxe et al. (2000)
29	28.18	343.94	Canary Islands	0.00030-0.015	38	4	Kissel et al. (2015)
30	27.71	341.93	Canary Islands	0.28	20	5	Monster et al. (2018)
31	27.46	342.26	Canary Islands	5.7	12	5	Leonhardt and Soffel (2006)
32	22.43	255.62	Mexico	8.9	45	5	Goguitchaichvili et al. (2002)
33	21.22	257.42	Mexico	2.9-10.0	23	5	Goguitchaichvili et al. (2011)
34	21.22	202.38	Hawaii, USA	0.033-0.677	14	5	Herrero-Bervera and Valet (2002)
35	21.16	252.40	Mexico	0.002-0.819	12	5	Petronille et al. (2005)
36	20.88	256.10	Mexico	0.115-1.12	15	5	Ceja et al. (2006)
37	20.73	258.09	Mexico	0.5-10.0	41	5	Ruiz-Martínez et al. (2010)
38	20.67	203.55	Hawaii, USA	3.1-3.19	82	5	Laj et al. (1999)
39	20.64	203.70	Hawaii, USA	0.00083-0.703	10	5	Herrero-Bervera and Valet (2007)
40	20.29	263.18	Mexico	1.53-7.33	13	5	Goguitchaichvili et al. (2007)
41	20.28	258.86	Mexico	0.56-2.78	11	5	Peña et al. (2011)
42	19.91	258.44	Mexico	0-3.53	32	5	Michalk et al. (2013)
43	19.84	258.15	Mexico	0.0011-0.0035	11	4	Mahgoub et al. (2018)

Table D.1. (continued)

Nr	Slat (°N)	Slon (°E)	Location	Age interval (Ma)	N	DC	Reference
44	19.73	260.56	Mexico	1.28-4.14	11	4	Mejia et al. (2005)
45	19.72	258.22	Mexico	0-2.1	22	4	Conte-Fasano et al. (2006)
46	19.38	260.45	Mexico	0-0.046	29	4	Mahgoub et al. (2019)
47	19.36	259.66	Mexico	0-0.029	11	5	Gonzalez et al. (1997)
48	19.33	260.81	Mexico	0.002	10	5	Alva-Valdivia (2005)
49	19.20	258.53	Mexico	0.0025-4.18	29	5	Peña et al. (2014)
50	19.17	258.57	Mexico	0.0024-0.0051	16	4	Mahgoub et al. (2017)
51	17.02	334.61	Cape Verde	0.477	27	5	M. C. Brown et al. (2009)
52	16.09	298.16	French West Indies	0.087-1.81	14	5	Ricci et al. (2018)
53	15.98	298.25	French West Indies	0.047-1.02	21	5	Carlut et al. (2000)
54	14.61	298.52	Martinique	0.0097-2.27	14	5	Tanty et al. (2015)
55	10.12	275.49	Costa Rica	0.005-2.11	30	5	Cromwell et al. (2013b)
56	4.90	284.63	Colombia	0-2.65	46	4	Sánchez-Duque et al. (2016)
57	2.13	35.77	Loiyangalani, Kenya	3.53-4.84	31	5	Opdyke et al. (2010)
58	-0.04	6.23	Sao Tome	0.5-5.5	38	4	Opdyke et al. (2015)
59	-0.47	281.77	Ecuador	0.0176-2.71	48	5	Opdyke et al. (2006)
60	-0.53	36.76	Mount Kenya, Kenya	0.3-5.36	60	5	Opdyke et al. (2010)
61	-1.07	269.14	Galapagos	1.5	52	4	Kent et al. (2010)
62	-4.33	327.74	Fernando de Noronha, Brazil	2.55-10.0	37	5	Leonhardt et al. (2003)
63	-7.46	111.94	Indonesia	0-6.7	44	5	Elmaleh et al. (2004)
64	-17.56	351.96	Saint Helena	8.8-10.3	34	5	Engbers et al. (2020)
65	-17.67	210.51	French Polynesia	0.905-4.21	116	5	Yamamoto et al. (2002)
66	-21.10	55.45	Reunion Island	0.073-0.131	15	4	Raïs et al. (1996)
67	-21.22	55.65	Reunion Island	0.0085-0.090	22	4	Chauvin et al. (1991)
68	-27.06	250.37	Easter Island	0.1-0.4	17	5	Miki et al. (1998)
69	-36.14	290.85	Argentina	0.007-1.72	30	5	Quidelleur et al. (2009)
70	-38.15	176.48	New Zealand	0.00012-0.021	13	5	Tanaka et al. (2009)
71	-38.90	288.24	Chile	0.00016-0.0051	18	4	Roperch et al. (2015)
72	-38.98	143.65	Australia	2.63	37	5	Opdyke and Musgrave (2004)
73	-39.28	175.58	New Zealand	0.015-0.292	24	5	Tanaka et al. (1997)
74	-39.29	174.05	New Zealand	0.00023	12	4	Lerner et al. (2019)
75	-46.45	51.47	Possession Island	0.64-3.00	36	4	Camps et al. (2001)
76	-47.08	288.79	Argentina	0.034-7.86	32	5	L. L. Brown et al. (2004)
77	-51.37	289.22	Argentina	0.165-8.67	37	4	Mejia et al. (2004)
78	-62.94	299.29	Deception Island, Antarctica	0.05	17	4	Oliva-Urcia et al. (2016)
79	-62.96	299.29	Deception Island, Antarctica	0.075	15	5	Baraldo et al. (2003)
80	-77.69	164.35	McMurdo, Antarctica	0.026-9.02	128	5	Lawrence et al. (2009)

Nr is the reference number. Slat and Slon are mean site latitude and mean site longitude (after plate motion correction) for each data set, respectively. Location is study region. N is the total number of sites for the 0-10 Ma interval. DC is the demagnetization code used to evaluate the data quality. References correspond to the published studies accepted in the database.

E. Paleomagnetism from southern Colombia

This appendix presents the supplementary material from the following article associated in this thesis:

Wellington P. de Oliveira, Gelvam A. Hartmann, Jairo F. Savian, Giovanny Nova, Mauricio Parra, Andrew J. Biggin, Ricardo I. F. Trindade. Paleosecular variation record from Pleistocene-Holocene lava flows in southern Colombia (2022). *Physics of the Earth and Planetary Interiors*, *332*, 106926.

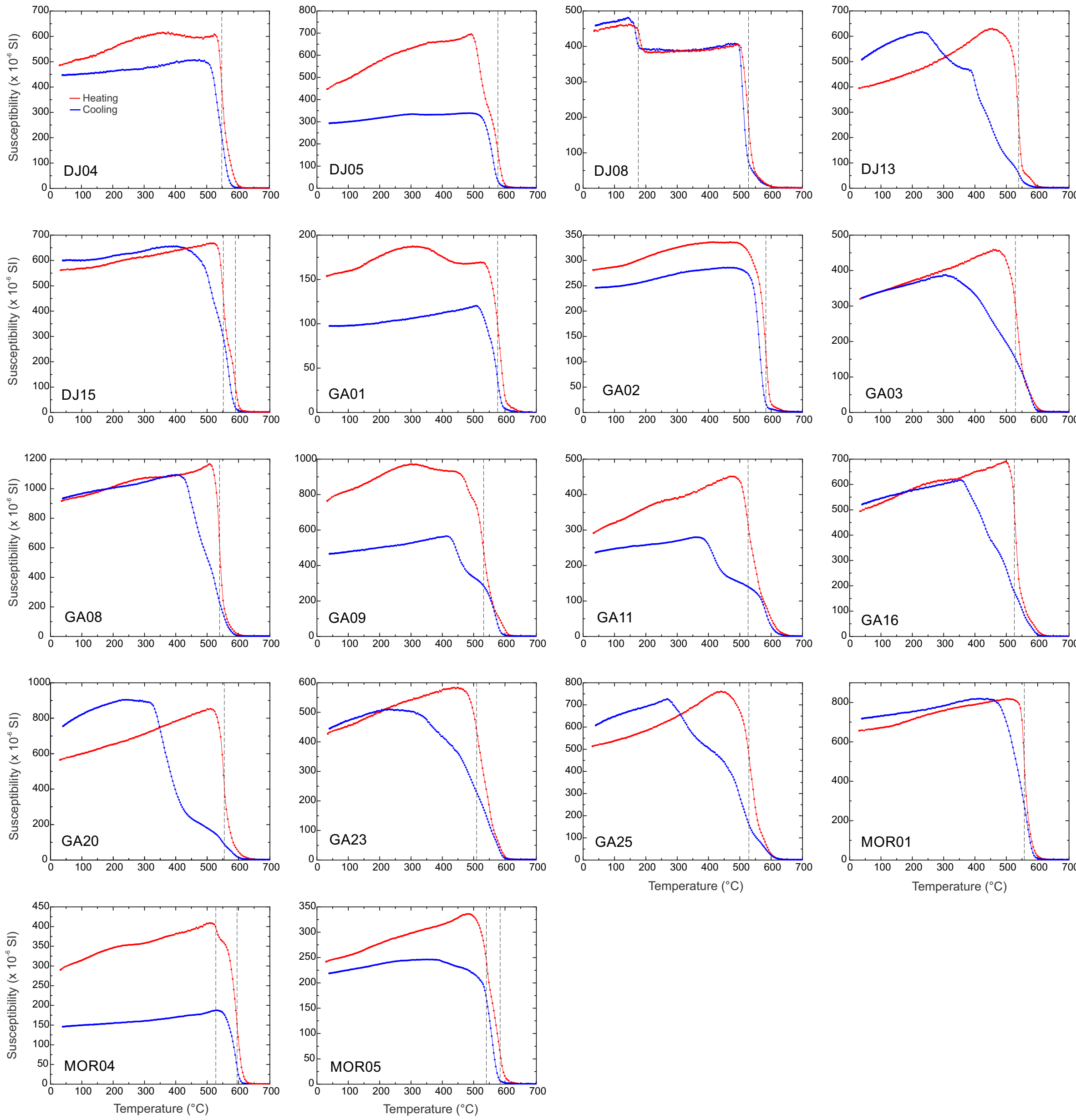

Figure E.1 – Examples of thermomagnetic curves during heating (red curve) and cooling (blue curve) cycles. Dashed lines indicate the Curie temperatures (T_c) summarized in Table E.1.

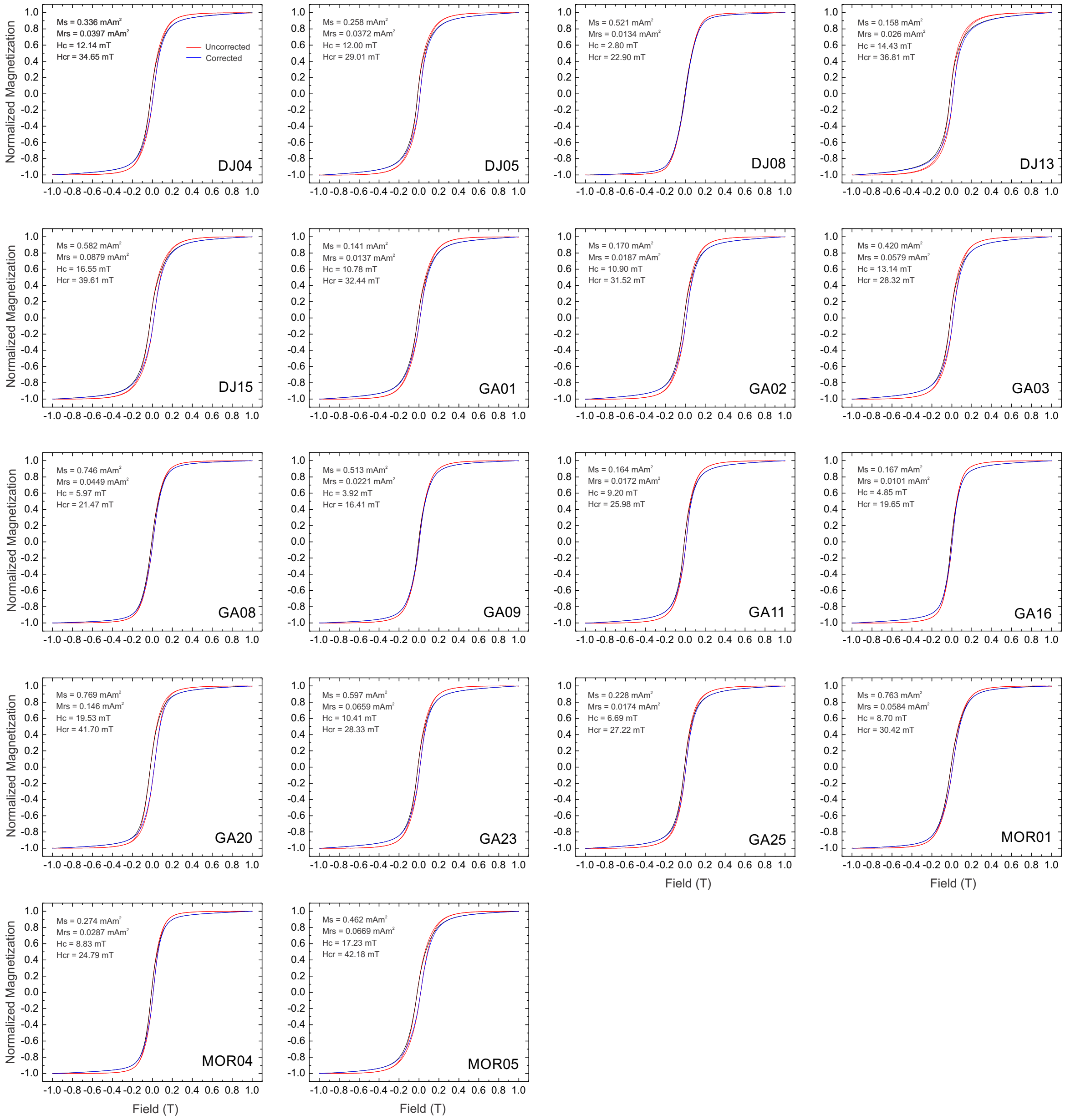

Figure E.2 – Examples of normalized hysteresis loops with their magnetic parameters (see Section 4.1.4.3 in the main article). Red (blue) curves show hysteresis loops with uncorrected (corrected) para- and diamagnetic contributions.

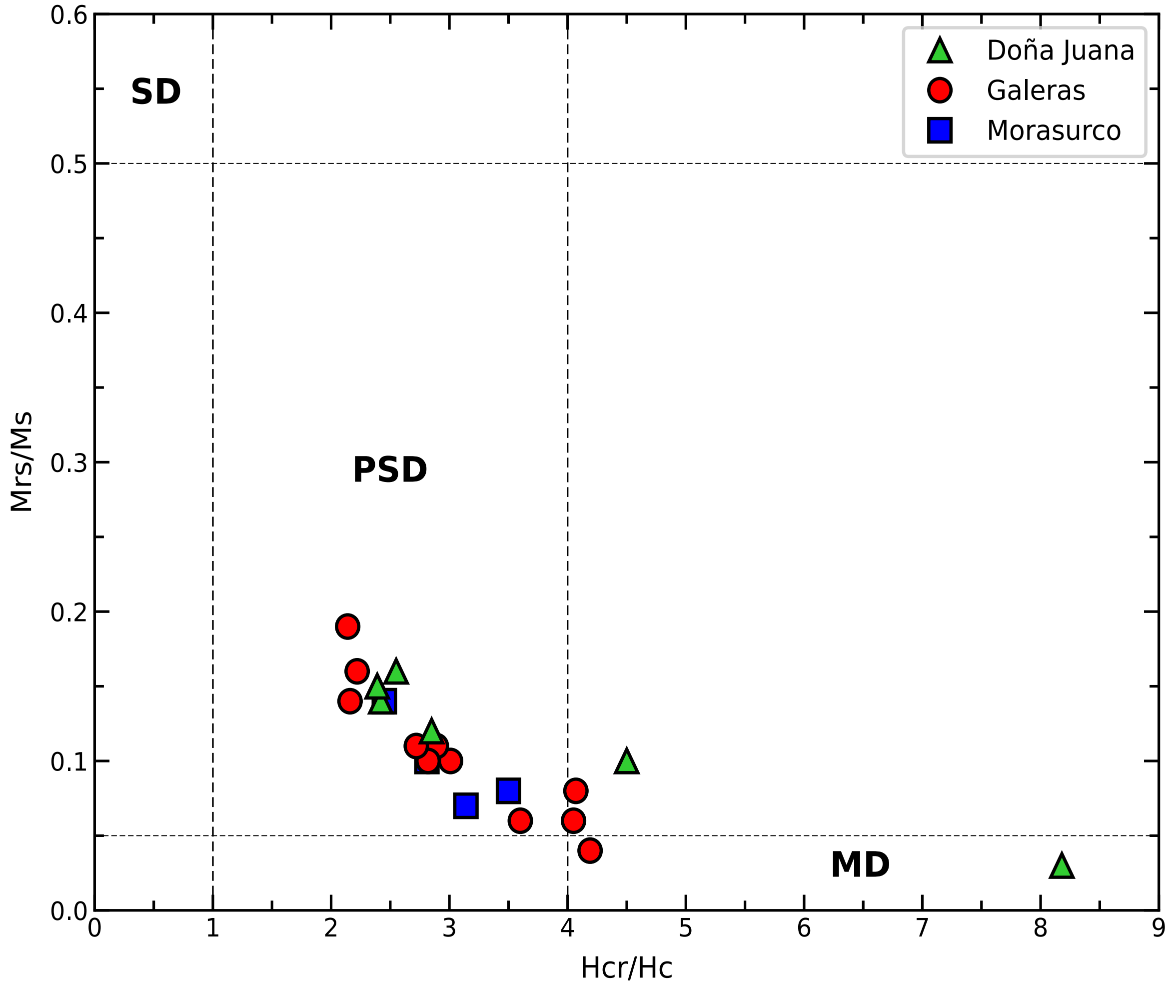

Figure E.3 – Day plot of representative samples (from 21 paleomagnetic sites). The estimates of hysteresis parameter ratios M_{rs}/M_s and H_{cr}/H_c are listed in Table E.1. SD = single domain; PSD = pseudo-single domain (or vortex state); MD = multidomain.

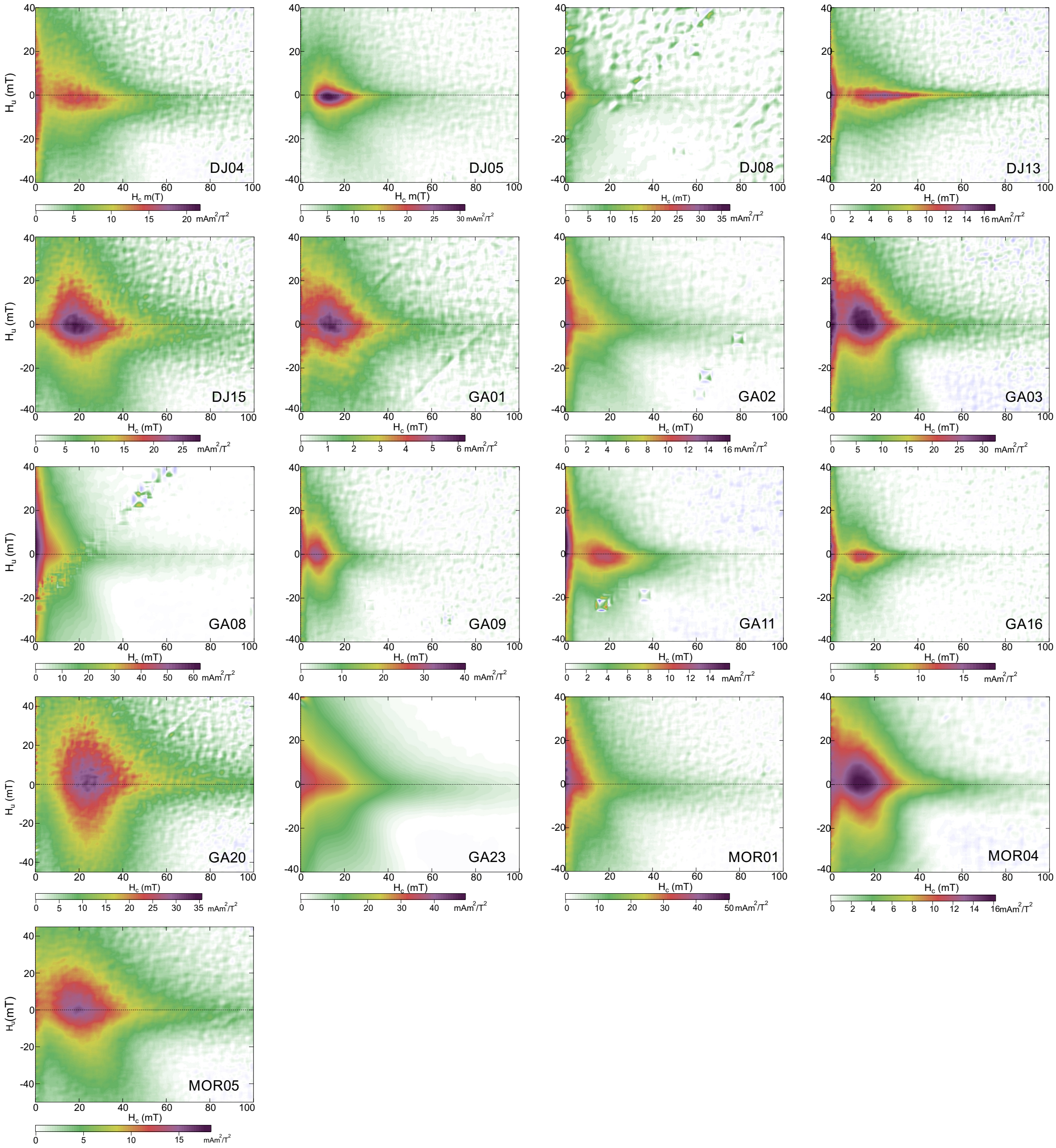

Figure E.4 – Examples of FORC diagrams. Details of magnetic domain structures are summarized in Table E.1

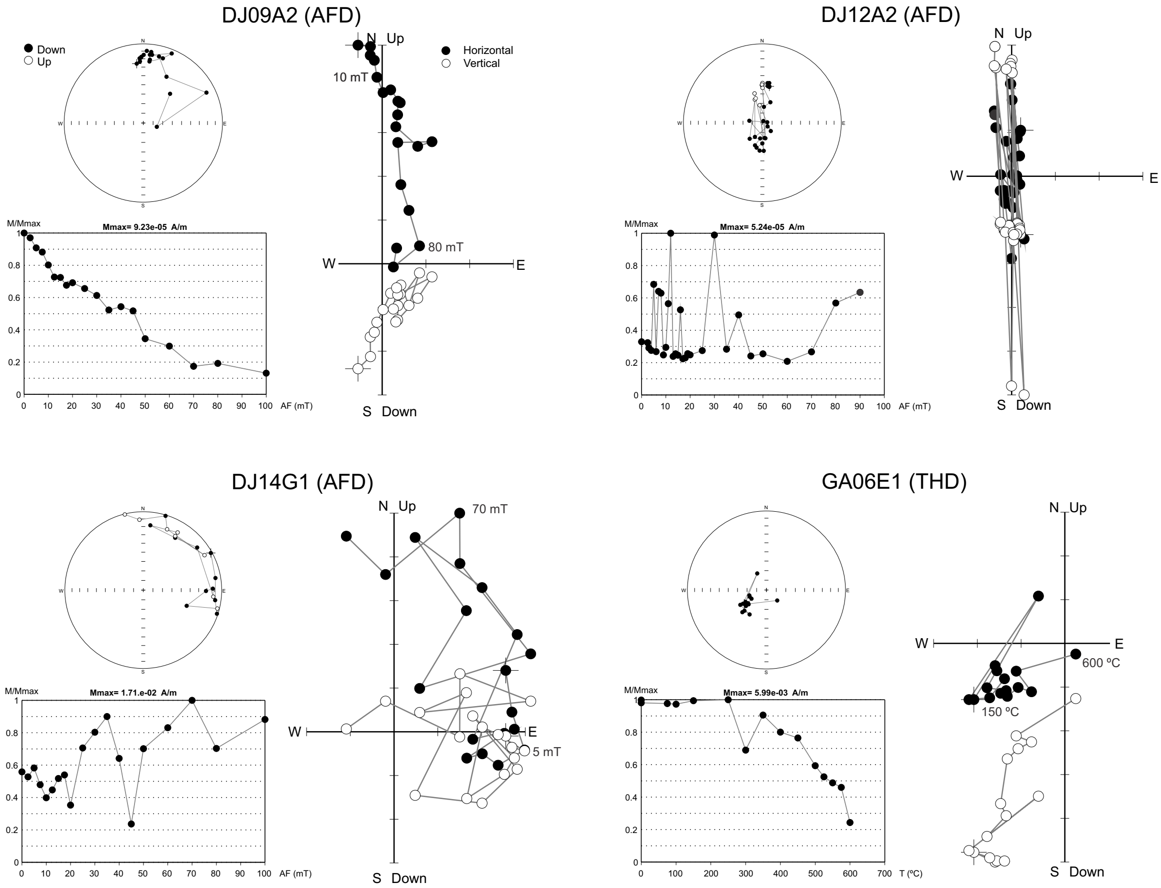

Figure E.5 – Examples of demagnetization diagrams for highly scattered data. Zijderveld diagrams, stereographic projections, and demagnetization curves of NRM components for sites (a) DJ09, (b) DJ12, (c) DJ14, and (d) GA06. NRM = natural remanent magnetization.

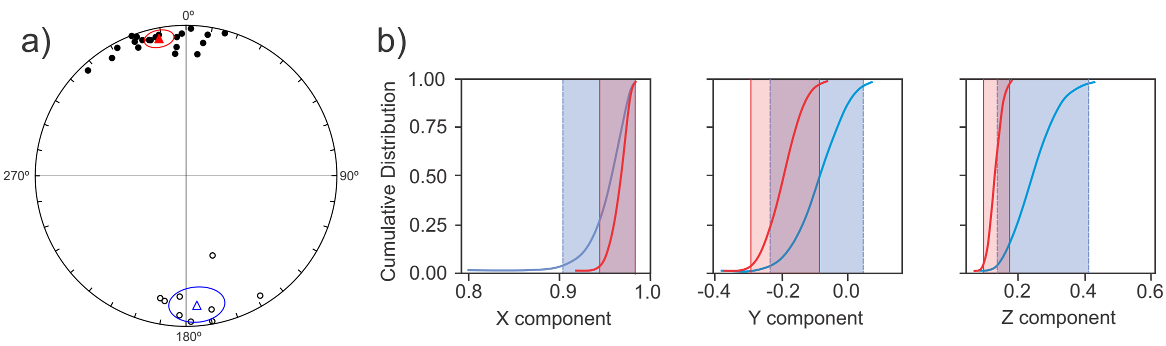

Figure E.6 – (a) Equal area projection of site-mean directions for normal (closed circles) and reverse (open circles) dataset. Red (blue) triangles represent the mean directions with their 95% confidence intervals for normal (reverse) polarity data. (b) Bootstrap reversal test defined by cumulative distributions of cartesian components for mean normal (red line) and mean reverse (blue line) directions. Red (blue) shaded areas are the 95% confidence regions for normal (reverse) modes.

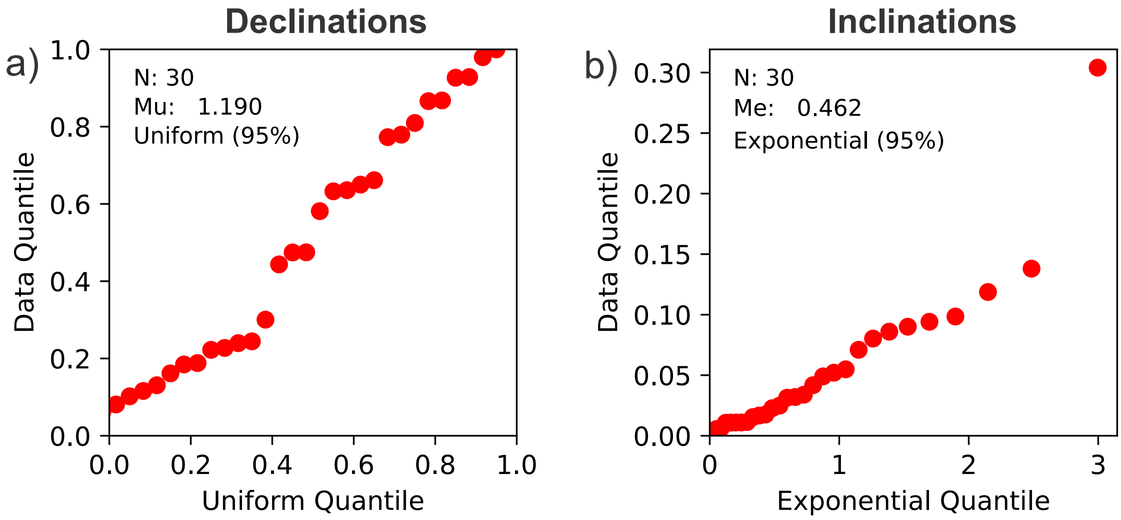

Figure E.7 – Quantile-quantile plots. (a) Declination data as a function of uniform distribution. (b) Inclination data as a function of exponential distribution.

Table E.1 – Magnetic mineralogy data derived from hysteresis loops, thermomagnetic susceptibility ($\chi(T)$) curves, and FORC diagrams.

Site	Hysteresis parameters						$\chi(T)$ curves	FORC states
	M_s (mAm^2)	M_{rs} (mAm^2)	H_c (mT)	H_{cr} (mT)	H_{cr}/H_c	M_{rs}/M_s	Transitions (°C)	
DJ04	0.336	0.0397	12.14	34.65	2.85	0.12	556.2, 433.1	VS + MD
DJ05	0.258	0.0372	12.00	29.01	2.42	0.14	593.9, 542.5	VS
DJ07	0.213	0.0215	11.26	50.69	4.50	0.10	575.3, 421.0	MD
DJ08	0.521	0.0134	2.80	22.90	8.18	0.03	529.4, 189.1	MD
DJ13	0.158	0.0260	14.43	36.81	2.55	0.16	542.2	VS + MD
DJ15	0.582	0.0879	16.55	39.61	2.39	0.15	601.0, 556.8	VS
GA01	0.141	0.0137	10.78	32.44	3.01	0.10	599.1, 419.3	VS
GA02	0.170	0.0187	10.90	31.52	2.89	0.11	593.9	VS
GA03	0.420	0.0579	13.14	28.32	2.16	0.14	544.6	VS + MD
GA08	0.746	0.0449	5.97	21.47	3.60	0.06	542.9	MD
GA09	0.513	0.0221	3.92	16.41	4.19	0.04	537.2, 333.6	VS + MD
GA11	0.164	0.0172	9.20	25.98	2.82	0.10	530.3	VS + MD
GA16	0.167	0.0101	4.85	19.65	4.05	0.06	539.7	VS + MD
GA20	0.769	0.146	19.53	41.70	2.14	0.19	556.8	VS
GA21	0.172	0.0271	17.93	39.83	2.22	0.16	559.3	VS
GA23	0.597	0.0659	10.41	28.33	2.72	0.11	516.5	VS
GA25	0.228	0.0174	6.69	27.22	4.07	0.08	553.0	MD
MOR01	0.763	0.0584	8.70	30.42	3.50	0.08	559.0	VS
MOR02	0.514	0.0383	8.91	27.95	3.14	0.07	580.6, 497.1	VS + MD
MOR04	0.274	0.0287	8.83	24.79	2.81	0.10	602.8, 534.8	VS + MD
MOR05	0.462	0.0669	17.23	42.18	2.45	0.14	595.0, 545.2	VS

Hysteresis parameters: saturation magnetization (M_s), saturation remanence magnetization (M_{rs}), coercive force (H_c), and coercivity of remanence (H_{cr}). MD = multidomain; VS = vortex state.